Complementary environmental analysis and functional characterization of a plastid diatom lower glycolytic-gluconeogenesis pathway

Short Title: Probing Diatom Chloroplast Lower Glycolysis

Richard G. Dorrell[1,2,3], Youjun Zhang[4,5,6], Yue Liang[7,8], Nolwenn Gueguen[9], Tomomi Nonoyama[1,10], Dany Croteau[11], Mathias Penot[1,2,3], Sandrine Adiba[1], Benjamin Bailleul[11], Valérie Gros[9], Juan José Pierella Karlusich[1,2,12], Nathanaël Zweig[1,2], Alisdair R. Fernie[4,5], Juliette Jouhet[9], Eric Maréchal[9] and Chris Bowler[1,2]

[1]Institut de Biologie de l'ENS (IBENS), Département de Biologie, École Normale Supérieure, CNRS, INSERM, Université PSL, 75005 Paris, France
[2]CNRS Research Federation for the study of Global Ocean Systems Ecology and Evolution, FR2022/Tara Oceans GOSEE, 3 rue Michel-Ange, 75016 Paris, France
[3]Laboratory of Computational and Quantitative Biology (LCQB), Institut de Biologie Paris-Seine (IBPS), CNRS, INSERM, Sorbonne Université, 75005 Paris, France
[4]Center of Plant Systems Biology and Biotechnology, 4000 Plovdiv, Bulgaria
[5]Max-Planck-Institute of Molecular Plant Physiology, Am Mühlenberg 1, 14476, Potsdam-Golm, Germany
[6]Key Laboratory of Seed Innovation, Institute of Genetics and Developmental Biology, Chinese Academy of Sciences, Beijing, China
[7]Center of Deep Sea Research, Institute of Oceanology, Center for Ocean Mega-Science, Chinese Academy of Sciences, Qingdao 266071, China
[8]Laboratory for Marine Mineral Resources, Pilot National Laboratory for Marine Science and Technology, Qingdao 266237, China
[9]Laboratoire de Physiologie Cellulaire et Végétale, CNRS, Univ. Grenoble Alpes, CEA, INRAE, IRIG, 17 rue des Martyrs, 38000 Grenoble, France
[10]Division of Biotechnology and Life Science, Institute of Engineering, Tokyo University of Agriculture and Technology, 2-24-16, Naka-cho, Koganei, Tokyo 184-8588, Japan
[11]Institut de Biologie Physico-Chimique (IBPC), Université PSL, 75005 Paris, France
[12]Present address: FAS Division of Science, Harvard University, Cambridge, MA, USA

The authors responsible for distribution of materials integral to the findings presented in this article in accordance with the policy described in the Instructions for Authors (https://academic.oup.com/plcell/pages/General-Instructions) are: Richard G. Dorrell (richard.dorrell@sorbonne-universite.fr) and Chris Bowler (cbowler@bio.ens.psl.eu)

Abstract

Organic carbon fixed in chloroplasts through the Calvin Cycle can be diverted towards different metabolic fates, including cytoplasmic and mitochondrial respiration; gluconeogenesis; and synthesis of diverse plastid metabolites via the pyruvate hub. In plants, pyruvate is principally produced via cytoplasmic glycolysis, although a plastid-targeted lower glycolytic pathway is known in non-photosynthetic tissue. Here, we characterize a lower plastid glycolytic-gluconeogenesis pathway in diatoms, ecologically important marine algae distantly related to plants. We show that two reversible enzymes required to complete diatom plastid glycolysis-gluconeogenesis, Enolase and PGAM (*bis*-phospho-glycerate mutase), originated through duplications of mitochondria-targeted respiratory isoforms. Through CRISPR-Cas9 mutagenesis, integrative 'omic analyses, and measured kinetics of expressed enzymes in the diatom *Phaeodactylum tricornutum*, we present evidence that this pathway diverts plastid glyceraldehyde-3-phosphate into the pyruvate hub, and may also function in the gluconeogenic direction. Considering experimental data, we show that this pathway has different roles dependent in particular on day length and environmental temperature, and show that it is expressed at elevated levels in high latitude oceans where diatoms are abundant. Our data provide evolutionary, meta-genomic and functional insights into a poorly understood yet evolutionarily recurrent plastid metabolic pathway.

Keywords: chloroplast; *Tara* Oceans; meta-genomics; post-endosymbiotic evolution; plastid-mitochondria crosstalk; RNAseq; GC and LC-MS; photophysiology

Introduction

Each year, over 250 gigatonnes of atmospheric carbon dioxide is assimilated through photosynthesis, with effectively equal contributions from terrestrial plants and aquatic algae (Friedlingstein, Jones et al. 2022). This activity is essential for maintaining planetary climate homeostasis, supporting the entire Earth ecosystem. Carbon assimilated through photosynthesis via the Calvin cycle is diverted into multiple metabolic fates (Raines 2003). In plants, these include gluconeogenesis of glucose-6-phosphate directly in plastids (or chloroplasts), which can then be used in leaf tissue for starch storage (Scialdone, Mugford et al. 2013). Additional metabolites including fatty acids and lipids, amino acids, chlorophyll and carotenoid pigments are synthesised directly in the plastid (Tanaka and Tanaka 2007, Bromke 2013, Maréchal and Lupette 2020, Bai, Cao et al. 2022) (**Fig. 1A**). Many of these plastid metabolic reactions utilize pyruvate, or its adjacent metabolic precursor phospho-*enol*-pyruvate (or PEP), and are referred to collectively as the pyruvate hub (Shtaida, Khozin-Goldberg et al. 2015). In addition, plant photosynthate is exported from the plastids to the cytosol for subsequent glycolysis and respiration in the mitochondria (Moog, Rensing et al. 2015), or for transport to non-photosynthetic tissue (Carrera, George et al. 2021) (**Fig. 1A**).

Plants are classically thought to generate PEP and pyruvate through glycolysis in the cytoplasm, then reimport these metabolites into the plastids (**Fig. 1A**) (Moog, Nozawa et al. 2020). Alongside this, certain plants may synthesize pyruvate hub substrates directly from the Calvin cycle inside the plastid. This conversion is performed by two enzymes, plastid-targeted phospho-glycerate mutase and enolase (henceforth referred to as cpPGAM and epEnolase), which allow the conversion of 1,3-bis-phosphoglycerate from the Calvin cycle to PEP (**Fig. 1A**) (Raines 2003, Andriotis, Kruger et al. 2010). Both Enolase and PGAM have been shown experimentally to be fully reversible enzymes, with bidirectional functions that we henceforth refer to as glycolysis-gluconeogenesis, contrasting with glycolysis and gluconeogenesis to signify enzymatic activities in one direction only (Sutherland, Posternak et al. 1949). Documented plant cpEnolase and cpPGAM enzymes are associated with non-photosynthetic tissues such as seeds and roots (Prabhakar, Löttgert et al. 2009, Fukayama, Masumoto et al. 2015, Troncoso-Ponce, Rivoal et al. 2018). *Arabidopsis thaliana* cpEnolase and cpPGAM knockout lines have limited phenotypes under replete growth conditions (Prabhakar, Löttgert et al. 2009,

Andriotis, Kruger et al. 2010, Anoman, Flores-Tornero et al. 2016), raising questions of their overall function.

Diatoms are a eukaryotic algal group that is distantly related to plants, with over one billion years of evolutionary separation between the nuclear and mitochondrial genomes of each species (Nonoyama, Kazamia et al. 2019, Strassert, Irisarri et al. 2021). In contrast to the primary plastids of plants, surrounded by two membranes and of bacterial origin, diatoms possess complex plastids surrounded by four membranes and derived from a eukaryotic red alga, which is likewise ancient (Nonoyama, Kazamia et al. 2019, Liu, Storti et al. 2022). Diatoms are extraordinarily successful in the modern ocean, comprising nearly half of total algal abundance e.g., in environmental sequence data from the *Tara* Oceans expedition (Malviya, Scalco et al. 2016, Behrenfeld, Halsey et al. 2021). Diatoms are particularly abundant in high-latitude and temperate oceans (i.e., the North Atlantic, North Pacific and Southern Oceans) that are characterised by stresses including low temperatures and elongated photoperiods (long days in the summer, and long nights in the winter) (Gilbertson, Langan et al. 2022, Joli, Concia et al. 2024). Previous studies, particularly of the transformable coastal and mesophilic species *Phaeodactylum tricornutum*, have identified multiple strategies that allow diatoms to tolerate photo-stress, including complex inter-organelle metabolite trafficking (Bailleul, Berne et al. 2015, Broddrick, Du et al. 2019, Smith, Dupont et al. 2019) and extensive photoprotective capabilities (reviewed in (Lepetit, Campbell et al. 2022). These data are further supported by extensive environmental (meta-genomic) sequence data such as those of the *Tara* Oceans mission. While the data from these studies relate fundamentally to different species to *Phaeodactylum* (i.e., open-ocean diatoms, including from polar habitats) they may allow us to understand how individual diatom chloroplast proteins function at ecosystem scales, as well as under laboratory conditions (Kazamia, Sutak et al. 2018, Liu, Storti et al. 2022).

Diatom carbon metabolism is highly different to that of plants (Kroth, Chiovitti et al. 2008). Differences include the storage of sugars in cytoplasmic vacuoles (as chrysolaminarin) as opposed to plastidial starch, and the synthesis of most lipid groups (e.g., galactolipids and part of triacylglycerol pathway) directly in the plastid (Zhu, Shi et al. 2016, Huang, Pan et al. 2024). Diatom plastids furthermore possess

136 no known plastid hexose phosphate transporters, which in plants are implicated in
137 plastidial sugar import in storage tissue. Diatoms are instead inferred to exchange
138 sugars with the cytoplasm via triose phosphates only (Moog, Nozawa et al. 2020, Liu,
139 Storti et al. 2022) (**Fig. 1A**). The lower half of respiratory glycolysis-gluconeogenesis
140 in diatoms occurs in the mitochondria, as opposed to the cytoplasm (Kroth, Chiovitti
141 et al. 2008, Río Bártulos, Rogers et al. 2018); and a complete plastid lower half
142 glycolysis-gluconeogenesis, including cpEnolase and cpPGAM proteins, has been
143 inferred from sequenced diatom genomes (Kroth, Chiovitti et al. 2008, Smith,
144 Abbriano et al. 2012, Hippmann, Schuback et al. 2022) (**Fig. 1A**). As diatoms are
145 unicellular and colonial species, plastid glycolysis presumably occurs organelles that
146 perform photosynthesis, contrasting with its predominant association with non-
147 photosynthetic tissues in plants (**Fig. 1A**).
148
149 Here, we profile sequence datasets from cultivated and environmental diatoms,
150 perform characterization of *P. tricornutum* CRISPR-CAS9 knockout mutants and
151 measure kinetic activities of expressed enzymes, to infer possible functions of diatom
152 cpEnolase and cpPGAM enzymes. We demonstrate that the genes encoding these
153 enzymes arose from diatom mitochondria-targeted and respiratory isoforms in a
154 common ancestor of all species, contrasting to other algae and plants in which it has
155 a sporadic distribution. We further show that the genes encoding these proteins are
156 most highly expressed at high latitudes in environmental sequence data from *Tara*
157 Oceans, and indeed their expression is induced in *Phaeodactylum* in response to
158 continuous light and low temperature. From *Phaeodactylum* knockout phenotypes,
159 we present evidence that this pathway may have different functions in cells grown
160 under continuous illumination as opposed to light-dark cycling, and at low compared
161 to moderate temperature. We use mutant phenotypes and measured kinetic activities
162 to propose metabolic functions of diatom cpEnolase and cpPGAM under different
163 illumination and temperature regimes. Overall, our data position lower half glycolysis-
164 gluconeogenesis as a modulator of diatom plastid metabolic poise, providing insights
165 into its physiological roles for photosynthetic organisms beyond plants.
166
167 **Results**
168

169 *Distribution and phylogeny of cpEnolase and cpPGAM across photosynthetic*
170 *eukaryotes*
171
172 To evaluate the occurrence of plastid-targeted glycolysis across the algal tree of life,
173 we searched for plastid-targeted homologues of *Phaeodactylum tricornutum* and
174 *Arabidopsis thaliana* enolase and PGAM enzymes in 1,673 plant and algal species,
175 considering genomes from JGI PhycoCosm, and transcriptomes from the MMETSP
176 (Marine Microbial Eukaryotic Transcriptome Sequencing Project) and OneKp (One
177 Thousand Plant Transcriptomes) initiatives (Keeling, Burki et al. 2014, Initiative 2019,
178 Grigoriev, Hayes et al. 2021). Plastid-targeting sequences were inferred using both
179 PFAM domain presence and the combined *in silico* predictions of HECTAR,
180 ASAFind, WolfPSort, TargetP and PredAlgo (Emanuelsson, Brunak et al. 2007,
181 Horton, Park et al. 2007, Gschloessl, Guermeur et al. 2008, Tardif, Atteia et al. 2012)
182 (**Table S1,** sheet 1). Plastid lower glycolysis-gluconeogenesis was frequently inferred
183 in diatoms, with 60/101 (59%) libraries with identified enolase and PGAM sequences
184 possessing plastid-targeted versions of each. A lower occurrence (22/69 libraries,
185 32%) was found amongst close relatives in the stramenopiles (e.g., pelagophytes,
186 dictyochophytes) and other algae with secondary red plastids (cryptomonads,
187 haptophytes; 25/94 libraries, 27%) (**Fig. S1A**). Within primary plastid-harbouring
188 lineages, only angiosperms were inferred to frequently possess plastid-targeted
189 copies of both enzymes (47/537 libraries, 9%). Notably, only 4/127 (3%) occurrences
190 were inferred in primary green algae and none in primary red algae, suggesting that
191 diatom plastid glycolysis does not derive from the secondary red chloroplast ancestor
192 (**Fig. S1A**).
193
194 Considering collection sites, diatom species with either plastid glycolysis enzyme
195 typically derive from higher latitudes (mean absolute latitude 45.6°, standard
196 deviation 13.5°, n = 81) than ones that possess neither (mean absolute latitude
197 38.9°, standard deviation 24.3°, n = 10; one-way ANOVA P = 0.19; **Fig. S1B**). This
198 difference was deemed to be significant for certain diatom groups (e.g., araphid
199 pennate diatoms, **Supplemental Dataset S1**, sheet 1; one-way ANOVA P = 0.012),
200 but was not observed in other algal groups.
201

202 Next, we explored the specific origins of *P. tricornutum* plastid Enolase and PGAM
203 sequences from diatoms by building phylogenies of the closest orthologs obtained
204 from other diatoms, the broader taxonomic group to which they belong, the
205 stramenopiles, and two other algal groups, the cryptomonads and haptophytes.
206 These lineages all possess plastids of secondary red endosymbiotic origin,
207 surrounded by four membranes, which are likely to be closely related to one another
208 (Strassert, Irisarri et al. 2021), but also contain non-photosynthetic members (e.g.,
209 oomycetes in stramenopiles) which only possess respiratory (i.e., mitochondria-
210 targeted) lower half glycolytic enzymes (Río Bártulos, Rogers et al. 2018). Single-
211 gene trees were made for the conserved domains of all organelle-targeted Enolase
212 and PGAM sequences from 289 cryptomonad, haptophyte and stramenopile
213 genomes and transcriptomes, plus all orthologs from 85 further genomes selected
214 from across the tree of life, based on a previously defined pipeline (**Supplemental**
215 **Dataset S1**, sheet 2-9). **Figs. 1B** and **1C** show consensus MrBayes trees realised
216 with GTR, Jones and WAG substitution matrices for species with both identifiable
217 plastid- and mitochondria- targeted orthologs of each protein.
218
219 The obtained topologies revealed multiple evolutionary origins for plastid Enolase
220 and PGAM sequences from mitochondria-targeted (respiratory) enzymes, with
221 diatom plastid isoforms typically having recent and/or diatom-specific evolutionary
222 origins. Diatom cpEnolase sequences resolve in a well-supported clade with plastid-
223 targeted enzymes from bolidophytes, dictyochophytes and pelagophytes, which are
224 sisters to diatoms in the stramenopiles (Río Bártulos, Rogers et al. 2018, Nonoyama,
225 Kazamia et al. 2019), followed by mitochondria-targeted proteins from these groups
226 (MrBayes PP = 1.0 under all studied matrices, **Fig. 1B**), other photosynthetic
227 (chrysophytes) and non-photosynthetic stramenopiles (oomycetes; MrBayes PP = >
228 0.95 under GTR and Jones matrices, **Fig. 1B**). This indicates a duplication and
229 recruitment of the host-derived mitochondria-targeted protein to the plastid within a
230 common ancestor of the diatoms, pelagophytes and dictyochophytes. A broader
231 evaluation of cpEnolase distribution suggests further duplications and plastid
232 retargeting of mitochondria-targeted enolase proteins in both the chrysophytes and
233 cryptomonads (**Fig. S2**).
234

235 The PGAM phylogeny revealed at least two closely-related families of plastid-
236 targeted diatom enzymes, both likely derived from host mitochondrial isoforms. The
237 cpPGAM1A clade (typified by the *P. tricornutum* protein Phatr3_J17086) was closely
238 related to mitochondrial-targeted proteins found across the stramenopiles (MrBayes
239 PP = 1.0 under all studied matrices, **Fig. 1C**), followed by plastid-targeted proteins
240 from chrysophytes and mitochondria-targeted oomycete proteins. Similarly, the
241 cpPGAM1B (Phatr3_J51404) clade included mitochondrial-targeted proteins from
242 pelagophytes and dictyochophytes (MrBayes > = 0.85 under all studied matrices,
243 **Fig. 1C**), and plastid- and mitochondria-targeted enzymes from the chrysophytes
244 (**Fig. S3**). Further duplications and plastid recruitments of mitochondria-targeted
245 PGAM proteins were again visible in the haptophytes and cryptomonads (**Fig. S3**).
246
247 A final plastid-targeted protein annotated as PGAM in the version 3 *P. tricornutum*
248 genome (Rastogi, Maheswari et al. 2018), hereafter termed PGAM2, was identified
249 exclusively in diatoms, pelagophytes, and haptophytes (**Fig. S4**), with limited
250 homology to PGAM1 (BLASTp e-value > 1.0 in pairwise protein-protein searches).
251 Only PGAM1 contain an annotated phospho-glyceromutase active site (IPR005952)
252 per InterProScan, while both PGAM1 and PGAM2 contain the same PFAM (histidine
253 phosphatase, PF03000) per PFAMscan (Jones, Binns et al. 2014, Mistry,
254 Chuguransky et al. 2020). PGAM2 enzymes were predominantly mitochondria-
255 targeted, with plastid- or dual-targeted isoforms amongst diatoms only identified in *P.*
256 *tricornutum* (Phatr3_J37201, and a more divergent copy Phatr3_J47096) and three
257 species in which it is inferred to have evolved independently (**Fig. S4**).
258
259 *Plastidial localisation and expression dynamics of* Phaeodactylum *lower glycolysis*
260 *enzymes*
261
262 To confirm plastid localization of *P. tricornutum* cpEnolase and cpPGAM, eGFP-
263 tagged copies of three proteins (Phatr3_J41515, cpEnolase; Phatr3_J17086,
264 cpPGAM1A; Phatr3_J37201, cpPGAM2) were expressed in *P. tricornutum* Pt1.86
265 cells via biolistic transformation. The observed GFP fluorescence patterns were
266 coincident with chlorophyll autofluorescence, consistent with *in silico* targeting
267 predictions in each case and confirming plastid localization (**Figs. 1D, S5**). We note
268 that both cpEnolase (named per its previous annotation Phatr2_J56418) and

cpPGAM1B (named Phatr2_J42857) have been independently localised with GFP to the *P. tricornutum* plastid in a separate study (Río Bártulos, Rogers et al. 2018).

Next, we considered previously published experimental proteomic data of plastid-enriched and *Phaeodactylum* total cellular fractions, following (Huang, Pan et al. 2024). Both cpEnolase and cpPGAM1A were detected in multiple plastid-enriched and total cell proteome samples, respectively forming 0.040% and 0.0033% of the mean plastid-enriched total proteome (**Fig. S6A**). These abundances were analogous to the total abundances and plastid enrichment ratios found for other Calvin cycle and plastidial carbon metabolism enzymes, e.g. pyruvate kinase (Phatr3_J22404), ribose-5-phosphate isomerase (Phatr3_J13382), and ribulose-5-phosphate epimerase (Phatr3_J53395). Both mtEnolase (Phatr3_draftJ1572) and mtPGAM (Phatr3_J33839) were also detected in plastid-enriched fractions, which may relate to close associations observed between the *Phaeodactylum* plastid and mitochondria, (Bailleul, Berne et al. 2015, Uwizeye, Decelle et al. 2020). No other organelle-associated enolase or PGAM enzymes were detected, including cpPGAM1B and cpPGAM2, suggesting that they are present at low abundances in the *Phaeodactylum* cell (**Fig. S6A; Supplemental Dataset S2,** sheet 1).

We further considered the transcriptional dynamics of *Phaeodactylum* lower plastid glycolysis proteins, using a pooled and ranked dataset of normalised microarray and RNAseq data to identify genes that are co-expressed with one another and which may perform linked cellular functions (Ashworth, Turkarslan et al. 2016, Ait-Mohamed, Novák Vanclová et al. 2020, Liu, Storti et al. 2022) (**Fig. S6B**; **Supplemental Dataset S2**, sheet 2-3). From these data, cpEnolase and cpPGAM1A showed strong, positive coregulation to one another ($r = 0.868$, $P < 10^{-05}$), with cpPGAM1A the second most strongly coregulated gene to cpEnolase across the entire *Phaeodactylum* genome. Other cpPGAMs showed much weaker coregulation to both cpEnolase and cpPGAM1A, including cpPGAM1B (cpEnolase $r = 0.432$; cPGAM1A $r = 0.473$) and cpPGAM2 (cpEnolase $r = 0.490$; cPGAM1A $r = 0.478$; **Fig. S6B**). The coexpression of cpEnolase and cpPGAM1A and accumulation of both encoded proteins in the plastid suggest that they possess linked metabolic functions.

302 We then explored under what conditions cpEnolase and cpPGAM genes are likely to
303 be highly expressed, considering RNAseq (**Fig. S7A-C**) and microarray (**Fig. S7D**)
304 data (**Supplemental Dataset S2**, sheet 4). These data suggested that nutrient
305 limitation does not directly induce the expression of the chloroplast-targeted
306 glycolysis proteins, with the ratio of expression of genes encoding chloroplast- versus
307 mitochondria-targeted copies of each enzyme either remaining unchanged in
308 published nitrate limitation (nitrate reductase knockout) and iron limitation data (**Fig.**
309 **S7A, B;** one-way ANOVA $P < 0.05$ (Smith, Gillard et al. 2016, McCarthy, Smith et al.
310 2017)). In an analogous study of phosphate limitation, we even observed a lower
311 ratio of plastid to mitochondrial glycolysis gene expression in phosphate-starved
312 versus -replete and -replenished cell lines (ptEnolase/ mtEnolase ratio one way
313 ANOVA $P = 0.009$, ptPGAM/ mtPGAM ratio one-way ANOVA $P = 0.049$ (**Fig. S7C**;
314 (Cruz de Carvalho, Sun et al. 2016)).
315
316 In contrast, we observed clear impacts of light quality and daylength on plastidial
317 glycolysis gene expression. In an RNAseq study of the effects of the Circadian cycle
318 on Fe-limited and -replete *Phaeodactylum* cells (Smith, Gillard et al. 2016), a much
319 higher ratio of plastid to mitochondrial Enolase gene expression was identified in
320 samples harvested twelve hours post-illumination than other time points (**Fig. S7B**;
321 one-way ANOVA $P = 4 \times 10^{-05}$). From a similar meta-analysis of microarray data
322 (Ashworth, Turkarslan et al. 2016), cpEnolase showed greatest relative fold-change
323 in RNA samples (one-way ANOVA $P < 10^{-05}$) collected between 8 and 16h after the
324 light onset, and were strongly suppressed following 30 minutes of white, red, green
325 and blue light treatment (**Fig. S7D**). cpPGAM showed the same trends albeit with
326 lower expression in normal light 10.5 h after the light induction period than 16h (**Fig.**
327 **S7D; Supplemental Dataset S2,** sheet 4). Both cpEnolase and cPGAM1A showed
328 strong suppression in microarray data obtained following four hours compared to
329 thirty minutes dark incubation (one-way ANOVA, P 0.05); and two days dark
330 incubation compared to two-days high light treatment (one-way ANOVA $P < 10^{-05}$;
331 **Fig. S7D**) suggesting that these effects relate to light perception.
332
333 Finally, we performed quantitative RT-PCR of cpEnolase and cpPGAM1A genes
334 from wild-type *Phaeodactylum* cells under different conditions (**Fig. 2B**). qRT-PCRs
335 were performed on RNA collected from late exponential phase cells at the subjective

336 day mid-points at 19°C and 12 h: 12 h light: dark cycling (19C LD); the same time but
337 for cells grown under 19°C and 24 h continuous light (19C CL); and the same time
338 but for cells grown under 8°C and 24 h continuous light (8C CL), considering *Tara*
339 Oceans sampling data (see below; **Supplemental Dataset S2**, sheet 4). qRT-PCRs
340 were performed using two RT-PCR amplicons for each gene and two normalisation
341 references (RPS, and TBP) previously shown to have invariant expression under
342 Circadian cycles in *Phaeodactylum* (Sachse, Sturm et al. 2013).
343
344 Both cpEnolase and cpPGAM1A showed transcriptional responses to light and
345 temperature, with different responses dependent on normalisation reference. The
346 expression of cpEnolase was inferred to be increased in 19C CL relative to 19C LD
347 when normalised to RPS (fold-change: 2.31, one-way ANOVA P = 0.028) although
348 no difference was measured by normalisation to TBP. In contrast, the expression of
349 cpEnolase was found to be significantly higher under 8C CL than 19C CL conditions
350 considering both RPS (fold-change: 2.74, P = 0.015) and TBP (fold-change: 4.17, P
351 = 0.001; **Fig. 2B**). cPGAM1A expression was inferred to be increased in 19C CL
352 relative to 19C LD conditions normalised to both RPS (fold-change: 6.33, P = 0.003)
353 and TBP (fold-change: 2.50, P = 0.002); but was only inferred to increase in 8C CL
354 relative to 19 CL conditions normalised to TBP (fold-change: 1.96, P = 0.005; **Fig.**
355 **2B**). In total these data suggest additive effects of both continuous light and low
356 temperature on *Phaeodactylum* cpPGAM1A and cpEnolase expression.
357
358 *Environmental roles of diatom cpEnolase and cpPGAM inferred from meta-genomics*
359
360 Next, we considered general patterns of transcriptional co-regulation of diatom
361 cpEnolase and cpPGAM sequences in environmental sequence data from *Tara*
362 Oceans. First, we used a previously benchmarked pipeline, based on combined
363 hmmer, reciprocal BLAST and phylogenetic filtration (Liu, Storti et al. 2022) to identify
364 *Tara* Oceans meta-genes that reconcile exclusively with plastid-targeted proteins
365 from cultured diatom species, to the exclusion of non-diatom and non-plastid
366 homologs (**Fig. S8A**). Amongst the retained meta-genes likely to be N-terminally
367 complete (BLAST homology within the first 40 residues of a *P. tricornutum*
368 sequence), a majority have consensus plastid-targeting sequences (enolase: 38/ 78-
369 49%, PGAM: 58/ 97- 60%). Only a very small number (one enolase, 10 PGAM)

370 possess mitochondrial or endomembrane localizations, suggesting that they
371 principally correspond to plastid-targeted environmental homologs of each protein
372 (**Fig. S8B, Supplemental Dataset S3**, sheet 11).
373
374 Within *Tara* Oceans data, the greatest relative abundances of diatom cpEnolase and
375 cpPGAM1 were observed in meta-transcriptome (metaT) data in stations from both
376 high northern and southern latitudes (**Fig. 3**). We observed these trends concordantly
377 in both surface and deep chlorophyll maximum (DCM) samples from 0.8 - 2000 µm
378 size filtered (**Fig. 3A**); and in individual size fractions (0.8-3/5 µm, 5-20 µm, 20-180
379 µm, 180-2000 µm (**Fig. S9**), suggesting broad reproductibiilty across diatoms
380 independent of cell size and depth. These levels were notably greater than
381 equivalent levels in meta-genome (metaG) data (**Figs. 3B, S9**).
382
383 To confirm that this was due to a greater expression of cpPGAM and cpEnolase
384 genes, as opposed to being purely driven by the greater relative abundance of
385 diatoms in high latitude *Tara* Oceans stations, we performed multiple normalization
386 tests (**Fig. S10**; **Supplemental Dataset S3**, sheet 10). First, metaT abundances
387 calculated for each gene in the 0.8-2000 µm size fraction were divided by the total
388 relative abundance of all diatom metaT sequences, providing the total proportion of
389 each diatom meta-transcriptome occupied by cpEnolase and cpPGAM. These
390 normalisations showed positive correlations to latitude in both surface and DCM
391 depth fractions, with the greatest relative abundances (> 0.1% total diatom mapped
392 transcripts) typically occurring in stations > 60° (**Fig. S10A**). The observed Pearson
393 correlations to latitude were significantly positive (surface cpEnolase $R^2 = 0.18$, $P <$
394 10^{-05}, cpPGAM1A $R^2 = 0.23$, $P < 10^{-05}$; DCM cpEnolase $R^2 = 0.53$, $P < 10^{-05}$,
395 cpPGAM1A $R^2 = 0.59$, $P < 10^{-05}$) (**Supplemental Dataset S3**, sheet 10). More
396 broadly across, the metaT-normalised relative abundance levels showed clearest
397 positive correlations to daylength and negative correlations to temperature. No other
398 parameters (e.g., nutrient concentrations) showed as clear correlations to chloroplast
399 glycolysis metaT relative abundances (**Supplemental Dataset S3**, sheet 10).
400
401 Alongside this, the metaT abundances obtained for diatom cpEnolase and cpPGAM
402 genes were compared (via log normalisation, to allow the inclusion of zero values) to
403 the relative abundances calculated for the meta-genomic (metaG) sequences of the

404 same genes (**Fig. S10B**). This can be taken as an indicative measurement of the
405 relative ratio of transcript versus gene abundances for each meta-gene, i.e. in effect
406 its expression level. These measurements showed a weaker but still significant
407 positive correlation to latitude for cpEnolase surface fractions (R^2 = 0.10, one-tailed
408 *F*-test, P < 0.05) and for both genes in DCM fractions (cpEnolase R^2 = 0.28, one-
409 tailed *F*-test P < 0.05, cpPGAM1 R^2 = 0.29, one-tailed *F*-test P< 0.05 (**Supplemental**
410 **Dataset S3**, sheet 10). For both genes and in both depth fractions, two individual
411 stations within the Arctic (Station 173, 78.93-78.96°N; Station 188, 78.25°-78.36°N)
412 were observed to have extremely high metaT to metaG ratios (($\log_{10}$(1+metaT)-
413 $\log_{10}$(1+metaG)) > 3-5) that disrupted the linear relationship between normalised
414 metaT and latitude and point to specifically high expression of chloroplast glycolysis
415 genes in polar waters. To correct for the impacts of these stations, ranked
416 (Spearman) correlation values were also calculated for normalised chloroplast
417 glycolysis metaT expression levels. Significant positive correlations with latitude were
418 detected in multiple individual size fractions and depths (0.8-5, 3/5-20, 20-180, 180-
419 2000 µm), including for cpPGAM1 metaT normalised against metaG in surface 3/5-
420 20 (one-tailed *F*-test, P < 10^{-05}), 20-180 (one-tailed *F*-test; P < 10^{-05}) and 180-2000
421 (one-tailed *F*-test, P < 0.05) µm fractions (**Supplemental Dataset S3**, sheet 10).
422
423 The transcriptional preference of diatom cpEnolase and cpPGAM1 for high latitudes
424 contrasted strongly with PGAM2, which showed equivalent relative abundance in
425 stations from the temperate South Pacific and Atlantic as stations from the Arctic and
426 Southern Oceans (**Fig. S11**; **Supplemental Dataset S3**, sheet 10). In certain size
427 fraction and depth combinations (e.g., DCM 0.8-3, and 3/5-20 µm fractions,
428 normalised against metaG abundances; and surface and DCM 180-2000 µm
429 fractions normalised against all diatom metaT abundances) PGAM2 metaT
430 abundances even demonstrated significant negative correlations to latitude
431 (**Supplemental Dataset S3**, sheet 10).
432
433 Finally, we tested whether the occurrence of plastidial lower glycolysis may correlate
434 to algal abundance at high latitudes. For this, we screened single-cell and meta-
435 genome assembled genomes (sMAGs) from *Tara* Oceans for potential plastid-
436 targeted Enolase and PGAM enzymes, using similar reciprocal BLAST best hit,
437 PFAM annotation and *in silico* targeting prediction techniques as previously used for

438 cultured algae (**Fig. S12**; **Supplemental Dataset S**3, sheet 11) (Delmont, Gaia et al.
439 2022). We emphasise these results are preliminary, as many of these genomes are
440 incomplete, and gene non-detection does not formally confirm absence (Delmont,
441 Gaia et al. 2022, Pierella Karlusich, Nef et al. 2023). For each sMAG, we considered
442 presence or absence of possible plastid-targeted Enolase and PGAM sequences;
443 taxonomic assignation of the MAG; and mean mapped vertical coverage of each
444 MAG in each station (i.e., depth and breadth of the coverage of sequences recruited
445 to each genome), as a proxy for abundance, regardless of whether the plastid-
446 targeted glycolysis genes associated with each sMAG were detected (**Fig. S12**).
447
448 Across 291 eukaryotic algal sMAGs, 32 were found to possess both plausible
449 cpEnolase and cpPGAM proteins, and a further 84 could be assigned either one or
450 the other (**Fig. S12**). As expected, diatoms were found to possess plastid-targeted
451 glycolysis much more frequently than other groups, with 17/ 49 of the diatom sMAGs
452 found to possess both chloroplast-targeted Enolase and PGAM enzymes, and a
453 further 20 one of the two only (**Fig. S12**). We also detected probable complete plastid
454 glycolysis pathways in 10 further sMAGs belonging to lineages (pelagophytes,
455 dictyochophytes, haptophytes, chrysophytes, and bolidophytes) previously inferred to
456 possess complete plastid-targeted glycolysis pathways amongst cultured species
457 (**Fig. S2, S3**). Surprisingly, given the relative paucity of this pathway in cultured
458 primary green algae, we finally identified fiuve putative chlorophyte sMAGs with both
459 plausible cpEnolase and cpPGAM1A proteins (**Fig. S12**). All five of these sMAGs
460 (TARA_AON_82_MAG_00297, AOS_82_MAG_00181, ARC_108_MAG_00063,
461 ARC_108_MAG_00100, and PSW_86_MAG_00289) are assigned as novel
462 members of the genus *Micromonas* which is abundant at high latitudes (Lovejoy,
463 Vincent et al. 2007, Worden, Lee et al. 2009, Delmont, Gaia et al. 2022). Of note, no
464 cultured *Micromonas* are inferred to possess this pathway **(Supplemental Dataset**
465 **S1,** sheet 1). We therefore infer, in particular, that the recurrent *Micromonas* sMAG
466 isoform may be a novel plastid glycolysis pathway specific to uncultivated taxa.
467
468 Considering the biogeography of each sMAG, we note that diatoms that possess
469 complete lower half plastidial glycolysis pathways shows positive correlations
470 between mean mapped vertical coverage and absolute station latitude, albeit only in
471 DCM fractions (**Fig. S12A**; r= 0.517, P< 0.001, while positive correlations to lartitude

472 were observed for diatom sMAGs possessing one of cpEnolase or cpPGAM only
473 atboth depths (**Fig. S12A**; surface *r*= 0.313, two-tailed *t*-test P= 0.003, DCM *r*= 0.614,
474 P< 0.001). This trend was not however observed for diatom sMAGs lacking plastid-
475 targeted copies of both proteins, which showed non-significant and even weakly
476 negative correlations to absolute latitude (**Fig. S12A**; surface *r*= -0.069, DCM *r*=
477 0.192, P> 0.1). No clear association between plastidial lower half glycolysis and
478 occupancy at high latitudes was observed for other algal groups, with the exception
479 of chlorophytes, in which the presence of both cpEnolase and cpPGAM1A showed a
480 strong association with abundance in high (and particularly) Arctic latitude stations
481 (surface *r* = 0.508, P< 0.001; DCM *r* = 0.386, P = 0.017; **Fig. S12B, S12C**).
482
483 *Growth and photo-physiology of* Phaeodactylum *cpEnolase and cpPGAM1A*
484 *knockouts across light and temperature conditions*
485
486 We generated homozygous CRISPR knockout lines for both cpEnolase and
487 cpPGAM1A in the model diatom *P. tricornutum*. cpPGAM1A was selected over other
488 PGAM (cpPGAM1B, cpPGAM2) isoforms because of its transcriptional co-regulation
489 to cpEnolase and occurrence in measurable quantities in plastid proteome data (**Fig.**
490 **S6**; **Supplemental Dataset S2**) and latitudinal expression correlation in *Tara* Oceans
491 (**Figs. 3, S11**).
492
493 Multiple CRISPR knockout lines were generated from two regions with unique
494 sequences in the *P. tricornutum* genome for each gene (cpEnolase CRISPR region 1
495 *n*= 4, CRISPR region 2 *n*= 3; cpPGAM1A CRISPR region 1 *n*= 2, CRISPR region 2
496 *n*= 3) (**Fig. S13A**). Each CRISPR line was verified by sequencing to be homozygous
497 and to contain a frame-shift mutation sufficient to impede translation of the encoded
498 protein (**Fig. S13A**). Commercial antibodies against enolase and PGAM were found
499 not to specifically label cpEnolase and cpPGAM1A in Western Blots, and so we
500 inferred protein relative expression level by qRT-PCR using recognised *P.*
501 *tricornutum* housekeeping genes as above (Sachse, Sturm et al. 2013, Zhang,
502 Sampathkumar et al. 2020). The measured knockout mRNA abundance in each line
503 was significantly lower (1.8-39 %) than that identified in empty vector control mRNA
504 (*n* = 4, one-way ANOVA, P < 0.05) 19C LD conditions, **Fig. S13B**). This is consistent

505 with effective knockdown of mutated genes e.g., via non-sense mediated decay
506 (Chang, Imam et al. 2007).
507
508 Next, we performed growth curves of cpEnolase and cpPGAM1A knockout lines
509 compared to empty vector controls (**Fig. 4**; **Supplemental Dataset S4**, sheets 3-6).
510 We chose to target changes in light and temperature, given that both show clear
511 associations observed with cpPGAM1A and cpEnolase in *Phaeodactylum* gene
512 expression and *Tara* Oceans data (**Fig. 2, 3**), using the three conditions (19C CL,
513 19C LD, and 8C CL) previously tested for qRT-PCR. We note that these conditions
514 are relevant to the environmental conditions in which the type culture of
515 Phaeodactylum (strain CCAP 1055/1) was collected (Irish Sea, 53.5°N) with
516 measured sea temperatures (1960-1999) between 3°C and 17°C ; and day lengths
517 between 7 and 17 hours (Young and Holt 2007, Gachon, Heesch et al. 2013).
518
519 Under 19C LD conditions, plastid glycolysis-gluconeogenesis knockout lines showed
520 an approximately 10-15% reduction in relative growth rate compared to empty vector
521 controls (cpEnolase growth rate 0.83± 0.06 cells day$^{-1;}$ cpPGAM1A growth rate 0.85±
522 0.07 cells day$^{-1;}$ empty vector growth rate 0.94 ± 0.05 cells day^{-1}; **Fig. 4, S14;**
523 **Supplemental Dataset S4**, sheet 3; cpEnolase growth rate 87.7% control and
524 cpPGAM1A growth rate 90.1% control, one-way ANOVA, two-tailed $P < 0.05$).
525 Under 19C CL, knockout lines showed a 25-30% reduction in relative growth rate
526 compared to controls (cpEnolase growth rate 0.99± 0.16 cells day^{-1}; cpPGAM1A
527 growth rate 1.08± 0.04 cells day^{-1}; empty vector growth rate 1.39 ± 0.09 cells day^{-1};
528 **Fig. 4, S14**; **Supplemental Dataset S4**, sheet 4; cpEnolase growth rate 70.7%
529 control and cpPGAM1A growth rate 77.5% control, one-way ANOVA, two-tailed $P <$
530 0.01). Under 8C C, overlapping growth rates were observed for knockout and control
531 lines, albeit with a possible reduction in cpEnolase knockout growth rate (cpEnolase
532 relative growth rate 0.49± 0.10 cells day^{-1}, cpPGAM1A growth rate 0.64± 0.02 cells
533 day^{-1}, empty vector growth rate 0.62± 0.07 cells day^{-1}; **Fig. 4, S14; Supplemental**
534 **Dataset S4**, sheet 5; cpEnolase growth rate 78.1% control and cpPGAM1A growth
535 rate 102.9% control; one-way ANOVA, two-tailed P non-significant).
536
537 To test the possibility of off-target effects of the CRISPR constructs, we
538 complemented mutant lines with blasticidin resistance genes linked to either

539 cpEnolase-GFP or cpPGAM1A-GFP modified to remove all CRISPR target
540 sequences (**Supplemental Dataset S4**, sheet 2) (McCarthy, Smith et al. 2017, Buck,
541 Río Bártulos et al. 2018). Despite an overall lower growth rate in all blasticidin-
542 resistant lines compared to primary transformants, and within-line variation,
543 comparative growth curves of 47 complemented versus placebo transformed mutant
544 lines revealed increased growth rates in complemented cpEnolase and cpPGAM1A
545 versus blank transformed knockout lines under 19C CL and 19C LD (**Supplemental**
546 **Dataset S4**, sheet 7; one-way one-way ANOVA, two-tailed P, < 0.05). By contrast,
547 complemented knockout line growth rates overlapped with empty vector controls
548 either transformed with cpEnolase or blank complementing vectors, indicating
549 effective recovery of mutant phenotypes (**Supplemental Dataset S4**, sheet 7).
550
551 Finally, we performed comparative photophysiological measurements of knockout
552 lines in the two conditions (19C LD and 19C CL) where they presented a growth
553 phenotype (see Methods). Our data indicate that the presence/ absence of these
554 enzymes does not significantly impact photosynthetic performance. The light
555 dependencies of either electron transfer rate through photosystem II (PSII) (rETR(II))
556 or photoprotection (non-photochemical quenching, NPQ) were very similar between
557 control and knock-out lines (**Fig. S15A**; **Supplemental Dataset S4**, sheets 8-11). A
558 slight but significant increase in the functional absorption cross-section of
559 photosystem II (σPSII) was found under 19C CL in both cpEnolase (319.3± 22.5) and
560 cpPGAM1A knockouts (306.6± 11.6) compared to controls (292.3± 8.2; one-way
561 ANOVA, P < 0.05) (Gorbunov, Shirsin et al. 2020). This elevation was suppressed in
562 both complemented lines (**Fig. S15B**; **Supplemental Dataset S4**, sheet 11).
563
564 *Gene expression profiling of* Phaeodactylum *cpEnolase and cpPGAM1A knockouts*
565
566 Next, we investigated the impacts of disruption of plastid glycolysis on diatom
567 metabolism beyond photosynthesis. First, we performed quantitative RNA-seq
568 analysis using 63 RNA samples drawn from multiple knockout and empty vector lines
569 under all three physiological conditions (19C LD, 19C CL, and 8C CL; **Supplemental**
570 **Dataset S5**, sheet 1; Materials and Methods). 8C CL was targeted despite the
571 absence of a growth phenotype associated with this line due to the high levels of
572 cpEnolase and cpPGAM1A gene expression inferred from qRT-PCR data (**Fig. 2B;**

573 **Fig. 4**) Complete results are provided in **Supplemental Dataset S5**, sheets 5-11.
574 Both cpEnolase and cpPGAM1A mRNA were found to significantly under-accumulate
575 in the corresponding knockout lines, consistent with qRT-PCR analysis (**Fig. S13B**)
576 and suggesting maintenance of the mutant genotypes throughout RNA sequencing;
577 while cpPGAM1B (Phatr3_J51404) but not cpPGAM2 (Phatr3_J37201) was
578 upregulated in cpPGAM1A knockouts but not cpEnolase knockouts under 19C CL
579 conditions, which may suggest compensatory functions between cpPGAM1A and
580 cpPGAM1B (**Supplemental Dataset S5**, sheet 12**).**
581
582 Genome-scale enrichment analyses of the *in silico* localizations of proteins encoded
583 by differentially expressed genes revealed distinctive changes in glycolysis knockout
584 organelle metabolism. These effects were most evident in 19C CL, in which 90/239
585 (38%) of the genes differentially upregulated (mean fold-change >2, P-value < 0.05)
586 in both cpEnolase and cpPGAM1A knockout lines compared to controls were
587 predicted to possess chloroplast targeting sequences based on ASAFind (Gruber,
588 Rocap et al. 2015) or HECTAR (Gschloessl, Guermeur et al. 2008). This was
589 significantly greater than the proportion of genes (1,585/11,514, 14%) across the
590 entire genome predicted to encoding chloroplast-targeted proteins that were detected
591 in RNAseq data (one-tailed chi-squared $P < 10^{-05}$; **Fig. 5A; Supplemental Dataset**
592 **S5**, sheet 10). These results were supported by domain enrichment analyses,
593 indicating significant (one-tailed chi-squared P < 0.05) enrichments in light-harvesting
594 complex (GO:0030076), photosynthesis (GO:0009765) and protein-chromophore
595 linkage (GO:0018298) GO terms. A more detailed resolution of gene expression
596 patterns underpinning core organelle metabolism pathways (Ait-Mohamed, Novák
597 Vanclová et al. 2020) suggested concerted upregulation of genes encoding light-
598 harvesting complexes and photosynthesis machinery and plastid fatty acid synthesis
599 machinery, alongside a probable upregulation of mitochondrial respiratory complex I
600 and ATP synthase (**Supplemental Dataset S5**, sheets 10-11). Less dramatic
601 changes were evident in 19C LD and 8C CL, although 13 of the 51 genes (25%)
602 inferred to be downregulated in both cpEnolase and cpPGAM1A knockout lines
603 under 8C CL were inferred to encode chloroplast-targeted proteins by either ASAFind
604 or HECTAR, representing likewise an enrichment compared to all genes identified
605 within the RNAseq data (one-tailed chi-squared P < 0.05; **Fig. 5A**).
606

607 To gain a more precise insight into the effects of plastid glycolysis-gluconeogenesis
608 on *P. tricornutum* metabolism, we additionally validated the differential expression of
609 eleven exemplar genes encoding chloroplast- and mitochondria-targeted proteins by
610 qPCR in knockout and empty vector control lines across all three conditions (**Fig. 5B**;
611 **Supplemental Dataset S5**, sheet 12). These genes showed relatively limited
612 differences under 19C LD, limited to a slight depression in the accumulation of *Lhcf1*
613 (Phatr3_J18049) and chorismate mutase (Phatr3_J43277) mRNA in both cpEnolase
614 and cpPGAM1A knockouts compared to control lines (~50% downregulation, two-
615 tailed *t*-test $P < 0.05$; **Fig. 5B**). Both knockout lines over-accumulated (>600%; two-
616 tailed *t*-test $P < 10^{-05}$) mRNAs encoding mitochondrial phospho-glycerate mutase
617 (Phatr3_J33839) under 19C LD compared to control lines (**Fig. 5B**).
618
619 Under 19C CL, we observed more substantial changes in plastid metabolism,
620 including the significant (two-tailed *t*-test $P < 0.05$) over-accumulation of mRNAs
621 encoding Lhcf1 (~150%), a plastid-targeted petB-type protein presumably involved in
622 cytochrome b_6f metabolism (Phatr3_J13558, ~90%), and a particularly strong over-
623 accumulation of plastid lysophosphatidyl acyltransferase (LPAT), involved in plastid
624 lipid synthesis (Phatr3_J20640, ~100%, two-tailed *t*-test $P < 10^{-05}$) in both knockout
625 lines (**Fig. 5B**). Significant over-accumulations were also observed of mRNAs
626 encoding plastid signal processing peptidase (Phatr3_J10319, 60-120%), alanine
627 transaminase (Phatr3_J34010) and coporphyrinogen oxygenase (Phatr3_J12186), in
628 either cpEnolase or cpPGAM1A knockout lines (**Fig. 5B**). Concerning mitochondrial
629 metabolism, a strong increase (>250%, two-tailed *t*-test $P < 10^{-05}$) was observed in
630 mRNA for NDH dehydrogenase subunit 1 (Phatr3_J43944), involved in oxidative
631 phosphorylation, but a corresponding decrease (>40%, two-tailed *t*-test $P < 10^{-05}$) in
632 mRNA for citrate synthase within the TCA cycle (Phatr3_J30145).
633
634 Finally, under 8C CL, contrasting and complementary changes were observed: up-
635 regulation (>60%; two-tailed *t*-test $P < 10^{-05}$) of genes encoding both the plastid
636 signal processing peptidase and petB-related protein, and mitochondrial PGAM and
637 citrate synthases in both knockout lines compared to controls (**Fig. 5B**). Both
638 knockout lines were found to under-accumulate *Lhcf1* mRNA (>90%; two-tailed *t*-test
639 $P < 10^{-05}$), while *Lhcx4* (Phatr3_J38720), encoding a dark-expressed gene of
640 unknown direct function but homologous to the Lhcx1 protein implicated in

641 photoprotection (Buck, Sherman et al. 2019), was found to substantially over-
642 accumulate in both cpEnolase and cpPGAM1A knockout lines (**Fig. 5B**).
643
644 *Metabolite profiling of* Phaeodactylum *cpEnolase and cpPGAM1A knockouts*
645
646 Next, we considered the compound effects of cpEnolase and cpPGAM1A knockout
647 on global metabolite accumulation under each environmental condition via GC-MS
648 profiling of 32 sugars and amino acids (**Fig. 6; Fig. S16**), across 139 samples drawn
649 from multiple knockout and control lines under 19C LD, 19C CL and 8C CL. These
650 samples were obtained from cell pellets collected from mid-exponential phase
651 cultures, and thus correspond to the long-term impacts on metabolite accumulation in
652 actively growing plastid glycolysis knockout lines. Complete outputs are tabulated in
653 **Supplemental Dataset S6**, sheets 1-2.
654
655 We were unable to directly measure the accumulation of any of the products or
656 substrates of either cpPGAM1A or cpEnolase (3-phosphoglycerate, 2-
657 phosphoglycerate, PEP), although we detected significantly diminished (one-way
658 ANOVA two-tailed P-value < 10^{-05}) pyruvate accumulation, as a metabolite
659 synthesised from PEP (by pyruvate kinase), in cpPGAM1A knockouts under all three
660 conditions, and in cpEnolase knockouts under 8C CL (**Fig. 6, S16**). We similarly
661 could not directly measure the accumulate of glyceraldehyde-3-phosphate (the
662 substrate for PGAM), but could detect an overaccumulation of glycerol-3-phosphate
663 (synthesised from glyceraldehyde-3-phosphate by glycerol-3-phosphate
664 dehydrogenase) in cpEnolase knockout lines under all three conditions (**Fig. 6**).
665
666 In all three conditions, significant reductions (one-way ANOVA two-tailed P-value <
667 0.01 in both cpEnolase and cpPGAM1A knockout lines) were observed in
668 cytoplasmic sugars and sugar derivatives (glucose, sucrose, histidine, *myo*-inositol)
669 in cpEnolase and cpPGAM1A knockouts compared to control lines (**Fig. 6**).
670 cpEnolase and cpPGAM1A knockout lines further under-accumulated citric acid in all
671 three conditions, and malic acid in 8C CL (**Fig. 6**). A probable over-accumulation of
672 phosphoric acid was observed in all knockout lines except cpPGAM1A under 19C CL
673 (**Fig. 6; S17**). Significant (one-way ANOVA two-tailed P-value < 10^{-05}) over-
674 accumulations were identified for valine in cpEnolase and cpPGAM1A knockouts

675 under 19C CL and 8C CL; for methionine and ornithine in 19C CL only; and an
676 under-accumulation for arginine under 19C CL only (**Fig. 6**).
677
678 Finally, specific differences were observed in the metabolite accumulation patterns
679 observed in cpEnolase and cpPGAM1A knockout lines (**Fig. 6; S16**). These include a
680 significant (one-way ANOVA two-tailed P-value < 10^{-05}) over-accumulation of three
681 amino acids (aspartate, leucine and phenylalanine) and one sugar phosphate
682 (glycerol-3-phosphate) specifically in cpEnolase knockout lines under all three
683 conditions, and in serine under 19C CL and 8C CL only. These differences contrast
684 to cpPGAM1A knockouts in which no significant changes were observed.
685 Surprisingly glycerol-3-phosphate and serine were found to significantly under-
686 accumulate under all three conditions in cpPGAM1A knockouts compared to controls
687 **(Fig. 6**; **S16**).
688
689 *Lipid profiling of* Phaeodactylum *cpEnolase and cpPGAM1A knockouts*
690
691 Next, we performed GC-MS (55 samples) and LC-MS (49 samples) of lipid profiles in
692 multiple knockout and control lines under 19C LD, 19C CL and 8C CL. Outputs are
693 tabulated in **Supplemental Dataset S6**, sheets 1, 3-5. While the GC-MS data project
694 significant (one-way ANOVA two-tailed P-value < 0.05) impacts of growth condition
695 on fatty acid profiles (e.g., a decrease of C20:5 side chain lipids balanced by an
696 increase of C16:1 side chain lipids in 19C CL, and an over-accumulation of C16:3
697 side chain lipids under 19C LD, and of C18:0 side chain lipids under 8C CL), no
698 substantial differences were observed between cpEnolase, cpPGAM1A and control
699 lines under any conditions studied (**Supplemental Dataset S6,** sheet 3).
700
701 In contrast to the relatively limited effects on total fatty acid profiles, LC-MS analyses
702 of lipid class distributions revealed substantial changes in lipid class distribution in
703 plastid glycolysis-gluconeogenesis knockout lines (**Fig. 7**; **Supplemental Dataset**
704 **S6,** sheet 4). Even accounting for within-line variation, both cpEnolase and
705 cpPGAM1A knockouts were found to significantly under-accumulate triacylglycerols
706 (TAG) (cpEnolase 3.98 ± 1.94%, cpPGAM1A 3.60 ± 1.72%, control 12.18 ± 7.26%;
707 one-way ANOVA, two-tailed P separation of means between knockout and control
708 lines < 0.05) and over-accumulate monogalactosyldiacylglycerols (MGDG; cpEnolase

709 63.83 ± 4.33%, cpPGAM1A 60.89 ± 5.64%, control 49.68 ± 8.88%; one-way ANOVA,
710 two-tailed P< 0.05) under 19C LD (**Fig. 7A**). Further significant (P < 0.05) under-
711 accumulations were detected in knockout lines for diacylglycerols (DAG) and
712 sulfoquinovosyl-diacylcerols (SQDG) under 19C LD. Similar tradeoffs were observed
713 under 19C CL, albeit with an over-accumulation, rather than under-accumulation of
714 DAG, and an additional under-accumulation of digalactosyldiacylglycerols (DGDG),
715 in glycolysis knockouts compared to control lines (**Fig; 6B**).
716
717 Detailed analyses of the individual fatty-acid side-chains associated with different
718 lipid classes in glycolysis knockout lines under 19C indicated increased relative
719 contributions of C16:1 fatty acids to plastid membrane lipid *sn*-1 positions
720 (**Supplemental Dataset S6,** sheet 5). These included conserved (P < 0.01) over-
721 accumulations of DGDG-16-1_16-2 under 19C LD **(Fig. S18)**; and SQDG 16-1_16-0,
722 MGDG-16-1_16-2, MGDG-16-1_16-3 and DGDG-16-1_16-1, in both cpEnolase and
723 cpPGAM1A knockout lines under 19C CL (**Fig. S19**). A significant over-accumulation
724 of 16-1_16-1 side chains and under-accumulation 20-5_18-4 was also observed for
725 diacylglyceryl hydroxymethyltrimethyl-*β*-alanine (DGTA), a betaine lipid known to act
726 as a platform for the biosynthesis of 20:5 fatty acids, in both cpEnolase and
727 cpPGAM1A knockout lines under 19C LD (**Fig. S18**) (Dolch and Maréchal 2015,
728 Popko, Herrfurth et al. 2016).
729
730 Under 8C CL, quite different trends were observed in fatty acid accumulation in
731 cpEnolase knockouts compared to cpPGAM1A knockouts and controls. These
732 correlated principally with an over-accumulation of TAG (cpEnolase 20.88 ± 12.21%,
733 cpPGAM1A 9.62 ± 6.31%, control 8.15 ± 3.95%; one-way ANOVA, two-tailed P <
734 0.05) in lieu of MGDG (cpEnolase 34.20 ± 6.74%, cpPGAM1A 42.94 ± 6.01%, control
735 46.61.3 ± 6.25%; one-way ANOVA, two-tailed P < 0.5; **Fig. 7A**). An over-
736 accumulation of SQDG was observed in both cpEnolase and cpPGAM1A knockouts
737 compared to controls, albeit with greater severity in cpEnolase knockouts (**Fig. 7B**).
738 Considering side-chain distributions of individual lipid classes, a significant (one-way
739 ANOVA two-tailed P-value < 0.01) over-accumulation of short-chain (C14:0, C16:1)
740 and *sn*-1 and *sn-2* fatty acids was observed in cpEnolase knockouts (**Fig. S20A**). A
741 probable exchange of very long-chain *sn*-2 fatty acids in SQDG pools was further
742 observed in cpEnolase knockouts, with significant (one-way ANOVA two-tailed P-

743 value < 0.01) increases in SQDG 14-0_16-0 and SQDG-14_0-16-1 in lieu of SQDG-
744 16-2_24-0 in cpEnolase knockouts compared to cpPGAM1A and control lines (**Fig.**
745 **S20B**; **Supplemental Dataset S6**, sheet 5).
746
747 *Reaction kinetics of expressed copies of* Phaeodactylum *cpEnolase and cpPGAM1A*
748
749 Finally, we assessed the kinetics of cpPGAM and cpEnolase in both glycolytic and
750 gluconeogenic directions. Previous studies (e.g., in animal renal and liver tissue)
751 project reversible reaction kinetics for both enolase and PGAM enzymes. The
752 reaction rates of enolase and PGAM show limited difference in glycolytic versus
753 gluconeogenic directions *in vivo*, with measured enolase rates in rat kidney tissue
754 equivalent to approximately 14,000 µmol g dry weight^{-1} hr^{-1} in the glycolytic direction,
755 and 20,000 µmol g dry weight^{-1} hr^{-1} in the gluconeogenic direction (KREBS 1963,
756 Scrutton and Utter 1968, Reinoso, Telfer et al. 1997). Equally, purified enolase and
757 PGAM typically show greater affinity for 3-PGA than PEP, with a 5-8 fold difference in
758 Km measured in mammalian, yeast and *Trypanosoma brucei* enzymes (Rider and
759 Taylor, 1974; Hannaert et al., 2003).
760
761 Using a previously defined assay (Sutherland, Posternak et al. 1949, Zhang,
762 Sampathkumar et al. 2020) with modified versions of each protein (codon-optimised,
763 and lacking signal peptides) expressed in *E. coli,* alongside measured NADH
764 consumption coupled to either lactate dehydrogenase (glycolysis) or glyceraldehyde-
765 3-phosphate dehydrogenase (**Fig. S20**). Both enzymes were inferred to possess
766 reversible reaction kinetics, metabolizing NADH when supplied both with 3-PGA (in
767 the glycolytic direction) and PEP (in the gluconeogenic direction; **Fig. 8, Fig. S20**).
768 The measured reaction rates were effectively reversible, albeit marginally greater in
769 the glycolytic than gluconeogenic direction (e.g., 2.47 ± 0.43 versus 1.97 ± 0.29 nMol
770 NADH consumption per gram free weight purified enzyme per minute when supplied
771 with12 mM 3PGA or 12 mM PEP; **Fig. 8**).
772
773 **Discussion**
774
775 We characterise a lower glycolytic-gluconeogenic pathway associated with diatom
776 plastids, relating specifically to two plastid-targeted proteins, cpEnolase and

cpPGAM1A, and focusing on the model species *P. tricornutum*. Our data position plastid glycolysis-gluconeogenesis as arising in a recent ancestor of diatoms and their closest relatives (e.g., pelagophytes, dictyochophytes) (Nonoyama, Kazamia et al. 2019). The presence of plastid glycolysis in haptophytes may be as a result of endosymbiotic transfers into this group from a pelagophyte/ dictyochophyte-related alga, as suggested in previous studies (Dorrell, Gile et al. 2017, Jiang, Cao et al. 2023). We further show that plastidial lower glycolysis-gluconeogenesis has a limited distribution across the algal tree of life, with no examples in primary red and few in primary green algae (**Fig. S1, S12**). It is possible that the occurrence of organelle-targeted isoforms of these enzymes is underestimated, e.g., due to lower sensitivity of diatom and plant-trained targeting predictors on other algal groups (Fuss, Liegmann et al. 2013, Gruber, Rocap et al. 2015). We propose that diatom plastid glycolysis most likely originated through the duplication and retargeting of mitochondrial respiratory enzymes (**Fig. 1**).

Using meta-genomic data from *Tara* Oceans we demonstrate that diatom plastid glycolysis is likely highly expressed at high latitudes (**Figs. 3, S8-S11**), which are subject to extreme photoperiods and low temperature. These data are further supported by collection sites of cultured species, with no occurrences of cultured diatoms lacking plastid-targeted PGAM enzymes beyond 50°N (**Fig. S1B**), and evidence from meta-genome assembled genomes, in which diatoms that possess apparent plastid-targeted Enolase and PGAM enzymes show an associative preference for high latitudes, while those that lack them do not (**Fig. S12**). These enrichments appear to be largely specific to diatoms, with polar circle haptophytes, cryptomonads and other ochrophytes lacking apparent plastidial glycolysis found further than 60°N and 70°S, considering both cultured species and MAG data, although with a potential parallel recruitment of plastidial glycolysis to isolates of the prasinophyte genus *Micromonas* abundant in high latitude *Tara* stations (Lovejoy, Vincent et al. 2007). We thus tentatively propose that lower half plastid glycolysis correlates to diatom occurrence in high latitude *Tara* Oceans stations, with diatoms that lack identifiable copies of these proteins absent from these stations, and other algal groups (except potentially chlorophytes) showing no preference for plastidial glycolysis at high latitudes.

811 We are hesitant to state that plastid glycolysis is an adaptive feature of diatoms
812 towards high latitudes, given it apparently originated in a common ancestor of
813 diatoms and several other algal groups (i.e., pelagophytes, and dictyochophytes),
814 and is retained in species such as *Phaeodactylum* which is typically associated with
815 intermediate latitudes (Rastogi, Vieira et al. 2020). cpEnolase and cpPGAM cannot
816 therefore have been viewed to have been gained in specific diatom species in
817 response to environmental selection. An open question, particularly given the largely
818 latitude-insensitive distributions to diatom MAGs lacking plastid glycolysis, remains to
819 what extent diatoms that have secondarily lost their plastid glycolytic pathway are
820 abundant in nature (**Fig. S12**). Ultimately, the physiological functions of diatom
821 plastid glycolysis will be best identified through competition assays e.g. between
822 diatom species with different plastid carbon metabolism arrangements, or between
823 *Phaeodactylum* knockout and empty vector control lines under each condition
824 (Siegel, Baker et al. 2020).
825
826 Nonetheless, from our analysis of published *Phaeodactylum* transcriptome data and
827 qRT-PCRs, we note that both cpEnolase and cpPGAM1A genes are transcriptionally
828 induced in response to both long day conditions and low temperatures (**Fig. 2B, S7**).
829 These biases are particularly interesting given the growth analysis of *P. tricornutum*
830 knockout lines. In particular, we observe more intense growth defects in
831 *Phaeodactylum* lines under continuous illumination than in light: dark cycles (**Figs. 4,**
832 **S9**), which alongside gene expression data suggests increased importance of plastid
833 glycolysis in diatoms subject to long days. In contrast, under low temperatures no
834 difference was observed in the growth rate of glycolysis knockouts showed to control
835 lines (**Fig. 4**). We note that the relative expression of cpEnolase and cpPGAM1A are
836 even greater at 8C than 19C under continuous light conditions, and it is possible that
837 flux occurs through plastid glycolysis at low temperature despite the absence of a
838 clear growth phenotype in knockout versus control lines. We thus tentatively propose
839 that lower glycolysis-gluconeogenesis may have multiple functions in the diatom
840 plastid, with different functions dependent on both light and temperature conditions.
841
842 Considering the observed phenotypes of knockout and control lines (**Figs. 4-7; S14-**
843 **S19**) and the reversible kinetics of expressed enzymes, we suggest potential
844 functions contributed by the lower half of plastid glycolysis-gluconeogenesis in

845 diatoms under 19C LD, 19C CL and 8C CL conditions (**Fig. 8)**. Overall, our
846 suggested roles for cpEnolase and cpPGAM1A are predominantly in favour of
847 metabolic flux in the glycolytic direction, reflecting the underaccumulation of pyruvate
848 in cpPGAM1A knockouts, and overaccumulation of 3-phospho-glycerate in
849 cpEnolase knockouts (**Fig. 6**). We also present this hypothesis based on the innate
850 metabolic activity of the Calvin cycle, which is likely to yield a high relative
851 abundance of triose phosphate in the plastid under illuminated and photosynthetically
852 active conditions; although we note that studied diatom triose phosphate transporters
853 show higher transport affinity for PEP than DHAP, which may facilitate substrate
854 supply for gluconeogenic activity (Moog, Nozawa et al. 2020) (**Fig. 8**). These results
855 are nonetheless inferential based on the long-term accumulation patterns of stable
856 metabolites and the expression of implicated metabolic genes. Whilst these would be
857 more effectively validated via direct flux measurements, e.g., comparative ^{13}C-
858 glycerol or -glucose labelling of glycolysis knockout and control lines (Zheng, Quinn
859 et al. 2013, Huang, Liu et al. 2015), this was beyond the scope of the current study.
860
861 Under 19C LD, we observe limited gene expression changes in cpPGAM1A and
862 cpEnolase knockout lines, except (as inferred from qPCR) a downregulation in
863 plastid chorismate mutase, which forms part of the plastid shikimate pathway, that
864 typically consumes PEP (Bromke 2013) and may form a primary acceptor of
865 glycolytic products (**Fig. 5B**). One of the products of chorismate mutase activity,
866 phenylalanine, does seem to overaccumulate in metabolite pools of cpEnolase
867 mutants only under these conditions, pointing to potentially more complex fluxes
868 (discussed below). We also note an upregulation of mitochondrial PGAM in both lines
869 (**Fig. 5B**), which might relate to a greater level of mitochondrial glycolysis, e.g. of
870 exported plastid glyceraldehyde-3-phosphate in the knockout lines. Strikingly, both
871 mutant lines underaccumulate TCA cycle intermediates (citric acid in both lines, and
872 fumaric and malic acid in cpPGAM1A only) which may suggest less retention of
873 metabolised sugar in the mitochondrion. Finally, both mutants also underaccumulate
874 sugars typically synthesised in the cytosol (sucrose, myo-inositol) which we interpret
875 to imply less excess fixed carbon in the knockout compared to control lines (**Fig. 6**).
876 Overall these data seem to point to less efficient carbon usage, and an overall
877 redirection of plastidial triose phosphate from plastid or cytoplasmic anabolic
878 reactions to mitochondrial catabolism in knockout lines.

879

880 We also note some evidence for lipid remodelling in glycolysis mutant lines. These
881 include a relative over-accumulation of galactolipids in lieu of TAGs, and short-chain
882 fatty acids in lieu of longer equivalents (**Figs. 7, S18**). Previous studies have noted
883 the importance of lipid metabolism in diatom stress responses (Zulu, Zienkiewicz et
884 al. 2018), and that most or all diatom lipid synthesis occurs directly in the plastid
885 (Huang, Pan et al. 2024). Many of the metabolic reactions required for lipid synthesis,
886 including acyl-coA synthesis from pyruvate (Maréchal and Lupette 2020), glycerol-3-
887 phosphate from glyceraldehyde-3-phosphate (Kroth, Chiovitti et al. 2008), and
888 glucosyl-1-phosphate from cytoplasmic glucosyl-1-phosphate (Zhu, Shi et al. 2016),
889 are likely to be Impacted by plastid carbon metabolism. Specifically, an
890 underaccumulation of TAGs and fatty acids in lieu of galactolipids would also suggest
891 a lower ratio of pyruvate (for acyl-coA synthesis) to glyceraldehyde-3-phosphate (for
892 galactosyl-phosphate synthesis) in glycolysis knockout lines (Demé, Cataye et al.
893 2014), similarly to the underaccumulation of pyruvate observed in our metabolomic
894 data (**Fig. 6**). We infer that these changes are probably driven by substrate limitation,
895 as we observe no changes in the transcription of genes involved in fatty acid
896 synthesis in glycolysis knockout lines; nor do we increased expression of cpEnolase
897 or cpPGAM1A in cellular conditions (N and P limitation) known to induce diatom lipid
898 accumulation (**Fig. 5B**; **Fig. S7**) (Abida, Dolch et al. 2015)
899

900 Under 19C CL, we observed much more dramatic remodelling of cellular transcription
901 in knockout lines compared to controls (**Fig. 5A**). These are notably concordant with
902 greater expression of cpEnolase and cpPGAM1A in wild-type cells (**Fig. 2B**), and an
903 enhanced growth defect in knockout lines, together suggesting greater potential flux
904 through this pathway than under 19C LD (**Fig. 4B**). The transcriptional changes
905 include greater overall photosynthesis gene expression, e.g., *Lhcf1* (**Fig. 5B**), which
906 was corroborated in photo-physiological analyses by larger PSII antenna size, i.e., a
907 larger functional cross-section (σPSII) (**Fig. S15**). It should be noted that the increase
908 in PSII antenna size does not necessarily change the quantum yield of individual PSII
909 reaction centres, and therefore the increased σPSII is independent of the Fv/ Fm
910 measured, which remains equivalent between knockout and control lines (**Fig. S15**).
911 We did not observe consistent differences in the expression of nitrogen or
912 phosphorus stress metabolism, or in the expression of the *P. tricornutum* biophysical

913 carbon concentration mechanisms of knockout lines, suggesting that these
914 differences were not caused by N, P or CO_2 limitation in the control lines
915 (**Supplemental Dataset S5,** sheets 4-5) (McCarthy, Smith et al. 2017, Nawaly,
916 Matsui et al. 2023). We further did not measure differences in photosynthetic
917 performance (electron transport), or an upregulation of genes encoding proteins
918 involved in photoprotection, e.g., LhcX family or xanthophyll cycle enzymes in
919 knockout lines under 19C CL (**Fig. 5B**; **Fig. S15**; **Supplemental Dataset S4,** sheet
920 12) (Buck, Sherman et al. 2019, Bai, Cao et al. 2022), suggesting that the differential
921 expression of photosynthesis genes in the knockout lines does not directly influence
922 photosynthesis.
923
924 In contrast, from RNAseq and qRPCR we observed an upregulation of multiple
925 mitochondrial NDH dehydrogenase and ATP synthase subunits; and downregulation
926 of TCA cycle enzymes in glycolysis knockout lines (**Fig. 5B; Supplemental Dataset**
927 **S5,** sheet 12). Our metabolomic data further show an underaccumulation of citric
928 acid, as per in 19LD conditions; but also arginine, synthesised in the diatom
929 mitochondria from glutamate and aspartate in the urea cycle (Allen, Dupont et al.
930 2011, Bromke 2013). We globally interpret these phenotypes to mean an increase in
931 mitochondrial respiratory electron transport in glycolysis knockout lines without
932 necessarily an increase in mitochondrial primary metabolic activity. Previous studies
933 have noted the important role of diatom mitochondria in dissipating excess plastid
934 reducing potential (Bromke 2013, Bailleul, Berne et al. 2015, Broddrick, Du et al.
935 2019), and we wonder if these phenotypes observed in knockout lines under 19C CL
936 conditions relate to the respiratory dissipation of plastidial NADPH.
937
938 It remains to be determined what routes beyond plastidial glycolysis contribute
939 substrates (e.g. PEP, pyruvate) to the *P. tricornutum* pyruvate hub. Previous studies
940 have noted that diatom plastid triose phosphate transporters may be able to transport
941 PEP directly from the cytoplasm, and one of these (Phatr3_J54017) is indeed
942 upregulated in both cpEnolase and cpPGAM1A knockout lines under 19C CL
943 (**Supplemental Dataset S5**, sheet 3) (Moog, Nozawa et al. 2020, Liu, Storti et al.
944 2022). Elsewhere our data suggest that amino acids may modify the concentrations
945 of *P. tricornutum* plastid PEP and/or pyruvate. These data include the overexpression
946 of plastid alanine transaminase in cpPGAM1A knockouts (**Fig. 5B);** and the

947 overaccumulation in both knockout lines of amino acids synthesised either from
948 pyruvate (valine), PEP (aspartate via PEP carboxylase, and methionine from
949 aspartate), or more broadly involved in plastid amino acid recycling (ornithine and
950 glutamate, in the diatom plastid ornithine cycle) (Levering, Broddrick et al. 2016,
951 Smith, Dupont et al. 2019, Yu, Nakajima et al. 2022) (**Fig. 6**). The direction (import or
952 export) and significance of these amino acid fluxes will be best determined e.g. with
953 an inducible knockout mutant compromised for both plastidial glycolysis and amino
954 acid incorporation (e.g., via nitrate reductase) to allow direct metabolic quantification
955 of *de novo* synthesised amino acids (McCarthy, Smith et al. 2017, Yin and Hu 2023).
956
957 Under 8C CL, we identify an over-accumulation of mRNAs encoding plastid
958 biogenesis and mitochondrial glycolytic proteins, an over-accumulation of short-chain
959 amino acids (valine) and an under-accumulation of cytoplasmic sugars and amino
960 acids (glucose, histidine) in cpEnolase and cpPGAM1A knockouts relative to controls
961 (**Figs. 5B, 5**). We further note under-accumulations of pyruvate in both knockout
962 lines (**Fig. 6**). Knockout lines under 8C conditions, however, have additional
963 phenotypes not observed at 19C. These include an overall enrichment in down-
964 regulated genes encoding plastid-targeted proteins (**Fig. 5A**); and a specific over-
965 accumulation of TCA cycle (citrate synthase) and a possible non-photochemical
966 quenching-associated mRNA (*LhcX4*) (**Fig. 5B**) (Bailleul, Berne et al. 2015, Murik,
967 Tirichine et al. 2019). Finally, specific differences are observed between cpEnolase
968 and cpPGAM1A knockout lines at 8C. These include an overaccumulation of TAGs
969 and SGDQs over glucosyl-lipids, and the over-accumulation of aspartate and
970 phenylalanine in cpEnolase knockouts only (**Figs. 6, 7; S17**).
971
972 The more complex phenotypes observed in our knockout lines at 8C, and particularly
973 the differences between cpPGAM1A and cpEnolase knockouts, may be due to
974 several reasons. PGAM is typically viewed to have a greater catalytic activity than
975 Enolase from biochemical studies, although this may be compensated by the greater
976 relative abundance of cpEnolase than cpPGAM1A in *Phaeodactylum* plastids (**Fig.
977 S6A**) (Scrutton and Utter 1968, Huang, Pan et al. 2024). It is true that cpPGAM1A
978 may be compensated by functionally redundant proteins (cpPGAM1B, cpPGAM2) in
979 the *Phaeodactylum* plastid in knockout lines, whereas cpEnolase is functionally non-
980 redundant, but none of these genes are specifically induced in RNAseq data of

981 cpPGAM1A knockouts under 8C CL (**Supplemental Dataset S5**, sheet 3)
982 suggesting an absent of specific compensation in the cpPGAM1A mutant line. We
983 note that several of the phenotypes associated with 8C CL, and with cpEnolase
984 knockouts specifically, relate to accumulation either of acyl-coA (TAGs) or PEP
985 (aspartate, phenylalanine), which may suggest impediment of the gluconeogenic
986 rather than glycolytic activity of cpEnolase and cpPGAM. The reversibility of the
987 cpPGAM1A and cpEnolase reaction is confirmed by enzymatic data (**Fig. 8**), and it
988 remains to be determined to what extent these enzymes function bidirectionally *in*
989 *vivo*. It also remains to be determined how these functions impact on growth kinetics
990 and viability of diatoms in the wild, given the limited differences in growth rate
991 observed in the lab between knockout and control lines (**Fig. 4**).
992
993 The complex phenotypes for diatom plastid glycolysis inferred from environmental
994 and experimental data contrast with those for plant plastid glycolysis, with (for
995 example) *A. thaliana* cpEnolase and cpPGAM mutants presenting relatively limited
996 phenotypes (Prabhakar, Löttgert et al. 2009, Andriotis, Kruger et al. 2010). We note
997 that the cytoplasmic and respiratory plant Enolase and PGAM1 isoforms, alongside
998 having predominant impacts on plant carbon flux, also have important moonlighting
999 roles in plant development, immune responses and even in the structural
1000 coordination of plastids and mitochondria (Zhao and Assmann 2011, Zhang,
1001 Sampathkumar et al. 2020, Yang, Wang et al. 2022). We similarly anticipate that
1002 further surprises will be identified for the functions of diatom plastid glycolysis, and for
1003 this still poorly understood pathway in the photosynthetic tree of life.
1004
1005 **Materials and Methods**
1006
1007 *Culture conditions*
1008
1009 *Phaeodactylum tricornutum* strain Pt1.86 was grown in enhanced seawater (ESAW)
1010 medium supplemented with vitamins, but without silicon or added antibiotics, in 50 µE
1011 m^{-2} s^{-1} white light. Light profiles were measured with a SpectraPen photofluorometer
1012 (Photon Systems Instruments, Czech Republic); and are provided in **Supplemental**
1013 **Dataset S4**, sheet 13. Cultures were grown under one of four light, temperature and
1014 shaking regimes. For general molecular work and transformation, cultures were

1015 grown under 19 °C with 12h light: 12 dark cycling, shaken at 100 rpm (for general
1016 molecular work and transformation), following the established methodology of
1017 Falciatore et al. (Falciatore, Casotti et al. 1999). For comparative physiology work,
1018 we were unable to replicate shaking conditions at low temperatures, and therefore
1019 chose to use conditions without shaking: 19 °C with 12 h light: 12 h dark cycling
1020 (« LD » growth conditions and physiological analysis); 19 °C with 24 h continuous
1021 light and without shaking (« CL » growth conditions and physiological analysis); or
1022 8°C with 24h continuous light and without shaking (« 8C » growth conditions and
1023 physiological analysis). All cultures achieved measured mid exponential Fv/Fm
1024 values of > 0.6, suggesting that the absence of shaking did not impact on
1025 photosynthetic efficiency (**Supplemental Dataset S5**, sheet 8).
1026
1027 Batch culturing of *P. tricornutum* for genetic manipulation was performed under
1028 fluorescent lamps. Physiological experiments were principally performed at 19°C in
1029 an AlgaeTron AG230 (Photon Systems Instruments) with cool white LED (WIR)
1030 illumination, and technical specifications described in https://growth-
1031 chambers.com/data/algaetron-ag-230/download/AlgaeTron_AG_230_Manual2021-
1032 finalweb.pdf . Growth experiments were performed at 8°C using a low-temperature
1033 adapted cool white LED (WIR, ECCLIM). Details of all three spectra used, as
1034 measured with a SpectraPen (PSI), are provided in **Table S4**, sheet 13.
1035
1036 Mutant *P. tricornutum* lines were maintained on ½ ESAW 1% agarose plates,
1037 supplemented by 100 µg ml^{-1} each ampicillin and streptomycin, and 30 µg ml^{-1}
1038 chloramphenicol, and either 100 µg ml^{-1} zeocin (single transformants), or 100 µg ml^{-1}
1039 zeocin and 4 µg ml^{-1} blasticidin (complementation lines), as previously described
1040 (Falciatore, Casotti et al. 1999, Buck, Río Bártulos et al. 2018). All functional
1041 analyses of transformant lines were performed on transformant lines grown in the
1042 absence of antibiotic selection, to avoid secondary effects on growth or physiology.
1043
1044 *Phylogenetic identification of plastid lower half glycolysis-gluconeogenesis enzymes*
1045
1046 Plastid-targeted glycolysis lower half enzymes were searched across 1,673 plant and
1047 algal genomes and transcriptomes (**Dataset S1**, sheet 1). Briefly, this involved
1048 searching all annotated *P. tricornutum* PGAM (Phatr3_J17086, Phatr3_J51404,

1049 Phatr3_J5605, Phatr3_J5629, Phatr3_J8982, Phatr3_J37201, Phatr3_J47096) and
1050 enolase (Phatr3_draftJ1192, Phatr3_draftJ1572, Phatr3_J41515) peptide sequences
1051 with BLASTp and a threshold e-value of 10^{-05}, and a reciprocal BLASTp with criteria -
1052 max_target_seqs 1 to retrieve the best homologues against the entire *P. tricornutum*
1053 genome. For PGAM, where *P. tricornutum* queries failed to retrieve homologues in
1054 >50% searched libraries, a second BLASTp was performed with query peptide
1055 sequences from *A. thaliana* (AT2G17280, AT1G09780, AT3G05170, AT3G08590,
1056 AT3G50520, AT5G04120, AT5G64460), and a reciprocal BLASTp was performed
1057 with the *P. tricornutum* genome supplemented with these sequences. Similar
1058 approaches were subsequently used to identify equivalent plastid glycolysis proteins
1059 from *Tara* Oceans meta-genome assembled genomes (MAGs), as assembled in
1060 (Delmont, Gaia et al. 2022).
1061
1062 The domain content of each potential homologue was identified using hmmscan and
1063 the version 33.1 Pfam database (Mistry, Chuguransky et al. 2020). Only Enolase
1064 sequences that contained >90% predicted domain coverage to both Enolase_N and
1065 Enolase_C domains; and PGAM sequences that contained >50% domain coverage
1066 to the His_Phos domain (based on the corresponding coverage observed in *P.*
1067 *tricornutum* sequences) were viewed as being complete. Sequences for which the N-
1068 terminus of the region homologous to the PFAM domain was located within the first
1069 20 aa of the predicted sequence (i.e., less than the length of a typical plastid-
1070 targeting sequence) (Emanuelsson, Brunak et al. 2007) were viewed as lacking
1071 credible targeting sequences. All remaining proteins were scanned, considering both
1072 complete proteins and sequences trimmed to the first encoded N-terminal
1073 methionine, using targetp (using a plant scoring matrix) (Emanuelsson, Brunak et al.
1074 2007), PredAlgo (Tardif, Atteia et al. 2012), HECTAR (Gschloessl, Guermeur et al.
1075 2008) and ASAFind (with SignalP 5.0) (Gruber, Rocap et al. 2015, Almagro
1076 Armenteros, Tsirigos et al. 2019). Sequences from primary plastid-containing
1077 organisms (plants, green and red algae, glaucophytes) that were inferred to possess
1078 a plastid-targeting sequence either with TargetP or PredAlgo, and sequences from
1079 secondary plastid-containing organisms that were inferred to possess a plastid-
1080 targeting sequence with either HECTAR or ASAFind, considering both complete and
1081 N-trimmed sequence models, were annotated as putatively plastid-targeted.
1082

1083 A more detailed phylogenetic analysis was performed using Enolase and PGAM
1084 homologues obtained from a subset of 289 complete cryptomonad, haptophyte and
1085 stramenopile genomes and transcriptomes in the above library, alongside
1086 homologues identified from a further 85 prokaryotic and eukaryotic genomes
1087 sampled with taxonomic balance from across the remainder of the tree of life (Liu,
1088 Storti et al. 2022). Sequences were also screened for mitochondrial presequences
1089 using HECTAR (Gschloessl, Guermeur et al. 2008), and MitoFates, run with
1090 threshold value 0.35 (Fukasawa, Tsuji et al. 2015).
1091
1092 The pooled set of sequences were aligned first with MAFFT v 7.0 under the --auto
1093 setting, followed by the in-built alignment programme in GeneIOUS v 10.0.9, under
1094 default settings (Kearse, Moir et al. 2012, Katoh, Rozewicki et al. 2017). Incomplete
1095 and poorly aligned sequences, alongside taxonomically uninformative N- and C-
1096 terminal regions were removed from the alignment manually, followed by trimal with
1097 setting –gt 0.5 (Capella-Gutiérrez, Silla-Martínez et al. 2009). Phylogenetic analyses
1098 were performed with MrBayes v 3.2 and rAxML v 8, integrated into the CIPRES
1099 webserver (Stamatakis 2014, Miller, Schwartz et al. 2015). MrBayes trees were run
1100 for 10,000,000 generations with the GTR, Jones and WAG substitution matrices, 4
1101 starting chains and sumt and sump burnin fractions set to -0.5; all cold chains were
1102 confirmed to have reached a pvalue plateau below 0.1 prior to the start of the
1103 consensus building. rAxML trees were run with GTR, JTT and WAG substitution
1104 matrices, 350-400 ML generations, and automatic bootstopping. Phylogenies were
1105 either rooted between bacterial and eukaryotic sequences (Enolase); or on the mid-
1106 point (PGAM1, PGAM2) due to the absence of a single monophyletic bacterial
1107 outgroup. A summary of these analyses is provided in **Supplemental Dataset S1**.
1108
1109 Analysis of previously published *Phaeodactylum* data
1110
1111 First, the mean relative abundance of peptides corresponding to Enolase and PGAM
1112 sequences was retrieved from published mass spectrometry data of *Phaeodactylum*
1113 plastid-enriched fractions and total cell pellets, following (Huang, Pan et al. 2024).
1114 The two datasets were found to show a positive correlation with one another (r=
1115 0.891, n = 901, $P < 10^{-05}$) considering all proteins recovered in the plastid-associated
1116 fraction with a previously suspected plastid localisation (plastid-encoded, or plastid-

1117 targeted nucleus-encoded proteins inferred using combined ASAFind and HECTAR
1118 predictions). These data are provided in **Supplemental Dataset S2**, sheet 1.
1119
1120 Next, the expression trends of *Phaeodactylum* plastid glycolysis proteins (cpEnolase,
1121 cpPGAM1A, PGAM2) were assessed in combat normalised RNAseq data (Ait-
1122 Mohamed, Novák Vanclová et al. 2020) assembled from three prior studies, relating
1123 to induced nitrate limitation (nitrate reductase knockout), phosphate limitation and
1124 resupply, and iron limitation over a Circadian cycle (Cruz de Carvalho, Sun et al.
1125 2016, Smith, Gillard et al. 2016, McCarthy, Smith et al. 2017). A second set of
1126 comparisons were performed using normalised *Phaeodactylum* microarray data
1127 (summarised in (Ashworth, Turkarslan et al. 2016), particularly relating to changes in
1128 light quality, wavelength and Circadian time point. To enable global analyses of
1129 coregulation to cpEnolase and cpPGAM enzymes, these two datasets were
1130 converted into ranked values (i.e., for Spearman correlation) and merged, following
1131 (Liu, Storti et al. 2022). These data are summarised in **Supplemental Dataset S2**,
1132 sheets 2-4.
1133
1134 *Tara* Oceans Analysis
1135
1136 The complete *Tara* Oceans and *Tara* Oceans Polar Circle libraries of meta-genome
1137 and meta-transcriptome diversity (Carradec, Pelletier et al. 2018, Royo-Llonch,
1138 Sánchez et al. 2020) were searched for orthologues of diatom cpEnolase,
1139 cpPGAM1A and PGAM2 sequences via a phylogenetic reconciliation approach
1140 benchmarked in previous studies (Kazamia, Sutak et al. 2018, Liu, Storti et al. 2022).
1141 This approach uses the combined outputs of hmmer, BLAST best-hit, and single-
1142 gene tree topologies to only retain *Tara* Oceans meta-genes that reconcile as
1143 monophyletic with a defined query set, in these case plastid-targeted diatom isoforms
1144 of each enzyme. Exemplar tree topologies are shown in **Fig. S8.**
1145
1146 First, a HMM (hidden Markov model) was constructed for all diatom plastid-targeted
1147 sequences in the untrimmed alignments for each phylogeny, as detailed above, and
1148 searched into the complete *Tara* Oceans catalog by hmmer (http://hmmer.org) with
1149 evalue 10^{-10} to identify putative meta-gene homologues of each protein. Matching
1150 sequences were extracted, and searched by BLASTp against the complete copy of

1151 the *P. tricornutum* genome (Rastogi, Maheswari et al. 2018). Only sequences that
1152 retrieved a best hit against an Enolase or PGAM sequence (and therefore likely
1153 correspond to homologues of each protein) were retained. Next, the retained
1154 sequences were similarly searched by BLASTp against the complete untrimmed
1155 alignment of cultured Enolase and PGAM sequences. Only sequences that retrieved
1156 a diatom plastid-targeted isoform were retained, allowing the elimination of non-
1157 diatom and homologues of diatom non-plastid sequences. Finally, sequences were
1158 combined with the untrimmed alignment of cultured sequences from each gene and
1159 realigned using the same MAFFT, GeneIOUS and trimal pipeline as defined above.
1160 Curated alignments were screened by rAxML tree with the JTT substitution matrix, as
1161 above. Only *Tara* Oceans sequences that resolved within a monophyletic clade with
1162 diatom plastid-targeted proteins, defined as all sequences that position closer on a
1163 midpoint rooting of the tree to diatom plastid-targeted proteins than to any non-
1164 diatom or non-plastid targeted sequences, were extracted for further analyses.
1165
1166 Relative abundances were calculated for the total occurrence of all phylogenetically
1167 verified diatom plastid-targeted proteins in both meta-transcriptome and meta-
1168 genome data. Relative expression levels of each gene were estimated by reconciling
1169 the calculated meta-transcriptome abundances either to total diatom meta-
1170 transcriptome sequences using the formula $10^{\wedge 6}(\Sigma_{metaT}/ \Sigma_{DiatomT})$, i.e., expressed per
1171 million reconciled diatom reads, or to calculated meta-genome abundances, using
1172 the formula and $\log_{10} (1+ \Sigma_{metaT}) - \log_{10} (1+ \Sigma_{metaG})$, to allow inclusion of zero metaG
1173 values. Pearson and Spearman correlations were calculated between relative
1174 abundances and all quantitative measured environmental variables associated with
1175 *Tara* Oceans samples as stored within the PANGAEA repository (Pesant, Not et al.
1176 2015). All calculations were repeated independently for each depth (surface, or deep
1177 chlorophyll maximum/ DCM) and size fraction (0.8- 2000 µm, 0.8- 5 µm, 3/5- 20 µm,
1178 20- 180 µm, and 180- 2000 µm), with 3 and 5 µm filters viewed as equivalent to allow
1179 reconciliation of Arctic and non-Arctic data, respectively. All *Tara* Oceans meta-gene
1180 assignations, alongside individual and total abundance calculations are provided in
1181 **Supplemental Dataset S3**, sheets 1-10.
1182
1183 *Tara* Oceans MAGs were partitioned into those that contained credible chloroplast-
1184 targeted copies of Enolase and/ or PGAM sequences, using a similar reciprocal

1185 BLAST best-hit, PFAM analysis and *in silico* targeting prediction pipeline as used for
1186 cultured species data (**Supplemental Dataset S3**, sheet 11). MAGs were partitioned
1187 into those containing both identifiable chloroplast-targeted Enolase and PGAM
1188 enzymes; one only; and neither. The mean mapped vertical depth (analogous to
1189 abundance) was calculated for each MAG from 0.8-2000 µm data at DCM and
1190 surface depths, following data from (Delmont, Gaia et al. 2022), and was compared
1191 to absolute station latitude by Pearson correlation and two-tailed *t*-test.
1192
1193 *Nucleic acid isolation*
1194
1195 For DNA isolation, 150 ml early stationary phase *P. tricornutum* culture, grown under
1196 19°C with 12h light: 12h dark cycling, and shaken at 100 rpm as described above,
1197 was centrifuged at 4000 rpm for 10 minutes. The resulting cell pellet was washed in
1198 sterile growth medium three times, and incubated for four hours in 5 ml TEN buffer
1199 (0.1 M NaCl, 0.01 M Tris pH8, 0.001 M EDTA) supplemented with 2% volume:
1200 volume SDS, and 1U μl^{-1} proteinase K (Fisher Scientific). Lysed cell fractions were
1201 used for phenol: chloroform precipitation of cellular DNA, as previously described
1202 (Nash, Barbrook et al. 2007), prior to dissolution in 50 µl nuclease-free water, and
1203 quantification with a nanodrop photospectrometer.
1204
1205 For RNA isolations, 10^5 stationary phase *P. tricornutum* cells, as calculated with cell
1206 densities counted from a Malassez haemocytometer were inoculated in a 250 ml
1207 conical Erlenmeyer containing 80 ml ESAW without antibiotics. Cell cultures were
1208 harvested in mid-exponential phase, at counted densities of between 1 and 2 x 10^6
1209 cells ml^{-1}. 19C CL cultures were typically harvested eight days post-inoculation, 19C
1210 LD cultures nine days post-inoculation, and 8C CL cultures seventeen days post-
1211 inoculation, in agreement with growth curve dynamics. Cells were harvested at the
1212 mid-point of the light-induction phase of the LD growth condition (15:00 CET), per
1213 previous gene expression studies in *P. tricornutum* (Cruz de Carvalho, Sun et al.
1214 2016).
1215
1216 RNA was isolated from 10^8 cells from each culture, pelleted and washed as before,
1217 and snap-frozen in liquid nitrogen. Frozen cell suspensions were re-equilibrated with
1218 1 ml Trizol reagent (Invivogen) and 200 µl chloroform (Honeywell), prior to phenol:

1219 chloroform extraction. An additional separation step was performed in 500 µl pure
1220 chloroform to remove any residual phenol traces from the aqueous phase, and
1221 purified nucleic acids were precipitated overnight in 500 µl isopropanol at -20°C. RNA
1222 was collected by centrifugation at 10,000 rpm for 30 minutes, washed with 900 µl
1223 100% ethanol, and resupended in 50 µl RNAse-free water (Qiagen).
1224
1225 2 µg RNA, as quantified with a nanodrop photospectrometer, was subsequently
1226 treated with 2U RNAse-free DNAse (Promega) for 30 minutes at 37 °C, and the
1227 reaction was stopped with 1 µl 0.5 M EDTA. The digested RNA sample was
1228 reprecipitated in isopropanol for one hour at -20 °C, washed in ethanol, and
1229 resuspended in 20 µl RNAse-free water. Purified RNA sample concentrations were
1230 quantified with a nanodrop spectrometer, and a 3 µl aliquot was migrated on an
1231 RNAse-free 1% agarose gel stained with 0.2 µg ml^{-1} ethidium bromide to confirm
1232 RNA integrity prior to all downstream applications.
1233
1234 *GFP localization*
1235
1236 Full length mRNA sequences of cpEnolase, cpPGAM1A and cpPGAM2 were
1237 amplified from *P. tricornutum* RNA libraries grown under 19 °C, light: dark cycling and
1238 replete nutrient conditions as described above, by reverse transcription with RT
1239 Maxima First Strand synthesis kit (Thermo Fisher) from 200 ng template RNA,
1240 following the manufacturer's instructions; and gene-specific primers as shown in
1241 **Supplemental Dataset S2**, sheet 4. PCRs were performed using Pfu high-fidelity
1242 DNA polymerase, in 50 µl total reaction volume, including 1 µl cDNA template and 2
1243 µl each specific primer, following the manufacturer's protocol. Typical PCR conditions
1244 were: 10 minutes at 95 °C; followed by 35 cycles of 45 seconds at 95 °C, 45 seconds
1245 at 55 °C, and 2 minutes at 72 °C; followed by a terminal elongation phase of 5
1246 minutes at 72 °C. Amplified products were migrated on a 1% agarose gel stained
1247 with ethidium bromide, cut out, and purified using a MinElute PCR purification kit
1248 (Qiagen).
1249
1250 Purified products were cloned into linearised versions of pPhat vectors containing
1251 eGFP and a zeocin resistance gene (SHBLE). These products were amplified using
1252 an analogous PCR protocol as above, with 1 ng purified plasmid DNA, and outward-

1253 directed PCR primers extending from the start of the fluorescence protein gene
1254 sequence to the end of the FcpA promoter region (**Supplemental Dataset S2**, sheet
1255 4); cut, purified, and treated with 1U FastDigest DpnI (Thermo Fisher) to remove any
1256 residual plasmid DNA. The gene-specific primers for each cpEnolase and cpPGAM
1257 construct were modified with 15 5' nucleotides complementary to the terminal regions
1258 of the FcpA and GFP sequences, allowing cloning of complete vector sequences
1259 using a HiFi DNA assembly kit (NEB), following the manufacturer's instructions.
1260 Assembled vectors were transformed into chemically competent Top10 *E. coli*, and
1261 positive clones (as identified by Sanger sequencing of positive colony PCR products)
1262 were used to generate purified plasmid DNA with a Plasmid Midi Kit (Qiagen).
1263
1264 Subcellular localization constructs were transformed into wild type *P. tricornutum*
1265 Pt186 by biolistic transformation, as previously described (Falciatore, Casotti et al.
1266 1999). 5 x 10^7 mid-exponential phase cells were plated on a ½ ESAW- 1% agarose
1267 plate, and left to recover for two days, prior to bombardment with 10 mg 1 µm
1268 tungsten beads treated with 5 µg purified plasmid DNA in a Helios gene gun
1269 (BioRad) at 1,550 PSI. Cells were left to recover for two days, prior to replating on ½
1270 ESAW- 1% agarose plates supplemented with 100 µg ml^{-1} ampicillin, 100 µg ml^{-1}
1271 streptomycin, 30 µg ml^{-1} chloramphenicol and 100 µg ml^{-1} zeocin. Plates post-
1272 bombardment and for the first two days post-selection were maintained in a low light
1273 environment (10 µE m^{-2} s^{-1}) prior to return to standard growth conditions.
1274
1275 Positive transformant colonies, as verified by Western Blot with a mouse anti-GFP
1276 antibody (Thermo Fisher), were visualised using a SP8 inverted spinning disc
1277 confocal microscopy (Leica) under 400 x magnification, with excitation wavelength
1278 485 nm and emission wavelength filters 500-550 nm. GFP-negative colonies were
1279 used to confirm detection specificity, and empty-vector GFP (with cytoplasmic
1280 localizations) were used as fluorescence positive controls. A minimum of 12 GFP
1281 expressing clones were visualised for each construct with consistent localization.
1282
1283 *CRISPR mutagenesis*
1284
1285 CRISPR target sequences for cpEnolase and cpPGAM1A genes were identified
1286 using PhytoCRISP-Ex (Rastogi, Murik et al. 2016), privileging positions in the N-

1287 terminal region of the conserved domain to minimize the probability of enzyme
1288 functionality in knockout lines, and uniqueness across the entire *P. tricornutum*
1289 genome within the final 11 bp of the target sequence to minimize off-target effects.
1290 Primers were designed for each target sequence, and introduced into a pu6:SG1
1291 CRISPR target sequence plasmid by PCR, as previously described (Nymark,
1292 Sharma et al. 2016). 2 µg insertion-positive pu6:SG1 plasmids, as confirmed by
1293 Sanger sequencing were co-introduced into wild type *P. tricornutum* Pt186 cells by
1294 bombardment along with 2 µg HA-tagged Cas9 and pPhat vectors, as described
1295 above. Mutant colonies were genotyped using a DNA lysis buffer containing 0.14 M
1296 NaCl, 5 mM KCl, 10 mM Tris-HCl pH 7.5, 1% v/v NP40 to generate crude DNA
1297 extracts, followed by PCR amplification across the CRISPR target sequences with
1298 DreamTaq PCR reagent (Promega) and Sanger sequencing (Eurofins genomics).
1299 Mixed mutant: wild-type colonies were segregated via repeated dilution on ESAW:
1300 zeocin plates until only homozygous mutant genotypes were detected (Nymark,
1301 Sharma et al. 2016, McCarthy, Smith et al. 2017). Empty vector control lines were
1302 generated using the same protocol, except with only HA-Cas9 and pPhat plasmids,
1303 cotransformed without a CRISPR target sequence.
1304
1305 Tabulated cleaned knockout mutants, their associated genotypes and the expression
1306 levels of mutated gene copies are shown in **Supplemental Dataset S4**, sheets 1-2.
1307 Mutant colony genotypes were periodically confirmed (approx. once per month) by
1308 PCR and Sanger sequencing throughout the duration of all subsequent experiments,
1309 and the CRISPR-induced gene modifications were found to remain stable. *P.*
1310 *tricornutum* Enolase proteins were determined by Western blot to be crossreactive to
1311 an anti-*Arabidopsis thaliana* Enolase-2 antibody (Agrisera), and thus knockout line
1312 protein expression was confirmed by qRT-PCR, as described below.
1313
1314 *Complementation of knockout lines*
1315
1316 Knockout lines were complemented with pPhat:GFP vectors carrying overexpressing
1317 copies (under an FcpA promoter) of cpEnolase and cpPGAM1A synthetic constructs,
1318 with all CRISPR target sequences replaced with silent mutations (Eurofins). Genes
1319 were fused to C-terminal GFP, allowing the verification of protein expression and
1320 localization. Vectors were identical to those previously used for localization, but with

1321 a blasticidin S-deaminase gene in lieu of SHBLE (Buck, Río Bártulos et al. 2018)
1322 introduced by NEB Hi-Fi kit as before. Complementation constructs were transformed
1323 via bombardment, and cotransformed colonies were selected on ½ ESAW- 1%
1324 agarose plates supplemented with 100 µg ml^{-1} ampicillin, 100 µg ml^{-1} streptomycin,
1325 30 µg ml^{-1} chloramphenicol, 100 µg ml^{-1} zeocin, 4 µg ml^{-1} blasticidin.
1326
1327 For each complementation, three cpEnolase and cpPGAM1A knockout lines
1328 (including at least one for each CRISPR target sequence) were complemented both
1329 with the conjugate construct, and an empty blasticidin resistance vector as a placebo;
1330 and two empty vector lines were further complemented with both cpEnolase and
1331 cpPGAM1A overexpressor constructs, plus an empty blasticidin resistance vector, to
1332 exclude possible effects from ectopic overexpression of each gene on cell
1333 physiology. A total of 47 colonies, with a minimum of 6 colonies for each knockout:
1334 complementation combination, including lines complemented from at least two
1335 distinct primary knockout mutant genotypes, were selected for subsequent study
1336 (**Supplemental Dataset S4**, sheet 7). The retention of the primary knockout mutant
1337 genotype in each complemented line was verified by colony PCR and sequencing as
1338 above, and the overexpression and correct localization of the complementing protein
1339 sequence (i.e., to the chloroplast for cpEnolase:GFP and cpPGAM1:GFP, or the
1340 cytoplasm for ectopic GFP) was verified by western blot with an anti-GFP antibody
1341 (Thermo Fisher) (Erdene-Ochir, Shin et al. 2019) and confocal microscopy.
1342
1343 *Growth rate measurements*
1344
1345 A starting density of 10^4 ml^{-1} stationary phase *P. tricornutum* cells of a given culture
1346 line, as verified with a Malassez haemocytometer, were inoculated into a 15 ml
1347 volume antibiotic-free ESAW within a sterile, ventilated cap plastic culture flask
1348 (Celltreat) and grown under LD, CL, or 8C culture conditions as described. Cell
1349 densities were recorded: every day from one day post-inoculation (CL); every day
1350 from two days post-inoculation (LD); or every two days from five days post-
1351 inoculation (8C) at the mid-point of the LD light induction phase using a counting
1352 CyFlow Cube 8 cytometer (ParTec).
1353

1354 Typically, 15 µl cell culture, passed at 0.5 µl s^{-1}, were used for each measurement,
1355 with three technical replicates performed for each culture of which the first (enriched
1356 in non-cellular particles) was excluded from downstream calculations. Cytometer
1357 particle counts were correlated to actual cell densities using a calibration curve
1358 realised from haemocytometer counted densities of wild-type cell culture, and
1359 cultures with observed densities > 2 x 10^6 cells ml^{-1} were diluted ten-fold in blank
1360 growth media to avoid saturation of the cytometer.
1361
1362 Cell densities were measured until cell lines were confirmed to have exited log phase
1363 (i.e., reached a stationary phase plateau). Primary knockout mutant growth curves
1364 were repeated a minimum of six times (three biological replicates per-inoculation,
1365 with two independent repetitions) for each mutant line. Growth curves were tested for
1366 seven cpEnolase knockout, five cpPGAM1A knockout and four empty vector control
1367 lines, providing a minimum of 24 measurements (i.e., four distinct mutant lines) per
1368 each genotype studied (cpEnolase knockout, cpPGAM1A knockout and empty vector
1369 control lines).
1370
1371 To avoid artifacts based on the proximity of the seed cell culture to exponential phase
1372 at the time of inoculation (which may impact on lag phase length) or the relative
1373 diameter of each cell in culture (which may impact on carrying capacity), cell growth
1374 rates were measured exclusively from the log-phase relative division rate. This was
1375 calculated via considering $\Delta\log_2$ (cell density) / $\Delta\log_2$ (time) for a time-period
1376 corresponding to 5 x 10^4 to 4 x 10^6 cells/ ml, covering in most cases six successive
1377 measurements of each individual growth curve. To confirm that the cells were
1378 measured in exponential phase and were neither influenced by particle
1379 contamination of the cytometer or cell exhaustion of the growth medium, the linear
1380 correlation was calculated between the log value, with most calculated correlations
1381 (129/ 132) showing linearity (r> 0.95). Three exemplar growth curve outputs are
1382 provided in **Supplemental Dataset S4**, sheets 3-5; and an overview of relative
1383 growth rates expressed as a function of mean empty vector control growth rates are
1384 provided in **Supplemental Dataset S4**, sheet 6.
1385
1386 Complementation growth curves were repeated with at least two independent
1387 repetitions for each cell line, with five timepoints taken to project growth rates, and

1388 therefore a minimum of sixty independent measurements for each mutant:
1389 complementation genotype under each growth condition, with the average of the two
1390 fastest growth rates of each culture calculated as estimates for the growth rate. A
1391 heatmap of all estimated complementation line growth rates is provided in
1392 **Supplemental Dataset S4**, sheet 7.
1393
1394 *Photophysiology*
1395
1396 Cultures for photophysiological analysis were grown in 10ml ventilated plastic flasks,
1397 without shaking, under 19C CL and 19C LD as described above. Cultures were
1398 grown from a starting inoculum of 10^5 cells ml^{-1} as measured with a Malassez
1399 haemocytometer. Cell cultures that had reached a measured density of 10^6 cells ml^{-1}
1400 were then refreshed into fresh media at the initial starting concentration of 10^5 cells
1401 ml^{-1} to allow a prolonged adaptation to each photophysiological condition under a
1402 continuous exponential phase. Cells from refreshed culture lines were harvested in
1403 exponential phase (between 1 and 3×10^6 cells ml^{-1}, and good physiology was
1404 verified by Fv/Fm measurements > 0.6 across all measured lines (**Supplemental**
1405 **Dataset S4**, sheet 8).
1406
1407 Steady-state light curves (SSLC) were conducted with a fluorescence CCD camera
1408 recorder (SpeedZen, jBeamBio, France) in a selected set of control lines (*n*=2),
1409 cpPGAM (*n*=3) and cpEnolase knockouts (*n*=6), as well in complemented cpEnolase
1410 (*n*=2) and cpPGAM1A (*n*=3) knockout lines in which we observed a suppression of
1411 the knockout growth defect compared to complemented control lines. Measurements
1412 were repeated a minimum of two and in most cases four times per line and treatment
1413 condition, with a minimum of six unique measurements performed for each genotype
1414 and treatment. Curves were measured on cell cultures concentrated to between 2
1415 and 5×10^7 cells ml^{-1}. Samples were exposed to an initial 5 min illumination of 35
1416 µmol photons m^{-2} s^{-1} green actinic light (532 nm), followed by a 6 steps of 3 min each
1417 of increasing intensity to 750 µmol photons m^{-2} s^{-1}.
1418
1419 Minimum (F_0) and maximum (F_M) fluorescence were measured in dark-adapted (at
1420 least 1 min) samples, before and at the end of a 250 ms saturating (multiple turnover)
1421 pulse of light (532 nm, 5000 µmol photons m^{-2} s^{-1}) and the maximum quantum yield

of PSII in the dark was calculated as F_V/F_M = (F_M -F_0)/F_M. Every minute of light exposure, steady-state fluorescence (F_S) and maximum fluorescence under Light (F_M') were measured. PSII quantum yield (φPSII) and nonphotochemical quenching (NPQ) were calculated on the last time point of each light step as φPSII = (F_M'-F_s)/F_M' and NPQ = F_M/F_M'-1, and rETR at PSII as rETR = φPSII.*E*.

The whole rETR vs *E* curve was fitted as rETR = $rETR_M$.(1-exp(-α.*E*/$rETR_M$)) where $rETR_M$ is the maximum rETR and α is the light-limited slope of rETR vs E (Jassby and Platt 1976). Only rETR values from 0 to 450 µmol photons m^{-2} were used for the fit because values from 600 and 750 µmol photons m^{-2} were too noisy. The light saturation parameter E_K was calculated as $rETR_M$/α and the fitted values of the parameters were used to estimate φPSII under the growth light intensity of 50 µmol photons m^{-2} s^{-1} as $φPSII_{50µE}$= ($rETR_M$.(1-exp(-α.50/$rETR_M$)))/ 50. The NPQ vs E curve was fitted as NPQ = NPQ_M× E^n/ ($E_{50}NPQ^n$+E^n), where NPQ_M is the maximal NPQ, E_{50}NPQ is the half- saturation intensity for NPQ and *n* is the sigmoidicity coefficient (Serôdio and Lavaud 2011).

The PSII functional absorption cross-section, σPSII, was calculated from the fluorescence induction upon a single turnover flash of blue light (100 µs, 455 nm, 60 nm bandwidth) on non-concentrated cell culture. The induction curve was measured on 20 min dark-acclimated samples before centrifugation (average of 2-4 independent replicates) with a Fluorescence Induction and Relaxation (miniFIRe) fluorometer (Gorbunov, Shirsin et al. 2020), which also measures single turnover F_V/F_M and PSII connectivity. Parameters measured with the miniFIRe fluorometer (as defined below) were also quantified for cultures grown under 8C CL, as the measurements were sufficiently rapid to allow the culture to be maintained at growth temperatures (Gorbunov, Shirsin et al. 2020). Measured photophysiological values are tabulated in **Supplemental Dataset S4**, sheet 8. Violin plots of photophysiological parameters were generated with BoxPlotR (Spitzer, Wildenhain et al. 2014).

Gene expression analysis

1455 Libraries were prepared from 200 ng DNAse-treated RNA for each mutant line and
1456 treatment condition, with at least three replicates per sample. Sequencing was
1457 performed by Fasteris (Plan-les-Ouates, Switzerland). After initial quality control
1458 checks, stranded Illumina mRNA libraries were prepared with a Novaseq V1.5 kit and
1459 sequenced with an SP-flow cell with 2x 100 bp over 200 cycles, yielding circa 130-
1460 160 Gb sequence data per sample with ≥85% of bases higher than Q30.
1461
1462 FastQ files were mapped using Nextflow's RNA sequencing assembly pipeline
1463 https://nf-co.re/rnaseq/usage, to gff3 annotations of the *P. tricornutum* version 3
1464 genome (Rastogi, Maheswari et al. 2018, Lataretu and Hölzer 2020). Total mapped
1465 read counts were then compared between all biological and technical replicates for (i)
1466 each mutant line sequenced, (ii) each genotype (cpEnolase knockout, cpPGAM1A
1467 knockout, control), and (iii) each treatment condition performed (LD, CL, 8C) by
1468 principal component analysis (PCA) using the R package factoextra, with highly
1469 variant libraries removed (Kassambara and Mundt 2017). The final dataset included
1470 63 RNAseq libraries, including five cpEnolase and five cpPGAM1A knockout lines
1471 and four empty vector controls, and a minimum of four RNA libraries prepared from
1472 at least two genetically distinct mutant constructs for each genotype (cpEnolase,
1473 cpPGAM1A and control) considered (**Supplemental Dataset S5**, sheets 1-2).,
1474 Differentially expressed genes (DEGs) were then calculated between each genotype
1475 for each treatment condition using DESeq2 with cutoff fold-change 2 and P-value
1476 0.05 (Liu, Wang et al. 2021) (**Supplemental Dataset S5**, sheets 2-3).
1477
1478 The mean transcript abundances of DEGs in knockout compared to control lines
1479 were first assessed in RNAseq data of N and P-limited *P. tricornutum* cell lines under
1480 two and nine time-points respectively (**Supplemental Dataset S5**, sheet 4) (Cruz de
1481 Carvalho, Sun et al. 2016, McCarthy, Smith et al. 2017). No significant differences
1482 were found between DEGs and other genes in the *P. tricornutum* genome (one-way
1483 ANOVA, $P > 0.05$; **Supplemental Dataset S5**, sheet 5), confirming that the RNAseq
1484 samples were not generated from N- or P-limited cultures. Next, functional
1485 enrichments in DEGs from previously tabulated values for the entire *P. tricornutum*
1486 genome (**Supplemental Dataset S5**, sheets 6-10) (Rastogi, Maheswari et al. 2018,
1487 Ait-Mohamed, Novák Vanclová et al. 2020). Functional enrichments were tested by
1488 two-tailed chi-square ($P < 0.05$) of a differentially expressed gene occurring in either

1489 one (cpEnolase v control; cpPGAM1A v control) knockout-versus-control line tests, or
1490 in both tests realised under each physiological condition. Finally, the distribution of
1491 DEGs across *P. tricornutum* core plastid and mitochondrial metabolism pathways
1492 were mapped onto a previously defined proteomic model of each organelle (Ait-
1493 Mohamed, Novák Vanclová et al. 2020); with the strongest DEG enrichment taken in
1494 the case of enzymes with multiple homologues (**Supplemental Dataset S5**, sheet
1495 11).
1496
1497 Quantitative RT-PCR (qRT-PCR) validations were performed using cDNA
1498 synthesised from 5 ng dNase-treated RNA (per qRT-PCR reaction) and a RT
1499 Maxima First Strand synthesis kit (Thermo Fisher), following the manufacturer's
1500 instruction; using a 384-well Lightcycler (Roche) and Takyon™ No ROX SYBR 2X
1501 MasterMix (Eurogentec), following the manufacturers' protocols. Typical amplification
1502 conditions were: 10 minutes at 95°C, followed by 40 cycles of 30 seconds at 95°C,
1503 30 seconds at 55°C, and 30 seconds at 72°C. Primer pairs for qRT-PCR
1504 amplifications were designed using NCBI Primer-BLAST (Ye, Coulouris et al. 2012),
1505 privileging unique amplification targets within the genomic sequence, an amplicon
1506 size of 100 to 150 base pairs, primer positions at different regions of the gene
1507 studied, and a 3' terminal G or C on each primer. Primer efficiencies were tested by
1508 qPCR with serial dilutions of *P. tricornutum* gDNA, with only primer pairs that yielded
1509 a Cp increment of between 0.9 and 1.1 per half dilution of DNA retained for qRT-PCR
1510 analysis. qRT-PCRs were at least three times for each amplicon: sample pair. RT-
1511 equivalents were performed to subtract residual genomic DNA from each Cp value
1512 obtained, and two housekeeping genes (Ribosomal protein S1, RPS; and TATA
1513 binding protein, TBP) previously shown to have conditionally invariant expression
1514 patterns in *P. tricornutum* were used as quantification references (Sachse, Sturm et
1515 al. 2013). Tabulated qRT-PCR outputs are shown in **Supplemental Dataset S5**,
1516 sheet 13; and sample information and reaction conditions per MIQE guidelines
1517 (Bustin, Benes et al. 2009) are tabulated in **Supplemental Dataset S5**, sheet 14.
1518
1519 *Metabolite analysis*
1520
1521 Cell pellets were taken from exponential-phase *P. tricornutum* culture (counted
1522 density 1-2 x 10^6 cells ml^{-1}, 1.5 x 10^8 cells per sample) for metabolite and lipid

1523 analysis. Cell pellets were collected without washing to minimise impacts on
1524 metabolite turnover, then transferred to a pre-weighed, double-pierced and double-
1525 autoclaved 1.5 ml Eppendorf tube for lyophilization. Cell pellet masses were
1526 recorded, and samples were immediately snap-frozen in liquid nitrogen and stored at
1527 -80 °C for subsequent analysis.
1528
1529 Metabolite profiling was carried out by gas chromatography–mass spectrometry
1530 (ChromaTOF software, Pegasus driver 1.61; LECO) as described previously (Lisec,
1531 Schauer et al. 2006). The chromatograms and mass spectra were evaluated using
1532 TagFinder software (Luedemann, von Malotky et al. 2012). Metabolite identification
1533 was manually checked by the mass spectral and retention index collection of the
1534 Golm Metabolome Database (Kopka, Schauer et al. 2005). Peak heights of the mass
1535 fragments were normalized successively on the basis of the fresh weight of the
1536 sample, the added amount of an internal standard (ribitol) and values obtained for
1537 loading column controls obtained from the same experiment.
1538
1539 *Glycerolipid analysis*
1540
1541 Glycerolipids were extracted by suspending cell pellets in 4 mL of boiling ethanol for
1542 5 minutes to prevent lipid degradation. Lipids were extracted by addition of 2 mL
1543 methanol and 8 mL chloroform at room temperature (Folch, Lees et al. 1957). The
1544 mixture was then saturated with argon and stirred for 1 hour at room temperature.
1545 After filtration through glass wool, cell remains were rinsed with 3 mL
1546 chloroform/methanol 2:1, v/v and 5 mL of NaCl 1% was added to the filtrate to initiate
1547 biphase formation. The chloroform phase was dried under argon and stored at -20
1548 °C. The lipid extract was resuspended in pure chloroform when needed.
1549
1550 Total glycerolipids were quantified from their fatty acids: in an aliquot fraction, 5 µg of
1551 15:0 was added and the fatty acids present were converted to methyl esters (FAME)
1552 by a 1-hour incubation in 3 mL 2.5% H_2SO_4 in pure methanol at 100 °C (Jouhet,
1553 Maréchal et al. 2003). The reaction was stopped by addition of 3 mL water and 3 mL
1554 hexane. The hexane phase was analyzed by a gas chromatography-flame ionization
1555 detector (GC-FID) (Perkin Elmer) on a BPX70 (SGE) column. FAMEs were identified

1556 by comparison of their retention times with those of standards (Sigma) and quantified
1557 using 15:0 for calibration.
1558
1559 Glycerolipids were further analyzed by high pressure liquid chromatography-tandem
1560 mass spectrometry (HPLC-MS/MS), based on a previously described procedure
1561 (Rainteau, Humbert et al. 2012). The lipid extracts corresponding to 25 nmol of total
1562 fatty acids were dissolved in 100 µL of chloroform/methanol [2/1, (v/v)] containing
1563 125 pmol of each internal standard. Internal standards used were
1564 phosphatidylethanolamine (PE) 18:0-18:0 and diacylglycerol (DAG) 18:0-22:6 from
1565 Avanti Polar Lipid, and sulfoquinovosyldiacylglycerol (SQDG) 16:0-18:0 extracted
1566 from spinach thylakoids (Demé, Cataye et al. 2014) and hydrogenated (Buseman,
1567 Tamura et al. 2006). Lipid classes were separated using an Agilent 1200 HPLC
1568 system using a 150 mm × 3 mm (length × internal diameter) 5 µm diol column
1569 (Macherey-Nagel), at 40 °C. The mobile phases consisted of hexane/ isopropanol/
1570 water/ 1 M ammonium acetate, pH 5.3 [625/350/24/1, (v/v/v/v)] (A) and isopropanol/
1571 water/ 1 M ammonium acetate, pH 5.3 [850/149/1, (v/v/v)] (B). The injection volume
1572 was 20 µL. After 5 min, the percentage of B was increased linearly from 0% to 100%
1573 in 30 min and kept at 100% for 15 min. This elution sequence was followed by a
1574 return to 100% A in 5 min and an equilibration for 20 min with 100% A before the
1575 next injection, leading to a total runtime of 70 min. The flow rate of the mobile phase
1576 was 200 µL min^{-1}. The distinct glycerophospholipid classes were eluted successively
1577 as a function of the polar head group. Mass spectrometric analysis was performed on
1578 a 6460 triple quadrupole mass spectrometer (Agilent) equipped with a Jet stream
1579 electrospray ion source under following settings: drying gas heater at 260 °C, drying
1580 gas flow at 13 $L \cdot min^{-1}$, sheath gas heater at 300 °C, sheath gas flow at 11 $L \cdot min^{-1}$,
1581 nebulizer pressure at 25 psi, capillary voltage at ± 5000 V and nozzle voltage at ±
1582 1,000 V. Nitrogen was used as the collision gas. The quadrupoles Q1 and Q3 were
1583 operated at widest and unit resolution, respectively.
1584
1585 Phosphatidylcholine (PC) and diacylglyceryl hydroxymethyltrimethyl-*β*-alanine
1586 (DGTA) analyses were carried out in positive ion modes by scanning for precursors
1587 of m/z 184 and 236 respectively at a collision energy (CE) of 34 and 52 eV. SQDG
1588 analysis was carried out in negative ion mode by scanning for precursors of m/z -225
1589 at a CE of -56eV. PE, phosphatidylinositol (PI), phosphatidylglycerol (PG),

1590 monogalactosyldiacylglycerol (MGDG) and digalactosyldiacylglycerol (DGDG)
1591 measurements were performed in positive ion modes by scanning for neutral losses
1592 of 141 Da, 277 Da, 189 Da, 179 Da and 341 Da at cEs of 20 eV, 12 eV, 16 eV, 8 eV
1593 and 8 eV, respectively. DAG and triacylglycerol (TAG) species were identified and
1594 quantified by multiple reaction monitoring (MRM) as singly charged ions $[M+NH4]^+$ at
1595 a CE of 16 and 22 eV respectively. Quantification was done for each lipid species by
1596 MRM with 50 ms dwell time with the various transitions previously recorded (Abida,
1597 Dolch et al. 2015). Mass spectra were processed using the MassHunter Workstation
1598 software (Agilent) for lipid identification and quantification. Lipid amounts (pmol) were
1599 corrected for response differences between internal standards and endogenous lipids
1600 as described previously (Jouhet, Lupette et al. 2017).
1601
1602 Normalised metabolite and lipid abundances were screened by PCA, as per the
1603 RNAseq analysis above, and outliers and biologically non-representative samples
1604 were removed. The final datasets consist of 139 libraries (metabolite GC-MS), 55
1605 libraries (lipid GC-MS) and 49 libraries (lipid LC-MS), with a minimum of three
1606 libraries prepared from at least two genetically distinct mutant constructs for each
1607 genotype considered (**Supplemental Dataset S6**, sheet 1). Violin plots of
1608 differentially accumulated lipids were generated with BoxPlotR (Spitzer, Wildenhain
1609 et al. 2014).
1610
1611 *Expressed enzyme reaction kinetics*
1612
1613 Measurements of cpEnolase and cpPGAM1A reaction rates were performed
1614 following a previously defined protocol (Zhang, Sampathkumar et al. 2020) (**Fig.
1615 S20**). First, codon-optimised constructs for *E. coli* expression were synthesized
1616 (Eurofins) using full-length cpEnolase and cpPGAM1A mRNA sequences as
1617 template. Constructs were cloned into a Gateway pDest-CTD-His vector via a
1618 pDONR intermediate and BP /LR clonase (all reagents Thermo Fisher) following the
1619 manufacturer's instructions (Hartley, Temple et al. 2000). To enable optimal
1620 expression in *E. coli*, multiple N-terminal length variants were synthesized from each
1621 gene, with those corresponding to the full gene length minus the predicted N-terminal
1622 signal peptide domain as inferred with SignalP (Almagro Armenteros, Tsirigos et al.

1623 2019). Complete constructs and primers tested are provided in **Supplemental**
1624 **Dataset S6**, sheet 7.
1625
1626 cpEnolase and cpPGAM1A –CTDHis vectors were cloned into Rosetta (DE3) strain
1627 *E. coli* (Novagen) and coselected on ampicillin (100 µg /ml) and chloramphenicol (34
1628 µg /ml). Proteins were induced in overnight cultures at 28°C, purified on a His-Trap
1629 column (GE Healthcare) following the manufacturers' instructions, and eluted in a
1630 buffer consisting of 125 mM NaCl, 250 mM Imidiazol (Sigma) and protease inhibitors.
1631 Eluted proteins were desalted using a Q10/ PD10 column (GE Healthcare) and
1632 quantified using a Bradford. Protein integrity and quantity were assessed routinely
1633 throughout the purification using SDS-PAGE.
1634
1635 Reaction rates were measured on purified 100 µg cpPGAM1A and 100 µg
1636 cpEnolase, as quantified with a nanodrop spectrometer. Rates were measured
1637 separately for glycolytic and gluconeogenic activity. Briefly, to measure glycolytic
1638 reaction rates, both enzymes were combined with 10 units pyruvate kinase and 10
1639 units lactate dehydrogenase (both Sigma-Aldrich) at 25°C, alongside varying
1640 concentrations 9 mM D(-)3-Phosphoglyceric Acid, 25 mM Adenosine ''-Diphosphate,
1641 and 25 mM reduced ß-Nicotinamide Adenine Dinucleotide (NADH). Enzymatic
1642 activity was measured by considering 340 nm colorimetry as a proxy for NADH
1643 consumption following a previously defined protocol (Sigma protocols EC 5.4.2.1)
1644 (Sutherland, Posternak et al. 1949). To measure gluconeogenic reaction rates, a
1645 similar reaction was performed with both enzymes combined with 10 units
1646 phosphoglycerate kinase and 10 units glyceraldehyde-3-phosphate dehydrogenase
1647 (both Sigma-Aldrich), alongside 9 mM phospho-enol-pyruvate, 25 mM Adenosine 5'-
1648 Diphosphate, and 25 mM reduced ß-Nicotinamide Adenine Dinucleotide (NADH).
1649 Enzymatic activity was similarly measured by 340 nm colorimetry. A schematic of the
1650 measured reactions is provided in **Fig. S20**. Complete measured reaction rates over
1651 all technical replicates are provided in **Supplemental Dataset S6**, sheet 8.
1652
1653 **Accession Numbers**
1654
1655 RNAseq data associated with this project is deposited with NCBI BioProject with
1656 project number PRJNA788211.

1657

1658 **Materials Distribution Statement**

1659

1660 The author(s) responsible for distribution of materials integral to the findings
1661 presented in this article in accordance with the policy described in the Instructions for
1662 Authors (https://academic.oup.com/plcell/pages/General-Instructions) are: Richard G.
1663 Dorrell (richard.dorrell.algae@gmail.com) and Chris Bowler
1664 (cbowler@bio.ens.psl.eu).

1665

1666 **List of Supporting Files**

1667

1668 **Supplemental Dataset S1. Phylogenetic diversity of Enolase and PGAM**
1669 **sequences from across the tree of life.**

1670

1671 **Supplemental Dataset S2. Transcriptional and localization patterns of cpPGAM**
1672 **and cpEnolase genes in *Phaeodactylum tricornutum*.**

1673

1674 **Supplemental Dataset S3. *Tara* Oceans analysis of diatom plastid glycolysis.**

1675

1676 **Supplemental Dataset S4. Genotyping, growth dynamics and photophysiology**
1677 **in *P. tricornutum* plastid glycolysis mutant lines.**

1678

1679 **Supplemental Dataset S5. Differentially and conditionally expressed genes in**
1680 ***P. tricornutum* plastid glycolysis mutants.**

1681

1682 **Supplemental Dataset S6. Lipid and metabolite profiles of *P. tricornutum***
1683 **plastid glycolysis mutant lines revealed by GC- and LC-mass spectrometry,**
1684 **and measured reaction kinetics of expressed enzymes.**

1685

1686 All remaining supporting data not provided directly in paper supporting tables are
1687 provided in the linked Open Science Foundation Supporting database
1688 https://osf.io/89vm3/ (Dorrell, Novak Vanclova et al. 2022). Project contents are
1689 ordered hierarchically by theme, with an overview of all contents provided on the site

wiki page. A dedicated README file in each project folder explains the data presented and provides detailed methodology for each analysis.

Author Contributions

RGD designed the research, with critical input from YZ, YZ, DC, BB, ARF, JJ, EM and CB. RGD, YZ, NG, TN, DC, MP, and VG performed the research. RGD, YZ, YL, DC and MP analysed the data. SA provided new analytical tools for cell growth measurements, and JJPK and NZ provided new computational tools for meta-genomic and RNA-seq analysis. RGD wrote the paper, with critical input from YL, TN, MP, SA, BB, JJPK, JJ, EM and CB. All coauthors read and approved the manuscript draft prior to final submission.

Acknowledgments

RGD acknowledges a CNRS Momentum Fellowship, awarded from 2019-2021, an ANR JCJC Grant (« PanArctica » ANR-21-CE02-0014-01) awarded 2021-2022 and an ERC Starting Grant Grant (ChloroMosaic, 101039760), awarded from 2023-2027. CB acknowledges support from FFEM - French Facility for Global Environment, French Government ‘Investissements d’Avenir’ programs OCEANOMICS (ANR-11-BTBR-0008), FRANCE GENOMIQUE (ANR-10-INBS-09-08), MEMO LIFE (ANR-10-LABX-54), and PSL Research University (ANR-11-IDEX-0001-02), the European Research Council (ERC) under the European Union’s Horizon 2020 research and innovation program (Diatomic; grant agreement No. 835067), and from the ANR ‘BrownCut’ project (ANR-19-CE20-0020). CB, EM and JJ were supported by ANR ‘DIM’ (ANR-21-CE02-0021) and PEPR AlgAdvance (22-PEBB-0002). The lipid analyses were performed at the LIPANG (Lipid analysis in Grenoble) platform hosted by the LPCV (UMR 5168 CNRS-CEA-INRAE-UGA) and supported by the Rhône-Alpes Region, the European Regional Development Fund (ERDF), Institut Carnot 3BCAR and Labex GRAL (10-LABX-0049), financed within the University Grenoble Alpes graduate school (Ecoles Universitaires de Recherche) CBH-EUR-GS (ANR-17-EURE-0003). YZ and ARF acknowledge funding from the European Union’s Horizon 2020 research and innovation program, project PlantaSYST (SGA-CSA No. 739582 under FPA No. 66462; and the BG05M2OP001-1.003-001-C01 project,

financed by the European Regional Development Fund through the Bulgarian 'Science and Education for Smart Growth' Operational Programme. D.C and B.B acknowledge the support of the European Research Council (ERC) under the European Union's Horizon 2020 research and innovation program (PhotoPHYTOMIX project, grant agreement No. 715579). The authors acknowledge Giselle McCallum, Elena Kazamia and Xia Gao (IBENS) for assistance with the optimization of cell cytometry protocols; Amandine Baylet (Lycée ENCPB-Pierre Gilles de Gennes), Quentin Caris (Lycée de la Vallée de Chevreuse) and Yonna Lauruol (Ecole Sup'BioTech) for assistance with growth measurements, Frédy Barneche and Clara Richet-Bourbousse (IBENS) for the use of culture facilities; Nathalie Joli (IBENS) for aid with RNAseq library production; Catherine Cantrel and Priscillia Pierre-Elies (IBENS), Pauline Clémente (Lycée ENCPB-Pierre Gilles de Gennes) and Shun-Min Yang (University of South Bohemia) for the preparation of media substrates and aid with biolistic transformations; Ansgar Gruber (University of South Bohemia) for advice concerning the experimental localisation of chloroplast glycolysis proteins; Max Gorbunov (Rutgers University, NJ, USA) for the provision of the miniFIRE fluorometer used for photophysiological assays; and Mattia Storti (CEA Grenoble) for cell outlines used in the production of **Fig. 1A**. This paper is contribution XXX of *Tara* Oceans.

References

Abida, H., L. J. Dolch, C. Meï, V. Villanova, M. Conte, M. A. Block, G. Finazzi, O. Bastien, L. Tirichine, C. Bowler, F. Rébeillé, D. Petroutsos, J. Jouhet and E. Maréchal (2015). Membrane glycerolipid remodeling triggered by nitrogen and phosphorus starvation in Phaeodactylum tricornutum. Plant Physiol **167**(1): 118-136.

Ait-Mohamed, O., A. M. G. Novák Vanclová, N. Joli, Y. Liang, X. Zhao, A. Genovesio, L. Tirichine, C. Bowler and R. G. Dorrell (2020). PhaeoNet: a holistic RNAseq-based portrait of transcriptional coordination in the model diatom *Phaeodactylum tricornutum*. Frontiers Plant Sci **11**: 590949.

Allen, A. E., C. L. Dupont, M. Obornik, A. Horak, A. Nunes-Nesi, J. P. McCrow, H. Zheng, D. A. Johnson, H. Hu, A. R. Fernie and C. Bowler (2011). Evolution and metabolic significance of the urea cycle in photosynthetic diatoms. Nature **473**(7346): 203-+.

Almagro Armenteros, J. J., K. D. Tsirigos, C. K. Sønderby, T. N. Petersen, O. Winther, S. Brunak, G. von Heijne and H. Nielsen (2019). SignalP 5.0 improves signal peptide predictions using deep neural networks. Nat Biotechnol **37**(4): 420-423.

Andriotis, V. M., N. J. Kruger, M. J. Pike and A. M. Smith (2010). Plastidial glycolysis in developing *Arabidopsis* embryos. New Phytol **185**(3): 649-662.

1762 Anoman, A. D., M. Flores-Tornero, S. Rosa-Telléz, J. Muñoz-Bertomeu, J. Segura and R.
1763 Ros (2016). The specific role of plastidial glycolysis in photosynthetic and heterotrophic
1764 cells under scrutiny through the study of glyceraldehyde-3-phosphate dehydrogenase.
1765 Plant Signal Behav **11**(3): e1128614.
1766 Ashworth, J., S. Turkarslan, M. Harris, M. V. Orellana and N. S. Baliga (2016). Pan-
1767 transcriptomic analysis identifies coordinated and orthologous functional modules in
1768 the diatoms *Thalassiosira pseudonana* and *Phaeodactylum tricornutum*. Mar Genomics
1769 **26**: 21-28.
1770 Bai, Y., T. Cao, O. Dautermann, P. Buschbeck, M. B. Cantrell, Y. Chen, C. D. Lein, X. Shi, M. A.
1771 Ware, F. Yang, H. Zhang, L. Zhang, G. Peers, X. Li and M. Lohr (2022). Green diatom
1772 mutants reveal an intricate biosynthetic pathway of fucoxanthin. Proc Natl Acad Sci USA
1773 **119**(38): e2203708119.
1774 Bailleul, B., N. Berne, O. Murik, D. Petroutsos, J. Prihoda, A. Tanaka, V. Villanova, R.
1775 Bligny, S. Flori, D. Falconet, A. Krieger-Liszkay, S. Santabarbara, F. Rappaport, P. Joliot, L.
1776 Tirichine, P. G. Falkowski, P. Cardol, C. Bowler and G. Finazzi (2015). Energetic coupling
1777 between plastids and mitochondria drives CO2 assimilation in diatoms. Nature
1778 **524**(7565): 366-3267.
1779 Behrenfeld, M. J., K. H. Halsey, E. Boss, L. Karp-Boss, A. J. Milligan and G. Peers (2021).
1780 Thoughts on the evolution and ecological niche of diatoms. Ecol Monograph **91**(3):
1781 e01457.
1782 Broddrick, J. T., N. Du, S. R. Smith, Y. Tsuji, D. Jallet, M. A. Ware, G. Peers, Y. Matsuda, C. L.
1783 Dupont, B. G. Mitchell, B. O. Palsson and A. E. Allen (2019). Cross-compartment
1784 metabolic coupling enables flexible photoprotective mechanisms in the diatom
1785 *Phaeodactylum tricornutum*. New Phytol **222**: 1364-1379.
1786 Bromke, M. A. (2013). Amino Acid biosynthesis pathways in diatoms. Metabolites **3**(2):
1787 294-311.
1788 Buck, J. M., C. Río Bártulos, A. Gruber and P. G. Kroth (2018). Blasticidin-S deaminase, a
1789 new selection marker for genetic transformation of the diatom. PeerJ **6**: e5884.
1790 Buck, J. M., J. Sherman, C. R. Bártulos, M. Serif, M. Halder, J. Henkel, A. Falciatore, J.
1791 Lavaud, M. Y. Gorbunov, P. G. Kroth, P. G. Falkowski and B. Lepetit (2019). Lhcx proteins
1792 provide photoprotection via thermal dissipation of absorbed light in the diatom
1793 *Phaeodactylum tricornutum*. Nat Commun **10**(1): 4167.
1794 Buseman, C. M., P. Tamura, A. A. Sparks, E. J. Baughman, S. Maatta, J. Zhao, M. R. Roth, S.
1795 W. Esch, J. Shah, T. D. Williams and R. Welti (2006). Wounding stimulates the
1796 accumulation of glycerolipids containing oxophytodienoic acid and dinor-
1797 oxophytodienoic acid in *Arabidopsis* leaves. Plant Physiol **142**(1): 28-39.
1798 Bustin, S. A., V. Benes, J. A. Garson, J. Hellemans, J. Huggett, M. Kubista, R. Mueller, T.
1799 Nolan, M. W. Pfaffl, G. L. Shipley, J. Vandesompele and C. T. Wittwer (2009). The MIQE
1800 Guidelines: Minimum Information for publication of Quantitative real-time PCR
1801 Experiments. Clin Chem **55**(4): 611-622.
1802 Capella-Gutiérrez, S., J. M. Silla-Martínez and T. Gabaldón (2009). trimAl: a tool for
1803 automated alignment trimming in large-scale phylogenetic analyses. Bioinformatics
1804 **25**(15): 1972-1973.
1805 Carradec, Q., E. Pelletier, C. Da Silva, A. Alberti, Y. Seeleuthner, R. Blanc-Mathieu, G. Lima-
1806 Mendez, F. Rocha, L. Tirichine, K. Labadie, A. Kirilovsky, A. Bertrand, S. Engelen, M. A.
1807 Madoui, R. Méheust, J. Poulain, S. Romac, D. J. Richter, G. Yoshikawa, C. Dimier, S.
1808 Kandels-Lewis, M. Picheral, S. Searson, O. Jaillon, J. M. Aury, E. Karsenti, M. B. Sullivan, S.
1809 Sunagawa, P. Bork, F. Not, P. Hingamp, J. Raes, L. Guidi, H. Ogata, C. de Vargas, D.

1810 Iudicone, C. Bowler, P. Wincker and *Tara* Oceans Coordinators (2018). A global ocean
1811 atlas of eukaryotic genes. Nat Commun **9**(1): 373.
1812 Carrera, D., G. M. George, M. Fischer-Stettler, F. Galbier, S. Eicke, E. Truernit, S. Streb and
1813 S. C. Zeeman (2021). Distinct plastid fructose bisphosphate aldolases function in
1814 photosynthetic and non-photosynthetic metabolism in *Arabidopsis*. J Exp Bot **72**(10):
1815 3739-3755.
1816 Chang, Y. F., J. S. Imam and M. F. Wilkinson (2007). The nonsense-mediated decay RNA
1817 surveillance pathway. Annu Rev Biochem **76**: 51-74.
1818 Cruz de Carvalho, M. H., H. X. Sun, C. Bowler and N. H. Chua (2016). Noncoding and
1819 coding transcriptome responses of a marine diatom to phosphate fluctuations. New
1820 Phytol **210**(2): 497-510.
1821 Delmont, T. O., M. Gaia, D. D. Hinsinger, P. Frémont, C. Vanni, A. Fernandez-Guerra, A. M.
1822 Eren, A. Kourlaiev, L. d'Agata, Q. Clayssen, E. Villar, K. Labadie, C. Cruaud, J. Poulain, C. Da
1823 Silva, M. Wessner, B. Noel, J.-M. Aury, S. Sunagawa, S. G. Acinas, P. Bork, E. Karsenti, C.
1824 Bowler, C. Sardet, L. Stemmann, C. de Vargas, P. Wincker, M. Lescot, M. Babin, G. Gorsky,
1825 N. Grimsley, L. Guidi, P. Hingamp, O. Jaillon, S. Kandels, D. Iudicone, H. Ogata, S. Pesant,
1826 M. B. Sullivan, F. Not, K.-B. Lee, E. Boss, G. Cochrane, M. Follows, N. Poulton, J. Raes, M.
1827 Sieracki, S. Speich and E. Pelletier (2022). Functional repertoire convergence of distantly
1828 related eukaryotic plankton lineages abundant in the sunlit ocean. Cell Genom **2**(5):
1829 100123.
1830 Demé, B., C. Cataye, M. A. Block, E. Maréchal and J. Jouhet (2014). Contribution of
1831 galactoglycerolipids to the 3-dimensional architecture of thylakoids. FASEB J **28**(8):
1832 3373-3383.
1833 Dolch, L. J. and E. Maréchal (2015). Inventory of fatty acid desaturases in the pennate
1834 diatom *Phaeodactylum tricornutum*. Mar Drugs **13**(3): 1317-1339.
1835 Dorrell, R. G., G. Gile, G. McCallum, R. Méheust, E. P. Bapteste, C. M. Klinger, L. Brillet-
1836 Guéguen, K. D. Freeman, D. J. Richter and C. Bowler (2017). Chimeric origins of
1837 ochrophytes and haptophytes revealed through an ancient plastid proteome. Elife **6,**
1838 23717.
1839 Dorrell, R. G., A. M. G. Novák Vanclová, M. Penot, J. J. Pierella Karlusich, C. Bowler, S. Liu,
1840 E. Maréchal, J. Jouhet, B. Bailleul and D. Croteau (2022). Functional physiology of novel
1841 diatom chloroplast proteins. Open Science Foundation. https://osf.io/89vm3/.
1842 Emanuelsson, O., S. Brunak, G. von Heijne and H. Nielsen (2007). Locating proteins in the
1843 cell using TargetP, SignalP and related tools. Nat Protocol **2**(4): 953-971.
1844 Erdene-Ochir, E., B. K. Shin, B. Kwon, C. Jung and C. H. Pan (2019). Identification and
1845 characterisation of the novel endogenous promoter HASP1 and its signal peptide from
1846 *Phaeodactylum tricornutum*. Sci Rep **9**(1): 9941.
1847 Falciatore, A., R. Casotti, C. Leblanc, C. Abrescia and C. Bowler (1999). Transformation of
1848 Nonselectable Reporter Genes in Marine Diatoms. Mar Biotechnol (NY) **1**(3): 239-251.
1849 Folch, J., M. Lees and G. H. S. Stanley (1957). A simple method for the isolation and
1850 purification of total lipids from animal tissues. J Biol Chem **226**(1): 497-509.
1851 Friedlingstein, P., M. W. Jones, M. O'Sullivan, R. M. Andrew, D. C. Bakker, J. Hauck, C. Le
1852 Quéré, G. P. Peters, W. Peters and J. Pongratz (2022). Global carbon budget 2021. Earth
1853 System Science Data **14**(4): 1917-2005.
1854 Fukasawa, Y., J. Tsuji, S. C. Fu, K. Tomii, P. Horton and K. Imai (2015). MitoFates:
1855 improved prediction of mitochondrial targeting sequences and their cleavage sites. Mol
1856 Cell Proteom **14**(4): 1113-1126.

Fukayama, H., C. Masumoto, Y. Taniguchi, A. Baba-Kasai, Y. Katoh, H. Ohkawa and M. Miyao (2015). Characterization and expression analyses of two plastidic enolase genes in rice. Biosci Biotechnol Biochem **79**(3): 402-409.
Fuss, J., O. Liegmann, K. Krause and S. A. Rensing (2013). Green Targeting Predictor and Ambiguous Targeting Predictor 2: the pitfalls of plant protein targeting prediction and of transient protein expression in heterologous systems. New Phytol **200**: 1022-1033.
Gachon, C. M. M., S. Heesch, F. C. Kuepper, U. E. M. Achilles-Day, D. Brennan, C. N. Campbell, A. Clarke, R. G. Dorrell, J. Field, S. Gontarek, C. R. Menendez, R. J. Saxon, A. Veszelovszki, M. D. Guiry, K. Gharbi, M. Blaxter and J. G. Day (2013). The CCAP KnowledgeBase: linking protistan and cyanobacterial biological resources with taxonomic and molecular data. Systemat Biodiv **11**(4): 407-413.
Gilbertson, R., E. Langan and T. Mock (2022). Diatoms and their microbiomes in complex and changing polar oceans. Front Microbiol **13**: 786764.
Gorbunov, M. Y., E. Shirsin, E. Nikonova, V. V. Fadeev and P. G. Falkowski (2020). A multi-spectral fluorescence induction and relaxation (FIRe) technique for physiological and taxonomic analysis of phytoplankton communities. Mar Ecol Prog Series **644**: 1-13.
Grigoriev, I. V., R. D. Hayes, S. Calhoun, B. Kamel, A. Wang, S. Ahrendt, S. Dusheyko, R. Nikitin, S. J. Mondo, A. Salamov, I. Shabalov and A. Kuo (2021). PhycoCosm, a comparative algal genomics resource. Nucleic Acids Res **49**(D1): D1004-D1011.
Gruber, A., G. Rocap, P. G. Kroth, E. V. Armbrust and T. Mock (2015). Plastid proteome prediction for diatoms and other algae with secondary plastids of the red lineage. Plant J **81**(3): 519-528.
Gschloessl, B., Y. Guermeur and J. M. Cock (2008). HECTAR: a method to predict subcellular targeting in heterokonts. BMC Bioinformatics **9**: 393.
Hannaert, V., M.A. Albert, D.J. Ridgen, M.T. da Silva Giotto, O. Thiemann, R.C. Garratt, J. Van Roy, F. R. Opperdoes and P.A.M. Michels. Kinetic characterization, structure modelling studies and crystallization of *Trypanosoma brucei* enolase. Eur J Biochem **270**, 3205-3213.
Hartley, J. L., G. F. Temple and M. A. Brasch (2000). DNA cloning using in vitro site-specific recombination. Genome Res **10**(11): 1788-1795.
Hippmann, A. A., N. Schuback, K.-M. Moon, J. P. McCrow, A. E. Allen, L. F. Foster, B. R. Green and M. T. Maldonado (2022). Proteomic analysis of metabolic pathways supports chloroplast–mitochondria cross-talk in a Cu-limited diatom. Plant Direct **6**(1): e376.
Horton, P., K. J. Park, T. Obayashi, N. Fujita, H. Harada, C. J. Adams-Collier and K. Nakai (2007). WoLF PSORT: protein localization predictor. Nucl Acids Res **35**: W585-W587.
Huang, A., L. Liu, C. Yang and G. Wang (2015). *Phaeodactylum tricornutum* photorespiration takes part in glycerol metabolism and is important for nitrogen-limited response. Biotechnol Biofuels **8**(1): 1-16.
Huang, T., Y. Pan, E. Maréchal and H. Hu (2024). Proteomes reveal the lipid metabolic network in the complex plastid of *Phaeodactylum tricornutum*. Plant J **117**: 385-403.
Initiative, O. T. P. T. (2019). One thousand plant transcriptomes and the phylogenomics of green plants. Nature **574**(7780): 679-685.
Jassby, A. D. and T. Platt (1976). Mathematical formulation of the relationship between photosynthesis and light for phytoplankton. Limnol Oceanograph **21**(4): 540-547.
Jiang, Y., T. Cao, Y. Yang, H. Zhang, J. Zhang and X. Li (2023). A chlorophyll c synthase widely co-opted across phytoplankton. Science **382**(6666): 92-98.
Joli, N., L. Concia, K. Mocaer, J. Guterman, J. Laude, S. Guerin, T. Sciandra, F. Bruyant, O. Ait-Mohamed, M. Beguin, M.-H. Forget, C. Bourbousse, T. Lacour, B. Bailleul, C. Nef, M. Savoie, J.-E. Tremblay, D. A. Campbell, J. Lavaud, Y. Schwab, M. Babin and C. Bowler

(2024). Hypometabolism to survive the long polar night and subsequent successful return to light in the diatom *Fragilariopsis cylindrus*. New Phytol **241**(2193-2208).
Jones, P., D. Binns, H. Y. Chang, M. Fraser, W. Li, C. McAnulla, H. McWilliam, J. Maslen, A. Mitchell, G. Nuka, S. Pesseat, A. F. Quinn, A. Sangrador-Vegas, M. Scheremetjew, S. Y. Yong, R. Lopez and S. Hunter (2014). InterProScan 5: genome-scale protein function classification. Bioinformatics **30**(9): 1236-1240.
Jouhet, J., J. Lupette, O. Clerc, L. Magneschi, M. Bedhomme, S. Collin, S. Roy, E. Maréchal and F. Rébeillé (2017). LC-MS/MS versus TLC plus GC methods: Consistency of glycerolipid and fatty acid profiles in microalgae and higher plant cells and effect of a nitrogen starvation. PLoS One **12**(8): e0182423.
Jouhet, J., E. Maréchal, R. Bligny, J. Joyard and M. A. Block (2003). Transient increase of phosphatidylcholine in plant cells in response to phosphate deprivation. FEBS Lett**544**(1): 63-68.
Kassambara, A. and F. Mundt (2017). Package 'factoextra'. Extract and visualize the results of multivariate data analyses **76**(2).
Katoh, K., J. Rozewicki and K. D. Yamada (2017). MAFFT online service: multiple sequence alignment, interactive sequence choice and visualization. Brief Bioinform **20**: 1160-1166.
Kazamia, E., R. Sutak, J. Paz-Yepes, R. G. Dorrell, F. R. J. Vieira, J. Mach, J. Morrissey, S. Leon, F. Lam, E. Pelletier, J. M. Camadro, C. Bowler and E. Lesuisse (2018). Endocytosis-mediated siderophore uptake as a strategy for Fe acquisition in diatoms. Sci Adv **4**(5): eaar4536.
Kearse, M., R. Moir, A. Wilson, S. Stones-Havas, M. Cheung, S. Sturrock, S. Buxton, A. Cooper, S. Markowitz, C. Duran, T. Thierer, B. Ashton, P. Meintjes and A. Drummond (2012). Geneious Basic: An integrated and extendable desktop software platform for the organization and analysis of sequence data. Bioinform **28**(12): 1647-1649.
Keeling, P. J., F. Burki, H. M. Wilcox, B. Allam, E. E. Allen, L. A. Amaral-Zettler, E. V. Armbrust, J. M. Archibald, A. K. Bharti, C. J. Bell, B. Beszteri, K. D. Bidle, C. T. Cameron, L. Campbell, D. A. Caron, R. A. Cattolico, J. L. Collier, K. Coyne, S. K. Davy, P. Deschamps, S. T. Dyhrman, B. Edvardsen, R. D. Gates, C. J. Gobler, S. J. Greenwood, S. M. Guida, J. L. Jacobi, K. S. Jakobsen, E. R. James, B. Jenkins, U. John, M. D. Johnson, A. R. Juhl, A. Kamp, L. A. Katz, R. Kiene, A. Kudryavtsev, B. S. Leander, S. Lin, C. Lovejoy, D. Lynn, A. Marchetti, G. McManus, A. M. Nedelcu, S. Menden-Deuer, C. Miceli, T. Mock, M. Montresor, M. A. Moran, S. Murray, G. Nadathur, S. Nagai, P. B. Ngam, B. Palenik, J. Pawlowski, G. Petroni, G. Piganeau, M. C. Posewitz, K. Rengefors, G. Romano, M. E. Rumpho, T. Rynearson, K. B. Schilling, D. C. Schroeder, A. G. Simpson, C. H. Slamovits, D. R. Smith, G. J. Smith, S. R. Smith, H. M. Sosik, P. Stief, E. Theriot, S. N. Twary, P. E. Umale, D. Vaulot, B. Wawrik, G. L. Wheeler, W. H. Wilson, Y. Xu, A. Zingone and A. Z. Worden (2014). The Marine Microbial Eukaryote Transcriptome Sequencing Project (MMETSP): illuminating the functional diversity of eukaryotic life in the oceans through transcriptome sequencing. PLoS Biol **12**(6): e1001889.
Kopka, J., N. Schauer, S. Krueger, C. Birkemeyer, B. Usadel, E. Bergmüller, P. Dörmann, W. Weckwerth, Y. Gibon, M. Stitt, L. Willmitzer, A. R. Fernie and D. Steinhauser (2005). GMD@CSB.DB: the Golm Metabolome Database. Bioinformatics **21**(8): 1635-1638.
Krebs, H. A. (1963). Renal gluconeogenesis. Adv Enzyme Regul **1**: 385-400.
Kroth, P. G., A. Chiovitti, A. Gruber, V. Martin-Jezequel, T. Mock, M. S. Parker, M. S. Stanley, A. Kaplan, L. Caron, T. Weber, U. Maheswari, E. V. Armbrust and C. Bowler (2008). A model for carbohydrate metabolism in the diatom *Phaeodactylum tricornutum* deduced from comparative whole genome analysis. PLoS One **3**(1): e1426.

Lataretu, M. and M. Hölzer (2020). RNAflow: an effective and simple RNA-Seq differential gene expression pipeline using Nextflow. Genes (Basel) **11**(12).
Lepetit, B., D. A. Campbell, J. Lavaud, C. Büchel, R. Goss and B. Bailleul (2022). Photosynthetic Light Reactions in diatoms. II. The dynamic regulation of the various light reactions. The Molecular Life of Diatoms. A. Falciatore and T. Mock. Cham, Springer International Publishing**:** 423-464.
Levering, J., J. Broddrick, C. L. Dupont, G. Peers, K. Beeri, J. Mayers, A. A. Gallina, A. E. Allen, B. O. Palsson and K. Zengler (2016). Genome-scale model reveals metabolic basis of biomass partitioning in a model diatom. Plos One **11**(5), 0155038.
Lisec, J., N. Schauer, J. Kopka, L. Willmitzer and A. R. Fernie (2006). Gas chromatography mass spectrometry–based metabolite profiling in plants. Nat Protocol **1**(1): 387-396.
Liu, S., M. Storti, C. Bowler, G. Finazzi and R. G. Dorrell (2022). A metabolic, phylogenomic and environmental atlas of diatom plastid transporters from the model species *Phaeodactylum*. Front Plant Sci **13**, 950467.
Liu, S., Z. Wang, R. Zhu, F. Wang, Y. Cheng and Y. Liu (2021). Three Differential Expression Analysis Methods for RNA Sequencing: limma, EdgeR, DESeq2. J Vis Exp(175).
Lovejoy, C., W. F. Vincent, S. Bonilla, S. Roy, M. J. Martineau, R. Terrado, M. Potvin, R. Massana and C. Pedros-Alio (2007). Distribution, phylogeny, and growth of cold-adapted picoprasinophytes in Arctic seas. J Phycol **43**(1): 78-89.
Luedemann, A., L. von Malotky, A. Erban and J. Kopka (2012). TagFinder: preprocessing software for the fingerprinting and the profiling of gas chromatography-mass spectrometry based metabolome analyses. Methods Mol Biol **860**: 255-286.
Malviya, S., E. Scalco, S. Audic, F. Vincent, A. Veluchamy, J. Poulain, P. Wincker, D. Iudicone, C. de Vargas, L. Bittner, A. Zingone and C. Bowler (2016). Insights into global diatom distribution and diversity in the world's ocean. Proc Natl Acad Sci USA **113**(11): 1516-1525.
Maréchal, E. and J. Lupette (2020). Relationship between acyl-lipid and sterol metabolisms in diatoms. Biochimie **169**: 3-11.
McCarthy, J. K., S. R. Smith, J. P. McCrow, M. Tan, H. Zheng, K. Beeri, R. Roth, C. Lichtle, U. Goodenough, C. P. Bowler, C. L. Dupont and A. E. Allen (2017). Nitrate Reductase knockout uncouples nitrate transport from nitrate assimilation and drives repartitioning of carbon flux in a model pennate diatom. Plant Cell **29**(8): 2047-2070.
Miller, M. A., T. Schwartz, B. E. Pickett, S. He, E. B. Klem, R. H. Scheuermann, M. Passarotti, S. Kaufman and M. A. O'Leary (2015). A RESTful API for access to phylogenetic tools via the CIPRES Science Gateway. Evol Bioinform Online **11**: 43-48.
Mistry, J., S. Chuguransky, L. Williams, M. Qureshi, G. A. Salazar, E. L. L. Sonnhammer, S. C. E. Tosatto, L. Paladin, S. Raj, L. J. Richardson, R. D. Finn and A. Bateman (2020). PFAM: the protein families database in 2021. Nucleic Acids Res.
Moog, D., A. Nozawa, Y. Tozawa and R. Kamikawa (2020). Substrate specificity of plastid phosphate transporters in a non-photosynthetic diatom and its implication in evolution of red alga-derived complex plastids. Sci Rep **10**(1): 1167.
Moog, D., S. A. Rensing, J. M. Archibald, U. G. Maier and K. K. Ullrich (2015). Localization and evolution of putative triose phosphate translocators in the diatom *Phaeodactylum tricornutum*. Genom Biol Evol **7**(11): 2955-2969.
Murik, O., L. Tirichine, J. Prihoda, Y. Thomas, W. L. Araújo, A. E. Allen, A. R. Fernie and C. Bowler (2019). Downregulation of mitochondrial alternative oxidase affects chloroplast function, redox status and stress response in a marine diatom. New Phytol **221**(3): 1303-1316.

Nash, E. A., A. C. Barbrook, R. K. Edwards-Stuart, K. Bernhardt, C. J. Howe and R. E. R. Nisbet (2007). Organization of the mitochondrial genome in the dinoflagellate Amphidinium carterae. Mol Biol Evol **24**(7): 1528-1536.

Nawaly, H., H. Matsui, Y. Tsuji, K. Iwayama, H. Ohashi, K. Nakajima and Y. Matsuda (2023). Multiple plasma membrane SLC4s contribute to external HCO3– acquisition during CO2 starvation in the marine diatom *Phaeodactylum tricornutum*. J Exp Bot **74**(1): 296-307.

Nonoyama, T., E. Kazamia, H. Nawaly, X. Gao, Y. Tsuji, Y. Matsuda, C. Bowler, T. Tanaka and R. G. Dorrell (2019). Metabolic innovations underpinning the origin and diversification of the diatom chloroplast. Biomolecules **9**(8), 484.

Nymark, M., A. K. Sharma, T. Sparstad, A. M. Bones and P. Winge (2016). A CRISPR/Cas9 system adapted for gene editing in marine algae. Sci Rep **6**: 24951.

Pesant, S., F. Not, M. Picheral, S. Kandels-Lewis, N. Le Bescot, G. Gorsky, D. Iudicone, E. Karsenti, S. Speich, R. Trouble, C. Dimier, S. Searson and C. Tara Oceans (2015). Open science resources for the discovery and analysis of Tara Oceans data. Sci Data **2**.

Pierella Karlusich, J. J., C. Nef, C. Bowler and R. Dorrell (2023). Modèles biogéographiques et génomes des photoautotrophes aquatiques**:** 45-82.

Popko, J., C. Herrfurth, K. Feussner, T. Ischebeck, T. Iven, R. Haslam, M. Hamilton, O. Sayanova, J. Napier, I. Khozin-Goldberg and I. Feussner (2016). Metabolome analysis reveals betaine lipids as major source for triglyceride formation, and the accumulation of sedoheptulose during nitrogen-starvation of *Phaeodactylum tricornutum*. PLoS One **11**(10): e0164673.

Prabhakar, V., T. Löttgert, T. Gigolashvili, K. Bell, U. I. Flügge and R. E. Häusler (2009). Molecular and functional characterization of the plastid-localized phosphoenolpyruvate enolase (ENO1) from *Arabidopsis thaliana*. FEBS Lett **583**(6): 983-991.

Raines, C. A. (2003). The Calvin Cycle revisited. Photosynth Res **75**(1): 1-10.

Rainteau, D., L. Humbert, E. Delage, C. Vergnolle, C. Cantrel, M.-A. Maubert, S. Lanfranchi, R. Maldiney, S. Collin, C. Wolf, A. Zachowski and E. Ruelland (2012). Acyl chains of phospholipase D transphosphatidylation products in *Arabidopsis* cells: a study using multiple reaction monitoring mass spectrometry. PLoS One **7**(7): e41985.

Rastogi, A., U. Maheswari, R. G. Dorrell, F. R. J. Vieira, F. Maumus, A. Kustka, J. McCarthy, A. E. Allen, P. Kersey, C. Bowler and L. Tirichine (2018). Integrative analysis of large scale transcriptome data draws a comprehensive landscape of *Phaeodactylum tricornutum* genome and evolutionary origin of diatoms. Sci Rep **8**(1): 4834.

Rastogi, A., O. Murik, C. Bowler and L. Tirichine (2016). PhytoCRISP-Ex: a web-based and stand-alone application to find specific target sequences for CRISPR/CAS editing. BMC Bioinform **17**(1): 261.

Rastogi, A., F. R. J. Vieira, A. F. Deton-Cabanillas, A. Veluchamy, C. Cantrel, G. Wang, P. Vanormelingen, C. Bowler, G. Piganeau, H. Hu and L. Tirichine (2020). A genomics approach reveals the global genetic polymorphism, structure, and functional diversity of ten accessions of the marine model diatom *Phaeodactylum tricornutum*. ISME J **14**(2): 347-363.

Reinoso, R. F., B. A. Telfer and M. Rowland (1997). Tissue water content in rats measured by desiccation. J Pharmacol Toxicol Methods **38**(2): 87-92.

Royo-Llonch, M., P. Sánchez, C. Ruiz-González, G. Salazar, C. Pedrós-Alió, K. Labadie, L. Paoli, C. Tara Oceans, S. Chaffron, D. Eveillard, E. Karsenti, S. Sunagawa, P. Wincker, L. Karp-Boss, C. Bowler and S. G. Acinas (2021). Compendium of 530 metagenome-assembled bacterial and archaeal genomes from the polar Arctic Ocean. Nat Microbiol **2021**: 1561-1574.

2053 Rider, CC. and C.B. Taylor, Enolase isoenzymes in rat tissues: electrophoretic,
2054 chromatographic, immunological and kinetic properties. Biochim Biophys Acta **365**(1):
2055 285-300.
2056 Río Bártulos, C., M. B. Rogers, T. A. Williams, E. Gentekaki, H. Brinkmann, R. Cerff, M. F.
2057 Liaud, A. B. Hehl, N. R. Yarlett, A. Gruber, P. G. Kroth and M. van der Giezen (2018).
2058 Mitochondrial Glycolysis in a Major Lineage of Eukaryotes. Genom Biol Evol **10**(9):
2059 2310-2325.
2060 Sachse, M., S. Sturm, A. Gruber and P. Kroth (2013). Identification and evaluation of
2061 endogenous reference genes for steady state transcript quantification by qPCR in the
2062 diatom *Phaeodactylum tricornutum* with constitutive expression independent from time
2063 and light. Endocytobiosis Cell Res **24**: 7.
2064 Scialdone, A., S. T. Mugford, D. Feike, A. Skeffington, P. Borrill, A. Graf, A. M. Smith and M.
2065 Howard (2013). Arabidopsis plants perform arithmetic division to prevent starvation at
2066 night. eLife **2**: e00669.
2067 Scrutton, M. C. and M. F. Utter (1968). The Regulation of Glycolysis and Gluconeogenesis
2068 in Animal Tissues. Annu Rev Biochem **37**(1): 249-302.
2069 Serôdio, J. and J. Lavaud (2011). A model for describing the light response of the
2070 nonphotochemical quenching of chlorophyll fluorescence. Photosynth Res **108**(1): 61-
2071 76.
2072 Shtaida, N., I. Khozin-Goldberg and S. Boussiba (2015). The role of pyruvate hub
2073 enzymes in supplying carbon precursors for fatty acid synthesis in photosynthetic
2074 microalgae. Photosynth Res **125**(3): 407-422.
2075 Siegel, P., K. G. Baker, E. Low-Décarie and R. J. Geider (2020). High predictability of direct
2076 competition between marine diatoms under different temperatures and nutrient states.
2077 Ecol Evol **10**(14): 7276-7290.
2078 Smith, S. R., R. M. Abbriano and M. Hildebrand (2012). Comparative analysis of diatom
2079 genomes reveals substantial differences in the organization of carbon partitioning
2080 pathways. Algal Res **1**(1): 2-16.
2081 Smith, S. R., C. L. Dupont, J. K. McCarthy, J. T. Broddrick, M. Oborník, A. Horák, Z. Füssy, J.
2082 Cihlář, S. Kleessen, H. Zheng, J. P. McCrow, K. K. Hixson, W. L. Araújo, A. Nunes-Nesi, A.
2083 Fernie, Z. Nikoloski, B. O. Palsson and A. E. Allen (2019). Evolution and regulation of
2084 nitrogen flux through compartmentalized metabolic networks in a marine diatom. Nat
2085 Commun **10**(1): 4552.
2086 Smith, S. R., J. T. Gillard, A. B. Kustka, J. P. McCrow, J. H. Badger, H. Zheng, A. M. New, C. L.
2087 Dupont, T. Obata, A. R. Fernie and A. E. Allen (2016). Transcriptional orchestration of the
2088 global cellular response of a model pennate diatom to diel light cycling under iron
2089 limitation. PLoS Genet **12**(12): e1006490.
2090 Spitzer, M., J. Wildenhain, J. Rappsilber and M. Tyers (2014). BoxPlotR: a web tool for
2091 generation of box plots. Nat Methods **11**(2): 121-122.
2092 Stamatakis, A. (2014). RAxML version 8: a tool for phylogenetic analysis and post-
2093 analysis of large phylogenies. Bioinformatics **30**(9): 1312-1313.
2094 Strassert, J. F. H., I. Irisarri, T. A. Williams and F. Burki (2021). A molecular timescale for
2095 eukaryote evolution with implications for the origin of red algal-derived plastids. Nat
2096 Commun **12**(1): 1879.
2097 Sutherland, E. W., T. Posternak and C. F. Cori (1949). Mechanism of the phosphoglyceric
2098 mutase reaction. J Biol Chem **181**(1): 153-159.
2099 Tanaka, R. and A. Tanaka (2007). Tetrapyrrole biosynthesis in higher plants. Annu Rev
2100 Plant Biol **58**: 321-346.

2101 Tardif, M., A. Atteia, M. Specht, G. Cogne, N. Rolland, S. Brugière, M. Hippler, M. Ferro, C.
2102 Bruley, G. Peltier, O. Vallon and L. Cournac (2012). PredAlgo: a new subcellular
2103 localization prediction tool dedicated to green algae. Mol Biol Evol **29**(12): 3625-3639.
2104 Troncoso-Ponce, M. A., J. Rivoal, S. Dorion, R. Sánchez, M. Venegas-Calerón, A. J. Moreno-
2105 Pérez, S. Baud, R. Garcés and E. Martínez-Force (2018). Molecular and biochemical
2106 characterization of the sunflower (Helianthus annuus L.) cytosolic and plastidial
2107 enolases in relation to seed development. Plant Sci **272**: 117-130.
2108 Uwizeye, C., J. Decelle, P. Jouneau, B. Gallet, J. Keck, C. Moriscot, F. Chevalier, N. Schieber,
2109 R. Templin, G. Curien, Y. Schwab, G. Schoehn, S. C. Zeeman, D. Falconet and G. Finazzi
2110 (2020). Morphological bases of phytoplankton energy management and physiological
2111 responses unveiled by 3D subcellular imaging. Nat Commun **12**: 1à49.
2112 Worden, A. Z., J. H. Lee, T. Mock, P. Rouze, M. P. Simmons, A. L. Aerts, A. E. Allen, M. L.
2113 Cuvelier, E. Derelle, M. V. Everett, E. Foulon, J. Grimwood, H. Gundlach, B. Henrissat, C.
2114 Napoli, S. M. McDonald, M. S. Parker, S. Rombauts, A. Salamov, P. Von Dassow, J. H.
2115 Badger, P. M. Coutinho, E. Demir, I. Dubchak, C. Gentemann, W. Eikrem, J. E. Gready, U.
2116 John, W. Lanier, E. A. Lindquist, S. Lucas, K. F. X. Mayer, H. Moreau, F. Not, R. Otillar, O.
2117 Panaud, J. Pangilinan, I. Paulsen, B. Piegu, A. Poliakov, S. Robbens, J. Schmutz, E. Toulza,
2118 T. Wyss, A. Zelensky, K. Zhou, E. V. Armbrust, D. Bhattacharya, U. W. Goodenough, Y. Van
2119 de Peer and I. V. Grigoriev (2009). Green evolution and dynamic adaptations revealed by
2120 genomes of the marine picoeukaryotes *Micromonas*. Science **324**(5924): 268-272.
2121 Yang, L., Z. Wang, A. Zhang, R. Bhawal, C. Li, S. Zhang, L. Cheng and J. Hua (2022).
2122 Reduction of the canonical function of a glycolytic enzyme enolase triggers immune
2123 responses that further affect metabolism and growth in *Arabidopsis*. Plant Cell **34**(5):
2124 1745-1767.
2125 Ye, J., G. Coulouris, I. Zaretskaya, I. Cutcutache, S. Rozen and T. L. Madden (2012).
2126 Primer-BLAST: a tool to design target-specific primers for polymerase chain reaction.
2127 BMC Bioinform **13**: 134.
2128 Yin, W. and H. Hu (2023). CRISPR/Cas9-Mediated Genome Editing via Homologous
2129 Recombination in a Centric Diatom Chaetoceros muelleri. ACS Synth Biol **12**(4): 1287-
2130 1296.
2131 Young, E. F. and J. T. Holt (2007). Prediction and analysis of long-term variability of
2132 temperature and salinity in the Irish Sea. J Geophys Res **112**(C1).
2133 Yu, G., K. Nakajima, A. Gruber, C. Rio Bartulos, A. F. Schober, B. Lepetit, E. Yohannes, Y.
2134 Matsuda and P. G. Kroth (2022). Mitochondrial phosphoenolpyruvate carboxylase
2135 contributes to carbon fixation in the diatom *Phaeodactylum tricornutum* at low inorganic
2136 carbon concentrations. New Phytol **235**: 1379-1393.
2137 Zhang, Y., A. Sampathkumar, S. M.-L. Kerber, C. Swart, C. Hille, K. Seerangan, A. Graf, L.
2138 Sweetlove and A. R. Fernie (2020). A moonlighting role for enzymes of glycolysis in the
2139 co-localization of mitochondria and chloroplasts. Nat Commun **11**(1): 4509.
2140 Zhao, Z. and S. M. Assmann (2011). The glycolytic enzyme, phosphoglycerate mutase,
2141 has critical roles in stomatal movement, vegetative growth, and pollen production in
2142 *Arabidopsis thaliana*. J Exp Bot **62**(14): 5179-5189.
2143 Zheng, Y. T., A. H. Quinn and G. Sriram (2013). Experimental evidence and isotopomer
2144 analysis of mixotrophic glucose metabolism in the marine diatom *Phaeodactylum*
2145 *tricornutum*. Microbial Cell Factories **12**: 16.
2146 Zhu, B.-H., H.-P. Shi, G.-P. Yang, N.-N. Lv, M. Yang and K.-H. Pan (2016). Silencing UDP-
2147 glucose pyrophosphorylase gene in *Phaeodactylum tricornutum* affects carbon
2148 allocation. New Biotechnol **33**(1): 237-244.

2149 Zulu, N. N., K. Zienkiewicz, K. Vollheyde and I. Feussner (2018). Current trends to
2150 comprehend lipid metabolism in diatoms. Progr Lipid Res **70**: 1-16.
2151

2152 **Figures**

2153

2154 **Fig. 1. Metabolic context and evolution of the lower half of diatom plastid**
2155 **glycolysis-gluconeogenesis. A:** schematic comparison of diatom and plant core
2156 carbon metabolism, highlighting the localization and functions of two enzymes in the
2157 lower half of glycolysis-gluconeogenesis (phospho-glycerate mutase, and enolase)
2158 whose localization to the chloroplast can connect endogenous enzymes in the Calvin
2159 cycle and pyruvate hub to create a complete glycolytic-gluconeogenic-gluconeogenic
2160 pathway. Abbreviations: GA3P- glyceraldehyde-3-phosphate; 1,3-PGA and 2,3-PGA-
2161 1,3 and 2,3 bis-phosphoglycerate; Glu-6-P- glucose-6-phosphate; PEP- phospho-
2162 enol-pyruvate; RuBP- ribulose *bis*-phosphate; PGAM- phospho-glycerate mutase;
2163 cER- chloroplast: ndoplasmic reticulum. **B, C:** consensus MrBayes topologies
2164 realised with three substitution matrices (GTR, Jones, WAG) of a 163 taxa x 413 aa
2165 alignment of organelle-targeted enolase and 105 taxa x 220 aa alignment of selected
2166 organelle-targeted PGAM1 enzymes from diatoms and their closest relatives,
2167 identifying recent duplications and recruitments of respiratory glycolytic-
2168 gluconeogenic enzymes from the mitochondria to plastid in diatoms and their closest
2169 relatives. Branch lines correspond to the frequency with which a given branching
2170 relationship was recovered, with thick branches identified by all three substitution
2171 matrices.

2172

2173 **Fig. 2. Localisation and expression of *Phaeodactylum tricornutum* cpEnolase**
2174 **and cpPGAM1A. A:** individual channel and overlay images of GFP-tagged full-length
2175 cpEnolase (Phatr3_J41515) and cpPGAM1A (Phatr3_J17086) constructs (green),
2176 chlorophyll (red) and bright-field images of transformant *P. tricornutum* lines. Scale
2177 bar: 10 µm. **B:** quantitative RT-PCR (qRT-PCR) of cpEnolase and cpPGAM1A
2178 expression in mid-exponential phase cells harvested at the mid-point of a 19C 12h
2179 light: 12h dark cycle (19LD); at the same timepoint but under 24h continuous light
2180 (19CL); and under 8C and continuous light (8CL). Relative expression levels were
2181 normalised against two housekeeping genes (RPS, RNA polymerase subunit 1; TBP,
2182 Tata binding protein) that show invariant expression in response to light cycles in

2183 *Phaeodactylum* per (Sachse, Sturm et al. 2013). *: significantly different expression
2184 levels, one-way ANOVA, P < 0.05; **, the same, P < 0.001.
2185
2186 **Fig. 3. Environmental distributions of diatom plastidial lower half glycolysis-**
2187 **gluconeogenesis meta-genes.** Total transcriptome **(A)** and genome **(B)** relative
2188 abundances, sampled from all (0.8-2000µm) size fractions and surface layer **(i,iii)** or
2189 DCM **(ii,iv)** stations for *Tara* Oceans meta-genes phylogenetically resolved to diatom
2190 cpEnolase **(i,ii)** and cpPGAM1 **(iii,iv).** These data provide a global overview of *Tara*
2191 Oceans meta-gene abundances, in complement to data from individual size fractions
2192 shown in **Fig. S9.** These data demonstrate higher meta-transcript abundance without
2193 commensurate increases in meta-gene abundance at high northern and southern
2194 latitudes.
2195
2196 **Fig. 4. Growth phenotypes of cpEnolase and cpPGAM1A CRISPR-Cas9**
2197 **knockout mutant and zeocin-resistant empty vector control *P. tricornutum***
2198 **lines. A:** exemplar growth curves from single experiments realised for *P. tricornutum*
2199 lines in 50 µE m^{-2} s^{-1} illumination, non-shaken cultures and replete ESAW media,
2200 under three conditions- (i) 19°C and 12h light: 12h dark Circadian cycles (« 19C
2201 LD »); (ii) 19°C and 24h continuous light (« 19C CL »); and (iii) 8°C and 24h
2202 continuous light (« 8C CL »). Hashed black lines show the approximative
2203 concentrations (between 5 x10^4 and 4 x 10^6 cells ml^{-1}) over which growth rates were
2204 calculated). **B:** mean relative log phase growth rates of each genotype under each
2205 condition, measured through a minimum of three biological replicates and two
2206 technical repetitions (six measurements per line, minimum 24 measurements per
2207 genotype), over five time-points with linear (r^2 > 0.95 relationship between log cell
2208 density and time). Asterisks indicate significant differences as inferred by one-way
2209 ANOVA. An alternative version of this figure showing absolute growth rates of
2210 individual cell lines is provided in **Fig. S14.**
2211
2212 **Fig. 5. Changes in plastid and mitochondrial metabolic architecture inferred**
2213 **from gene expression analyses. A:** predicted consensus localizations (either:
2214 chloroplast, or non-chloroplast) from ASAFind (Gruber, Rocap et al. 2015) and
2215 HECTAR (Gschloessl, Guermeur et al. 2008) of all genes inferred (P < 0.05, fold-
2216 change expression >2) to be up- or down-regulated in both cpEnolase and

2217 cpPGAM1A knockout compared to control lines under 19C LD, 19C CL and 8C CL.
2218 Significantly enriched localizations (two-tailed chi-squared test) are asterisked. **B:**
2219 relative mRNA abundances of eleven genes encoding exemplar chloroplast- and
2220 mitochondria-targeted proteins, verified by qRT-PCR. Genes differentially expressed
2221 (two-tailed *t*-test, $P < 0.05$) in each condition are asterisked.
2222
2223 **Fig. 6. Volcano plots of differentially accumulated metabolites assessed by GC-**
2224 **MS.** Scatterplots of the $\log_2$ accumulation ratios and $-\log_{10}$ P-values of difference in
2225 the mass, ribitol and quality-control-normalised abundances of 39 sugars and amino
2226 acid metabolites in cpEnolase and cpPGAM1A knockout compared to empty vector
2227 control lines, measured by GC-MS in all three experimental conditions tested.
2228 Metabolites that show a differential accumulation in each plot ($P < 10^{-05}$) are labelled,
2229 with metabolites that show a differential accumulation in both knockout lines in each
2230 condition shown in black text, and five metabolites that are uniquely over-
2231 accumulated in cpEnolase knockout lines under all three conditions shown in dark
2232 red text.
2233
2234 **Fig. 7. LC-MS lipid distributions in glycolysis-gluconeogenesis mutant lines. A:**
2235 scatterplots of relative proportions of MGDG and TAG in total lipid LC-MS samples in
2236 cpEnolase and cpPGAM1A knockout lines and empty vector controls under each
2237 growth condition, showing increased MGDG: TAG in glycolysis knockout lines under
2238 19C, and the inverse relationship in cpEnolase knockout lines only under 8C. **B**:
2239 violin plots of relative abundances of three further lipid categories inferred to
2240 differentially accumulate in glycolysis knockout lines under different growth
2241 conditions. Significant differences between knockout and control lines (one-way
2242 ANOVA) are asterisked.
2243
2244 **Fig. 8. Proposed activities of *P. tricornutum* plastid lower glycolysis-**
2245 **gluconeogenesis.** Schematic diagram showing potential inferred roles of lower half
2246 diatom plastid glycolysis-gluconeogenesis in each environmental condition tested.
2247 The measured V_{max} of purified cpEnolase and cPGAM1A supplemented with 3-PGA
2248 (glycolytic direction) or PEP (gluconeogenic direction) are provided for 9mM
2249 substrate in each case**.**
2250

2251 **Fig. S1. Distribution of lower plastid glycolysis-glucneogenesis across**
2252 **photosynthetic eukaryotes. A:** Occurrence of plastid-targeted enolase and PGAM
2253 enzymes across 1,673 plant and algal genomes and transcriptomes, inferred using
2254 reciprocal BLAST best hit of *P. tricornutum* query enzymes as per **Fig. 1B** and **1C,**
2255 PFAM domain annotations, and in silico targeting predictions with TargetP and
2256 PredAlgo (primary chloroplast bearing lineages) and HECTAR and ASAFind
2257 (secondary lineages). **B:** scatterplots of collection site latitude for (**i)** diatoms, (ii)
2258 other stramenopiles, **(iii)** cryptomonads and haptophytes and **(iv)** green algae with
2259 detectable enolase and PGAM enzymes, divided by presence of inferred plastid-
2260 targeted isoforms. Notably, diatoms lacking both plastid-targeted glycolysis enzymes
2261 do not occur outside of low and intermediate latitudes (50°N in the northern and 60°S
2262 in the southern hemisphere) compared to other groups, which show no significant
2263 association between plastid glycolysis and latitude. The data in this figure were
2264 subselected for the phylogenies shown in **Fig. 1** and support the latitudinal
2265 correlations revealed by Tara analysis of **Fig. 3.**

2266 **Fig. S2. Consensus topology of a 380 taxa x 413 aa alignment of Enolase**
2267 **sequences.** Sequences represent a sample of all organelle-targeted isoforms from
2268 cryptomonads, haptophytes and stramenopiles and representatives from a densely-
2269 sampled dataset of 151 taxonomic groups across the tree of life (Dorrell et al., 2021).
2270 The tree topology shown is the consensus of the best-scoring rAxML trees identified
2271 using three substitution matrices: GTR, JTT, and WAG. Branch thickness
2272 corresponds to frequency of consensus tree topology recovery in individual trees;
2273 branches are coloured by taxonomic affiliation; and tips (cryptomonads, haptophytes
2274 and stramenopiles only) by predicted *in silico* localization. Individual clades
2275 (considering both taxonomic origins and inferred localization) of organelle-targeted
2276 enolase isoform are labelled with coloured brackets. This figure extends on the
2277 topology shown in **Fig. 1B**.

2278 **Fig. S3. Consensus topology of a 220 aa x 560 taxa alignment of PGAM isoform**
2279 **1 sequences.** Data are shown as per **Fig. S1**, extending on the topology of **Fig. 1C.**
2280

2281 **Fig. S4. Consensus phylogeny of a 235 aa x 66 taxa alignment of PGAM**
2282 **isoform 2 sequences.** Data are shown as per **Fig. S1,** forming a complement to the
2283 PGAM1 topologies shown in **Fig. 1C** and **S3.**

2284

2285 **Fig. S5. PGAM2 and control confocal microscopy images for *P. tricornutum***
2286 **plastid glycolysis proteins.** Images complement those shown in Fig. 2A.
2287

2288 **Fig. S6. Relative abundances and transcriptional coordination of plastidial**
2289 **enolase, PGAM1 and PGAM2. A:** relative % accumulation of different plastid- and
2290 mitochondrial-associated carbon metabolism proteins (large points) and all known
2291 plastid-encoded or inferred plastid-targeted proteins (small points, with power-law
2292 trendline) for experimental proteomics of *Phaeodactylum tricornutum* total cell
2293 proteomes (horizontal axis) or plastid-enriched protein fractions (vertical axis),
2294 following (Huang, Pan et al. 2024). Only proteins detected in at least two replicates of
2295 plastid-enriched and total cell fractions are included, and abundances are
2296 renormalized based on the total abundances of these proteins. Both cpEnolase
2297 (Phatr3_J41515) and cpPGAM1A (Phatr3_J17086) are detected in the plastid-
2298 associated proteome fraction with similar frequencies to other plastid carbon
2299 metabolism proteins, whereas other predicted plastid-targeted PGAMs (e.g.
2300 cpPGAM1B, Phatr3_J51404; cPGAM2, Phatr3_J37201) are not. B: Spearman
2301 correlation coefficients of all genes across the version 3 annotation of the
2302 *Phaeodactylum tricornutum* genome against cpEnolase and cpPGAM1A; calculated
2303 from ranked transcript data (Liu, Storti et al. 2022) from two merged datasets,
2304 PhaeoNet (Ait-Mohamed, Novák Vanclová et al. 2020) and DiatomPortal (Ashworth,
2305 Turkarslan et al. 2016). Genes are coloured by inferred *in silico* localisation; and
2306 other annotated enolase and PGAM enzymes in the *Phaeodactylum* genome are
2307 shown as large, labelled points. Notably, while cpEnolase and cpPGAM1A show a
2308 strong positive *(r* > 0.8) coregulation to one another, other PGAM isoforms (e.g.
2309 cpPGAM1B, cpPGAM2) show less apparent coregulation to either of these two
2310 genes. These data support the experimental localisations shown in **Fig. 2A**, and
2311 identify cPGAM1A as the PGAM most likely to work cooperatively with cpEnolase
2312 from the homologues shown in **Fig. 1C.**
2313

2314 **Fig. S7. Relative transcriptional regulation of cpEnolase and cpPGAM under**
2315 **nutrient, light and temperature stress conditions. A-C:** the relative ratio of plastid
2316 to mitochondria-targeted gene isoform expression for enolase (vertical axis), PGAM1
2317 (horizontal axis), and PGAM2 (bubble size) in published *Phaeodactylum* RNAseq

2318 data subject to nitrate limitation (McCarthy, Smith et al. 2017), phosphate starvation
2319 and addition (Cruz de Carvalho, Sun et al. 2016) and Circadian Fe enrichment and
2320 limitation (Smith, Gillard et al. 2016). While limited transcriptional responses are
2321 identifiable in response to changing N, P or Fe availability, the relative transcription of
2322 plastidial to mitochondrial-targeted enolase is substantially greater in RNA sampled
2323 in long day (> 12h post-illumination) conditions in **C**. **D**: relative fold changes in
2324 plastidial enolase and PGAM1 expression in published microarray data assembled in
2325 (Ashworth, Turkarslan et al. 2016), under different illumination conditions. Both
2326 Enolase and PGAM1 show substantial downregulation in dark-incubated (48h) and
2327 short post-illumination-incubated (< 0.5h) cultures, and show the greatest positive
2328 fold expression changes respectively > 16h and > 12h post-illumination. Specific data
2329 points showing either very high or low cpEnolase and cpPGAM1A expression are
2330 labelled.These data support the qRT-PCR and *Tara* Oceans observations of
2331 correlation of diatom cpEnolase and cpPGAM expression in **Fig. 2** and **Fig. 3.**
2332
2333 **Fig. S8. Identification of *Tara* Oceans homologs of diatom plastid-targeted**
2334 **enolase and PGAM enzymes. A:** Consensus rAxML JTT topologies of the
2335 phylogenetically verified *Tara* Oceans homologs of diatom plastidial enolase and
2336 PGAM enzymes and cultured species sequences, demonstrating reconciliation of
2337 retained homologs within monophyletic clades containing exclusively diatom
2338 plastidial isoforms amongst cultured species. **B:** *in silico* targeting predictions of all
2339 retrieved homologs inferred by BLAST alignment to be probably N-terminally
2340 complete, showing a strong enrichment in homologs with predicted plastid-targeting
2341 sequences. Sequences shown in this figure are analysed globally in **Fig. 3**.
2342
2343 **Fig. S9. Relative abundances of *Tara* Oceans diatom plastid glycolysis meta-**
2344 **genes.** Plots show relative abundances of meta-genes that group with **(i, iii)**
2345 cpEnolase and **(ii, iv**) cpPGAM1 sequences over individual size fractions of **(i, ii)**
2346 surface and **(iii, iv)** DCM meta-transcriptome **(left)** and -genome **(right)** data. These
2347 data, which allows us to identify whether specific trends are observed in different
2348 kinds of diatom cells, ranging from the nano to micro-metre scale, support global
2349 trends observed across from 0.8- 2000 µm filtered size fractions and surface layers
2350 shown in **Fig. 3**.
2351

2352 **Fig. S10. Normalised atitudinal regressions of *Tara* cpEnolase and cpPGAM1**
2353 **sequences.** Scatterplots of *Tara* Ocean expression patterns of sequences assigned
2354 phylogenetically to diatom cpEnolase and cpPGAM1A against station latitude.
2355 Abundances are shown for 0.8-2000 µm surface and DCM sample meta-
2356 transcriptome data, and are normalised relative to **(A**) total diatom metaT
2357 abundances at each station and **(B)** the corresponding metaG abundances for
2358 diatom cpEnolase and cpPGAM1A. Best-fit (linear) regression lines are provided for
2359 each depth. In each case, a significant positive correlation between latitude and
2360 relative expression is observed, consistent with global distributions observed in **Fig.**
2361 **3.**
2362
2363 **Fig. S11. Total relative abundances of meta-genes phylogenetically reconciled**
2364 **to diatom PGAM2 in 0.8- 2000 µm filtered surface samples.** Plots showing **(A)**
2365 meta-transcriptome and **(B)** meta-genome data, showing effective congruence
2366 between both, in contrast to the high latitudinal abundance specific to meta-
2367 transcriptome data for diatom cpEnolase and cpPGAM1 as per **Fig. 3**.
2368
2369 **Fig. S12. Occurrence and mean coverage depth of *Tara* Oceans MAGs divided**
2370 **by chloroplast glycolysis state.** This figure shows mapped distributions for *Tara*
2371 meta-genome assembled genomes (MAGs (Delmont, Gaia et al. 2022)) pertaining to
2372 (**A**) diatoms, (**B**) chlorophytes, and (**C**) other algal groups (haptophytes,
2373 pelagophytes, dictyochophytes, chrysophytes, bolidophytes, cryptomonads)
2374 containing members with inferred lower half plastidial glycolysis. MAGs are divided
2375 by the inferred occurrence of which chloroplast-targeted enolase and PGAM
2376 enzymes could be inferred using combined RbH to *Phaeodactylum* queries, PFAM
2377 annotation, and in silico targeting prediction (TargetP, WolfPSort, PredAlgo,
2378 HECTAR, ASAFind): (i) detection of plastid-targeted homologues of both enzymes;
2379 (**ii**) detection of cpEnolase or cpPGAM only; (**iii**) detection of neither. Bubble sizes
2380 correspond to the mean vertical coverage of meta-gene reads recruited to each MAG
2381 as a proxy of abundance. In each case the linear correlation and P-value (two-tailed
2382 *t*-test) of correlation between mean vertical mapped depth and absolute latitude is
2383 provided. Notably there is a positive correlation between the retrieval of either plastid
2384 glycolysis protein and greater mapped read depth at high latitudes in diatoms, and
2385 also the retrieval of both plastid glycolysis proteins and greater mapped read depth at

2386 high latitudes in chlorophytes, although no such trend is observed in other algal
2387 groups. The latitudinal associations observed for diatom MAG abundances support
2388 expression trends shown in **Fig. 3,** although the chlorophyte MAG abundances point
2389 to the presence of novel plastid glycolytic pathways absent from the cultured species
2390 shown in **Fig. 1**.
2391
2392 **Fig. S13. Genotypes of *P. tricornutum* glycolysis knockout lines. A:** alignments
2393 of the two CRISPR regions targeted for mutagenesis of cpEnolase (Phatr3_J41515)
2394 and cpPGAM1A (Phatr3_J17086), and the genotypes obtained from Sanger
2395 sequences of homozygous CRISPR knockouts obtained for each gene. **B:** average
2396 relative expression level of each mutated gene, assessed by quantitative RT-PCR
2397 with two primer combinations and normalised against two housekeeping genes (RNA
2398 polymerase II and TATA binding protein), expressed as a % of the relative
2399 expression levels calculated in two empty vector expression controls. One-way *t*-test
2400 significance levels of the knockdown of gene expression in each knockout line
2401 compared to the empty vector controls are provided. Knockout lines shown in this
2402 figure were used for growth and integrative 'omic analyses as per **Figs. 3-6**.
2403
2404 **Fig. S14. Absolute and individual growth phenotypes of cpEnolase and**
2405 **cpPGAM1A CRISPR-Cas9 knockout mutant lines. A:** growth curves of knockout
2406 lines, shown as per **Fig. 4**, but with absolute as opposed to logarithmic cell
2407 concentrations B: scatterplot showing the average and standard deviation relative
2408 growth rates for each cell line studied under 19C CL (vertical) and 19C LD (horizontal
2409 axis). Each point corresponds to an individual line, with genotype indicated by point
2410 colours, and standard deviations of growth rates by error bars. Despite individual
2411 variances in growth rate between lines, knockout lines show consistently slower
2412 growth than empty vector controls under both conditions, particularly 19C CL.
2413
2414 **Fig. S15. Measured photo-physiology of glycolysis knockout lines A:** Curves for
2415 **(i-ii)** relative electron transport (rETR) of photosystem II fitted as a function of light
2416 intensity) and **(iii-iv)** photoprotective non-photochemical quenching (NPQ) fitted as a
2417 function of E. Separate values are shown for cultures in CL **(i, iii)** and LD **(ii, iv)**
2418 growth conditions. Data points are the mean between the average values (*n*=2-4)
2419 measured in each strain within each genotype (Control = 2, cpEnolase

2420 complemented = 2, cpPGAM1A complemented = 3, cpEnolase knockout = 6,
2421 cpPGAM1A knockout = 3). **B:** Violin plots of PSII functional absorption cross-section
2422 (σPSII), measured with a MINIFIRe spectrometer for glycolysis mutant versus control
2423 lines under each growth conditions. Significantly different values observed for
2424 knockout and complementation mutants relative to control lines (one-way ANOVA, P
2425 < 0.05) are asterisked, with asterisk colour corresponding to the line considered.
2426 Each boxplot includes all measured/ fitted values for each strain within a mutant line.
2427 The absence of clear photosynthetic defects contrasts with the diminished growth of
2428 knockout lines, as per **Fig. 4.**
2429
2430 **Fig. S16: Bar plots of the mean and standard deviation of the ratios of 39**
2431 **metabolites assessed by GC-MS in plastid glycolysis mutant lines under the**
2432 **three tested experimental conditions.** Data support the Volcano Plots shown in
2433 **Fig. 6**. Metabolites are sorted in ranked decreasing accumulation in mutant lines over
2434 all three conditions. Metabolites inferred to be differentially accumulated (one-way
2435 ANOVA) in each mutant line and condition are asterisked.
2436
2437 **Fig. S17. Lipid accumulation profiles under 19C LD conditions**. **A:** Volcano Plots
2438 showing (horizontal axis) $\log_2$ accumulation ratios and (vertical axis) $-\log_{10}$ one-way
2439 ANOVA, two-tailed Pvalues for separation of mean proportions of specific fatty acids,
2440 across all fatty acids observed in a specific lipid class in glycolysis mutants versus
2441 control lines, supporting the global scatter- and violin plots shown in **Fig. 7**. Specific
2442 lipids that show extreme (P < 0.01) differences in accumulation between both mutant
2443 genotypes and control lines are labelled, and coloured by lipid class. **B:** Bar plots
2444 showing total DGTA lipid class distributions in all three lines under these conditions.
2445 These data suggest limited changes in glycolysis mutant lipid architecture, barring a
2446 probable over-accumulation of *sn*-1 C16 in gycolysis mutant lipid pools, and
2447 corresponding under-accumulation of *sn*-1 C20 in mutant DGTA pools.
2448
2449 **Fig. S18. Lipid accumulation profiles under 19C CL conditions. A:** Volcano plots
2450 showing (horizontal axis) $\log_2$ accumulation ratios and (vertical axis) $-\log_{10}$ one-way
2451 ANOVA, two-tailed Pvalues for separation of mean proportions of specific fatty acids,
2452 across all fatty acids observed in a specific lipid class in glycolysis mutants versus
2453 control lines, and **B: bar plots** of SQDG and DGTA accumulation in lines harvested

2454 under **19C CL.** Data are shown as per **Fig. S17** and support global scatter- and violin
2455 plots shown in **Fig. 7.** These data suggest similar changes in glycolysis mutant lipid
2456 architecture to **19C LD**, including probable over-accumulations of *sn*-1 C16 in lieu of
2457 C20 and C14 in cpEnolase and cpPGAM1A mutant SQDG and MGDG pools.
2458
2459 **Fig. S19. Lipid accumulation profiles under 8C CL conditions.** Volcano plots
2460 showing (horizontal axis) $\log_2$ accumulation ratios and (vertical axis) $-\log_{10}$ ANOVA
2461 Pvalues for separation of mean proportions of specific fatty acids, across all fatty
2462 acids observed in a specific lipid class in cpEnolase mutants versus control lines, and
2463 cpEnolase mutants versus cpPGAM1A mutants harvested under 8C CL conditions.
2464 Data are shown as per **Fig. S17** and support global scatter- and violin plots shown in
2465 **Fig. 7.** No sigificantly differentially accumulated ($P < 10^{-05}$) lipids were observed in
2466 corresponding comparisons of cpPGAM1A mutants and control lines. These data
2467 suggest specific overaccumulations in short-chain *sn*-1 MGDG, and *sn*-2 SQDG, and
2468 C20 *sn-1* DGTA in cpEnolase mutants compared to other lines.
2469
2470 **Fig. S20. Schematic diagram of the reaction kinetics measured for *P.***
2471 ***tricornutum* cpEnolase and cPGAM1A enzymes**. The measured activities of this
2472 assay are shown in **Fig. 8.** Common enzymes are shown in green, enzymes unique
2473 to the glycolytic assay in blue, and enzymes unique to the gluconeogenic assay in
2474 red. Reaction intermediates and reversible substrates are shown in yellow and gray
2475 respectively.
2476
2477 **Supplemental Dataset S1. Phylogenetic diversity of Enolase and PGAM**
2478 **sequences from across the tree of life.**
2479
2480 **Supplemental Dataset S2. Transcriptional and localisation patterns of ptPGAM**
2481 **and ptEnolase genes in *Phaeodactylum tricornutum*.**
2482
2483 **Supplemental Dataset S3. *Tara* Oceans analysis of diatom plastidial glycolysis.**
2484
2485 **Supplemental Dataset S4. Genotyping, growth dynamics and photophysiology**
2486 **in *P. tricornutum* plastidial glycolysis mutant lines.**
2487

2488 **Supplemental Dataset S5. Differentially and conditionally expressed genes in**
2489 ***P. tricornutum* plastidial glycolysis mutants.**
2490
2491 **Supplemental Dataset S6. Lipid and metabolite profiles of *P. tricornutum***
2492 **plastidial glycolysis mutant lines, and measured reaction kinetics of expressed**
2493 **enzymes.**

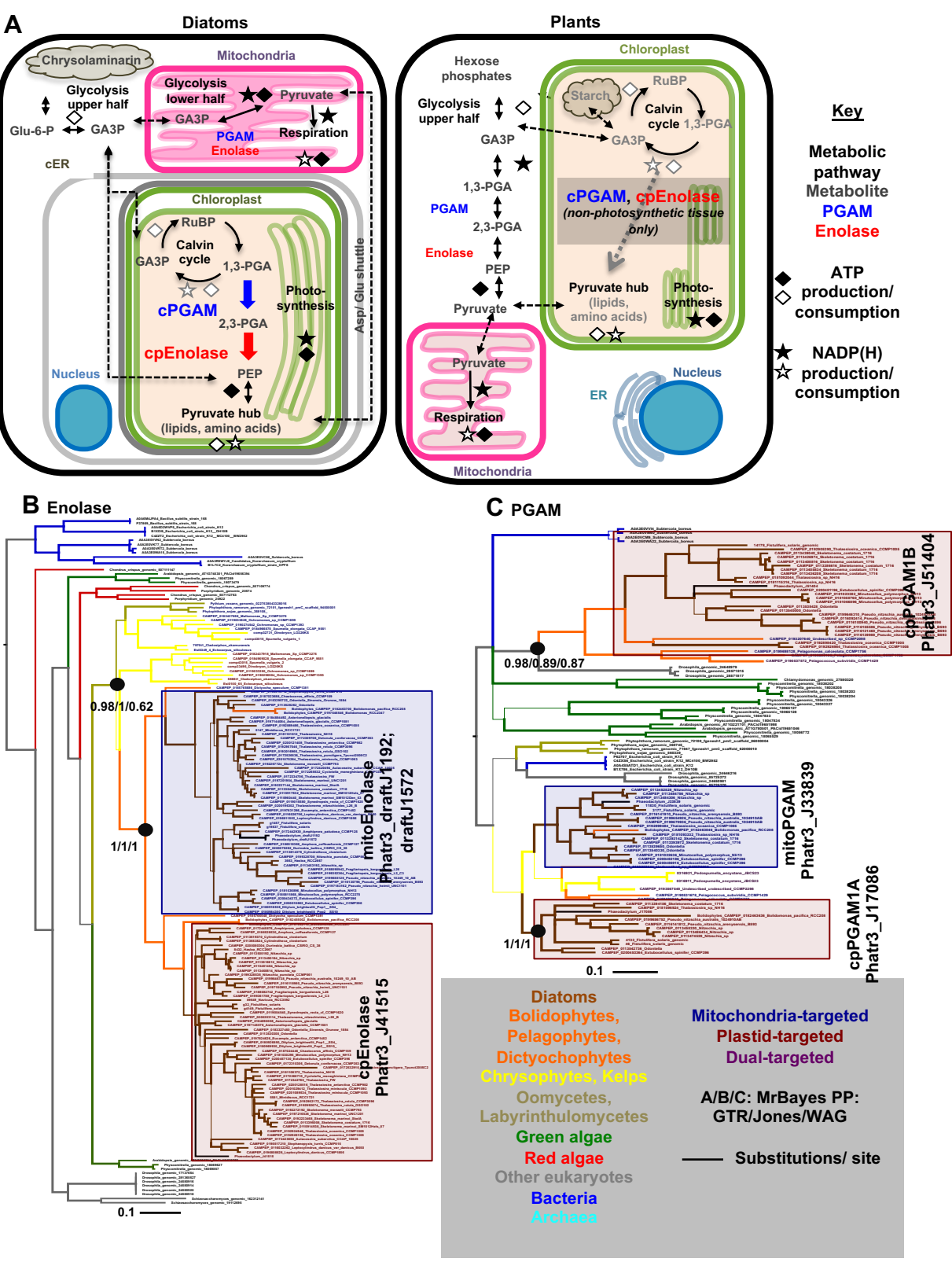

Fig. 1. Metabolic context and evolution of the lower half of diatom plastidial glycolysis-gluconeogenesis. A: schematic comparison of diatom and plant core carbon metabolism, highlighting the localization and functions of two enzymes in the lower half of glycolysis-gluconeogenesis (phospho-glycerate mutase, and enolase) whose localization to the chloroplast can connect endogenous enzymes in the Calvin cycle and pyruvate hub to create a complete glycolytic-gluconeogenic-gluconeogenic pathway. Abbreviations: GA3P- glyceraldehyde-3-phosphate; 1,3-PGA and 2,3-PGA- 1,3 and 2,3 bis-phosphoglycerate; Glu-6-P- glucose-6-phosphate; PEP- phospho-enol-pyruvate; RuBP- ribulose *bis*-phosphate; PGAM- phospho-glycerate mutase; cER- chloroplast: endoplasmic reticulum. **B, C:** consensus MrBayes topologies realised with three substitution matrices (GTR, Jones, WAG) of a 163 taxa x 413 aa alignment of organelle-targeted enolase and 105 taxa x 220 aa alignment of selected organelle-targeted PGAM1 enzymes from diatoms and their closest relatives, identifying recent duplications and recruitments of respiratory glycolytic-gluconeogenic enzymes from the mitochondria to plastid in diatoms and their closest relatives. Branch lines correspond to the frequency with which a given branching relationship was recovered, with thick branches identified by all three substitution matrices.

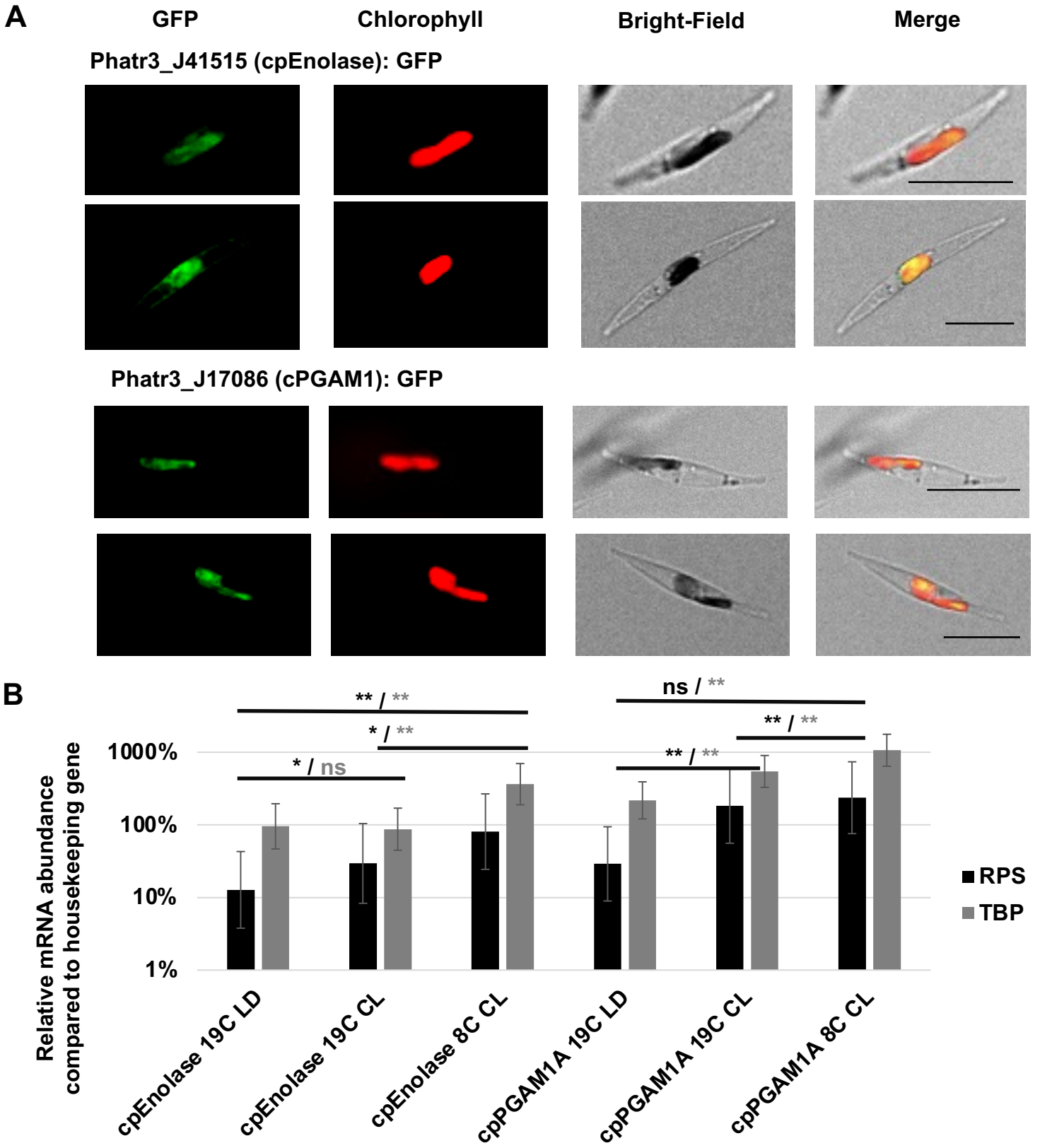

Fig. 2. Localisation and expression of *Phaeodactylum tricornutum* cpEnolase and cpPGAM1A. **A: :** overlay images of GFP-tagged full-length cpEnolase (Phatr3_J41515) and cpPGAM1A (Phatr3_J17086) constructs (green), chlorophyll (red) and bright-field images of transformant *P. tricornutum* lines. Scale bar: 10 µm. **B:** quantitative RT-PCR (qRT-PCR) of cpEnolase and cpPGAM1A expression in mid-exponential phase cells harvested at the mid-point of a 19C 12h light: 12h dark cycle (19LD); at the same timepoint but under 24h continuous light (19CL); and under 8C and continuous light (8CL). Relative expression levels were normalised against two housekeeping genes (RPS, RNA polymerase subunit 1; TBP, Tata binding protein) that show invariant expression in response to light cycles in *Phaeodactylum* per (Sachse, Sturm et al. 2013). *: significantly different expression levels, one-way ANOVA, $P < 0.05$; **, the same, $P < 0.001$.

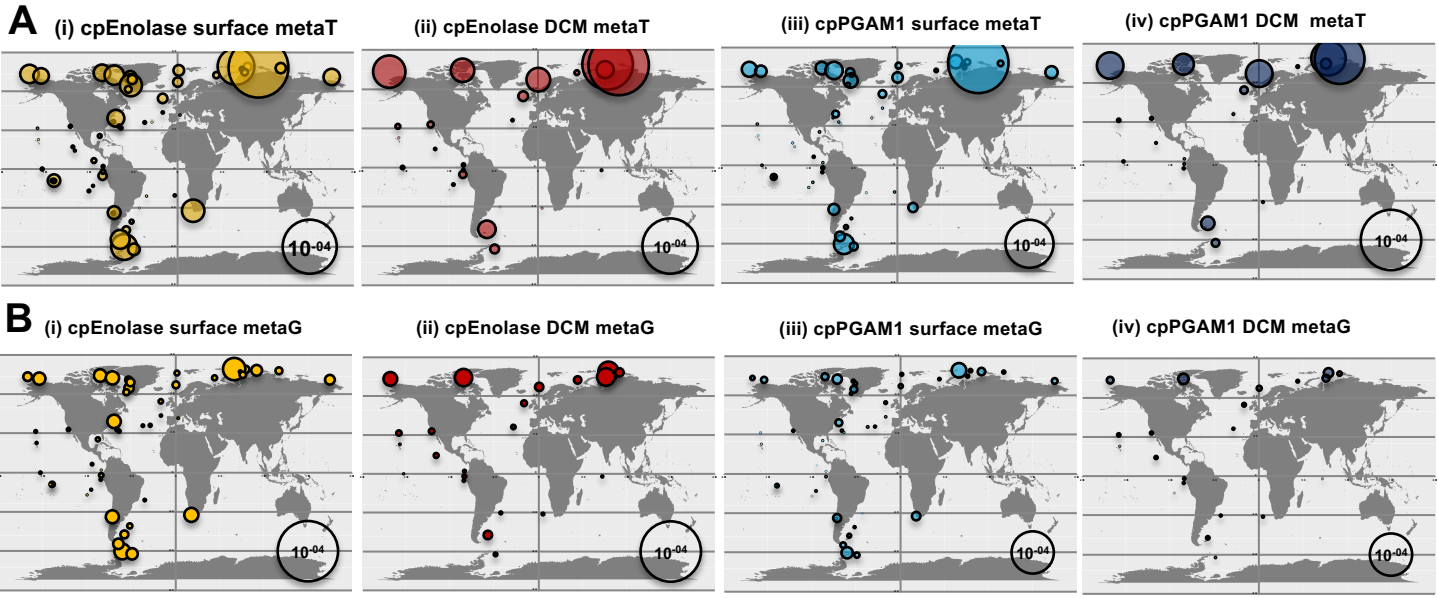

Fig. 3. Environmental distributions of diatom plastidial lower half glycolysis-gluconeogenesis meta-genes. Total transcriptome (**A**) and genome (**B**) relative abundances, sampled from all (0.8-2000µm) size fractions and surface layer (**i,iii**) or DCM (**ii,iv**) stations for *Tara* Oceans meta-genes phylogenetically resolved to diatom cpEnolase (**i,ii**) and cpPGAM1 (**iii,iv**). These data provide a global overview of *Tara* Oceans meta-gene abundances, in complement to data from individual size fractions shown in **Fig. S9**. These data demonstrate higher meta-transcript abundance without commensurate increases in meta-gene abundance at high northern and southern latitudes.

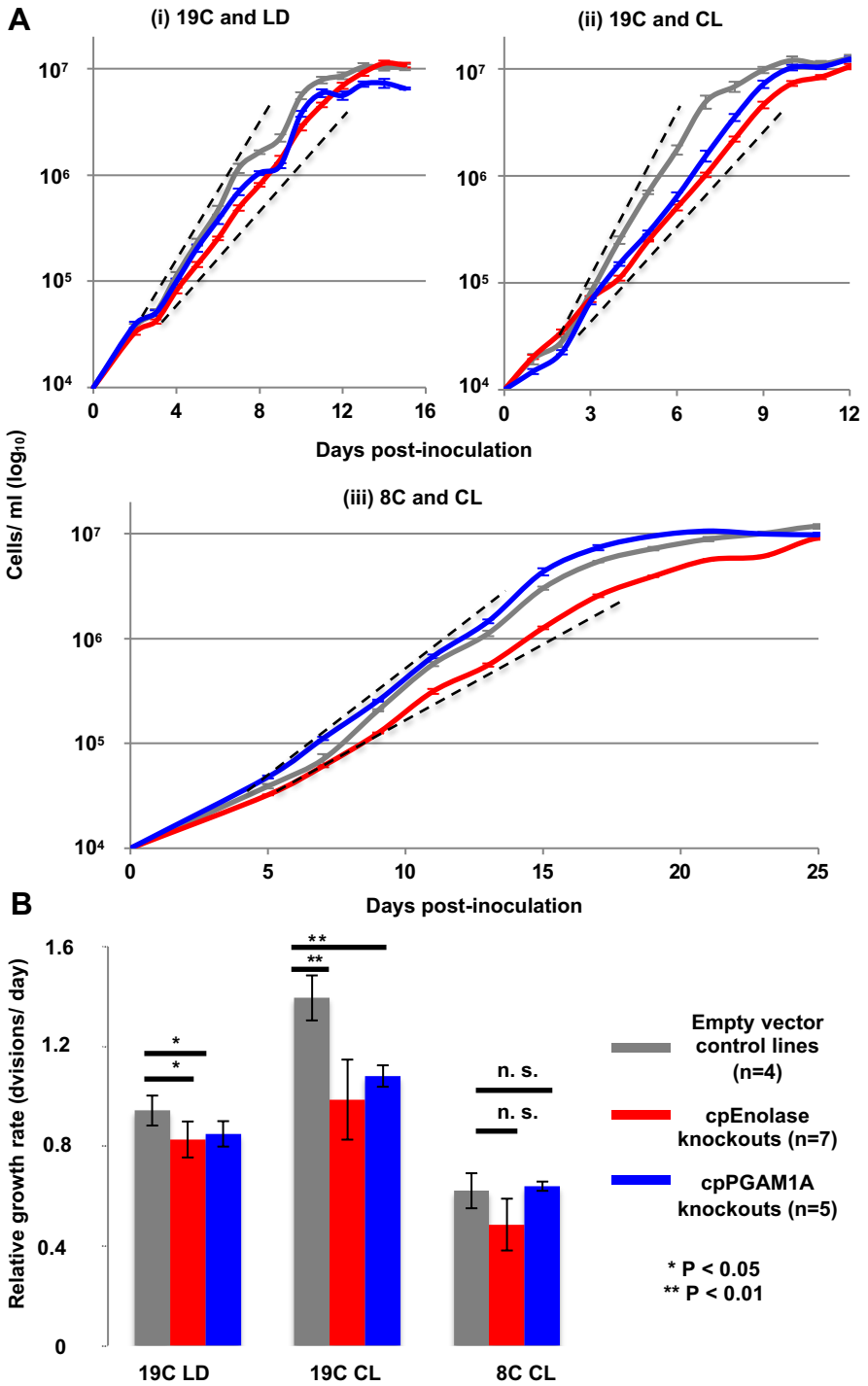

Fig. 4. Growth phenotypes of cpEnolase and cpPGAM1A CRISPR-Cas9 knockout mutant and zeocin-resistant empty vector control *P. tricornutum* lines. A: exemplar growth curves from single experiments realised for *P. tricornutum* lines in 50 µE m^{-2} s^{-1} illumination, non-shaken cultures and replete ESAW media, under three conditions- **(i)** 19°C and 12h light: 12h dark Circadian cycles (« 19C LD »); **(ii)** 19°C and 24h continuous light (« 19C CL »); and **(iii)** 8°C and 24h continuous light (« 8C CL »). Hashed black lines show the approximative concentrations (between 5 x10^4 and 4 x 10^6 cells ml^{-1}) over which growth rates were calculated). **B:** mean relative log phase growth rates of each genotype under each condition, measured through a minimum of three biological replicates and two technical repetitions (six measurements per line, minimum 24 measurements per genotype), over five time-points with linear (r^2 > 0.95 relationship between log cell density and time). Asterisks indicate significant differences as inferred by one-way ANOVA. An alternative version of this figure showing absolute growth rates of individual cell lines is provided in **Fig. S14**.

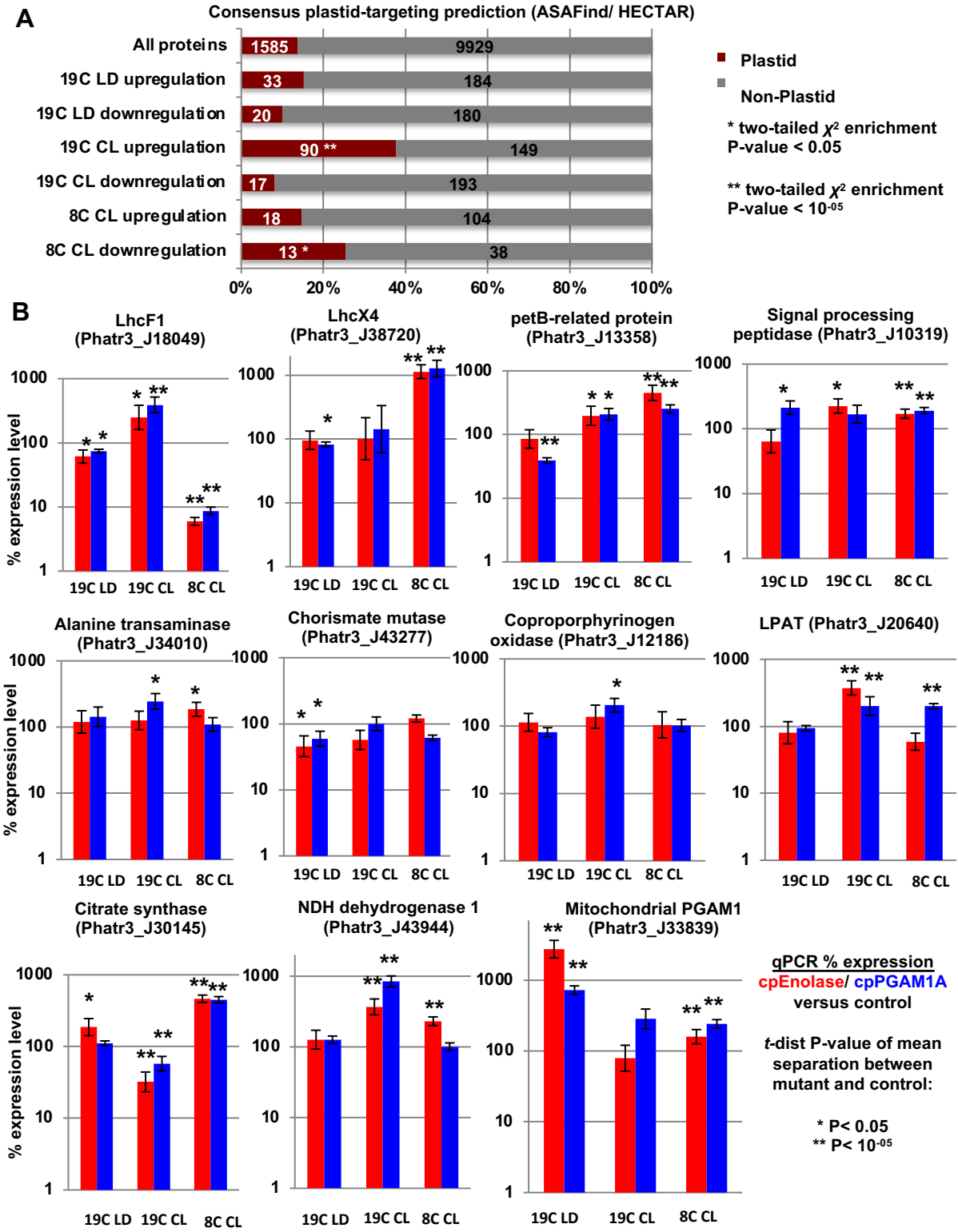

Fig. 5. Changes in plastid and mitochondrial metabolic architecture inferred from gene expression analyses. A: predicted consensus localizations (either: chloroplast, or non-chloroplast) from ASAFind (Gruber, Rocap et al. 2015) and HECTAR (Gschloessl, Guermeur et al. 2008) of all genes inferred ($P < 0.05$, fold-change expression >2) to be up- or down-regulated in both cpEnolase and cpPGAM1A knockout compared to control lines under 19C LD, 19C CL and 8C CL conditions. Significantly enriched localisations (two-tailed chi-squared test) are asterisked. **B:** relative mRNA abundances of eleven genes encoding exemplar

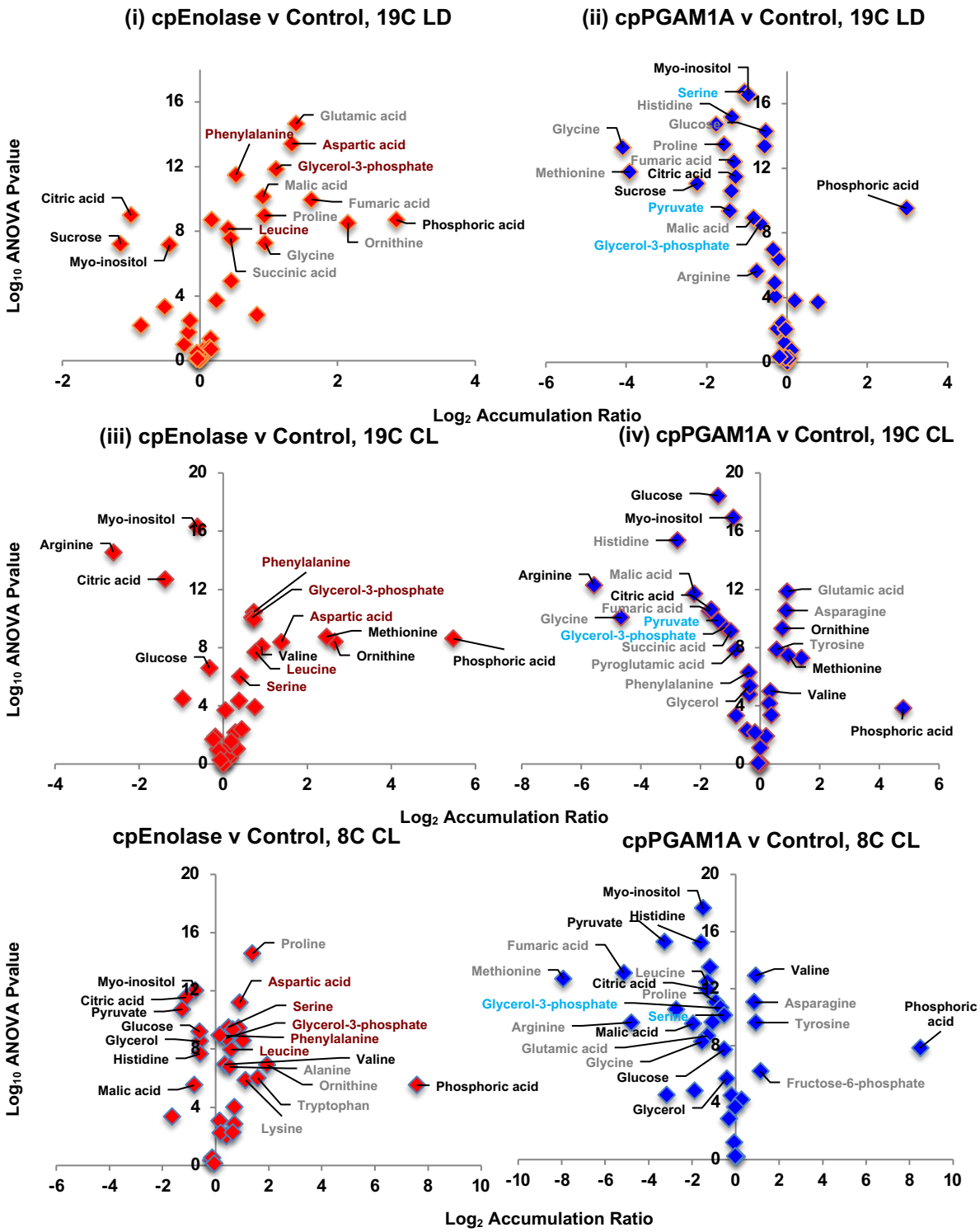

Fig. 6. Volcano plots of differentially accumulated metabolites assessed by GC-MS. Scatterplots of the $\log_2$ accumulation ratios and $-\log_{10}$ P-values of difference in the mass, ribitol and quality-control-normalised abundances of 39 sugar and amino acid metabolites in cpEnolase and cpPGAM1A knockout compared to empty vector control lines, measured by GC-MS in all three experimental conditions tested. Metabolites that show a differential accumulation in each plot ($P < 10^{-05}$) are labelled, with metabolites that show a differential accumulation in both knockout lines in each condition shown in black text, and five metabolites that are uniquely over-accumulated in cpEnolase knockout lines under all three conditions shown in dark red text.

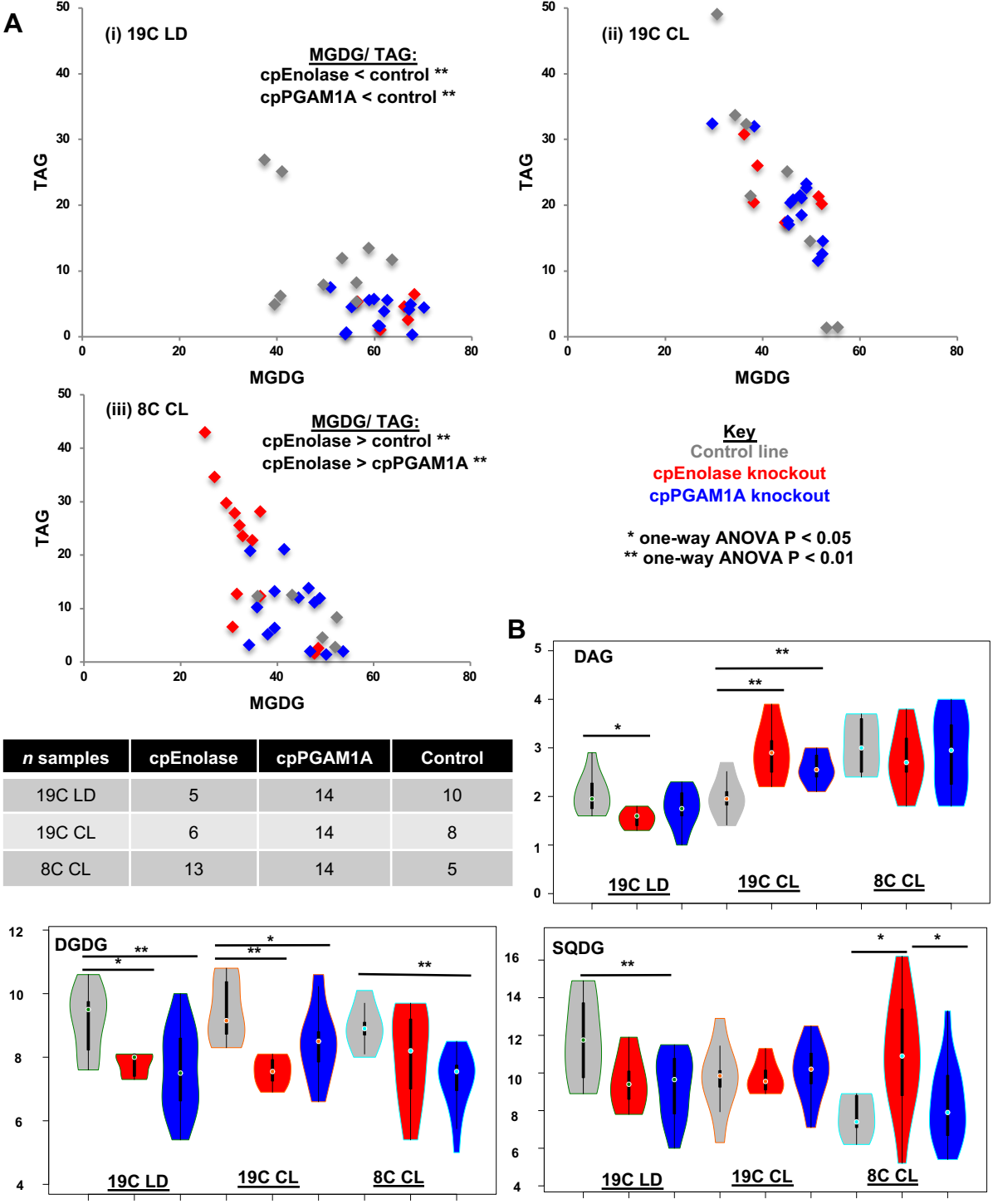

n samples	cpEnolase	cpPGAM1A	Control
19C LD	5	14	10
19C CL	6	14	8
8C CL	13	14	5

Fig. 7. LC-MS lipid distributions in glycolysis-gluconeogenesis mutant lines. A: scatterplots of relative proportions of MGDG and TAG in total lipid LC-MS samples in cpEnolase and cpPGAM1A knockout lines and empty vector controls under each growth condition, showing increased MGDG: TAG in glycolysis knockout lines under 19C, and the inverse relationship in cpEnolase knockout lines only under 8C. **B**: violin plots of relative abundances of three further lipid categories inferred to differentially accumulate in glycolysis knockout lines under different growth conditions. Significant differences between knockout and control lines (one-way ANOVA) are asterisked.

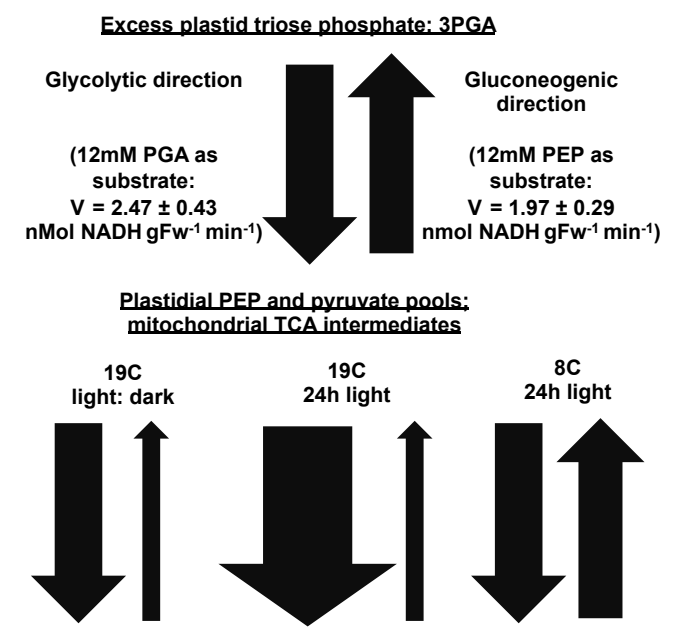

Fig. 8. Proposed kinetic activities of *P. tricornutum* plastid lower glycolysis-gluconeogenesis. Schematic diagram showing potential inferred roles of lower half diatom plastid glycolysis-gluconeogenesis in each environmental condition tested. The measured V_{max} of purified cpEnolase and cPGAM1A supplemented with 3-PGA (glycolytic direction) or PEP (gluconeogenic direction) are provided for 12mM substrate in each case

Parsed Citations

Abida, H., L. J. Dolch, C. Meï, V. Villanova, M. Conte, M. A. Block, G. Finazzi, O. Bastien, L. Tirichine, C. Bowler, F. Rébeillé, D. Petroutsos, J. Jouhet and E. Maréchal (2015). Membrane glycerolipid remodeling triggered by nitrogen and phosphorus starvation in Phaeodactylum tricornutum. Plant Physiol 167(1): 118-136.
Google Scholar: Author Only Title Only Author and Title

Ait-Mohamed, O., A. M. G. Novák Vanclová, N. Joli, Y. Liang, X. Zhao, A. Genovesio, L. Tirichine, C. Bowler and R. G. Dorrell (2020). PhaeoNet: a holistic RNAseq-based portrait of transcriptional coordination in the model diatom Phaeodactylum tricornutum. Frontiers Plant Sci 11: 590949.
Google Scholar: Author Only Title Only Author and Title

Allen, A. E., C. L. Dupont, M. Obornik, A. Horak, A. Nunes-Nesi, J. P. McCrow, H. Zheng, D. A. Johnson, H. Hu, A. R. Fernie and C. Bowler (2011). Evolution and metabolic significance of the urea cycle in photosynthetic diatoms. Nature 473(7346): 203-+.
Google Scholar: Author Only Title Only Author and Title

Almagro Armenteros, J. J., K. D. Tsirigos, C. K. Sønderby, T. N. Petersen, O. Winther, S. Brunak, G. von Heijne and H. Nielsen (2019). SignalP 5.0 improves signal peptide predictions using deep neural networks. Nat Biotechnol 37(4): 420-423.
Google Scholar: Author Only Title Only Author and Title

Andriotis, V. M., N. J. Kruger, M. J. Pike and A. M. Smith (2010). Plastidial glycolysis in developing Arabidopsis embryos. New Phytol 185(3): 649-662.
Google Scholar: Author Only Title Only Author and Title

Anoman, A. D., M. Flores-Tornero, S. Rosa-Telléz, J. Muñoz-Bertomeu, J. Segura and R. Ros (2016). The specific role of plastidial glycolysis in photosynthetic and heterotrophic cells under scrutiny through the study of glyceraldehyde-3-phosphate dehydrogenase. Plant Signal Behav 11(3): e1128614.
Google Scholar: Author Only Title Only Author and Title

Ashworth, J., S. Turkarslan, M. Harris, M. V. Orellana and N. S. Baliga (2016). Pan-transcriptomic analysis identifies coordinated and orthologous functional modules in the diatoms Thalassiosira pseudonana and Phaeodactylum tricornutum. Mar Genomics 26: 21-28.
Google Scholar: Author Only Title Only Author and Title

Bai, Y., T. Cao, O. Dautermann, P. Buschbeck, M. B. Cantrell, Y. Chen, C. D. Lein, X. Shi, M. A. Ware, F. Yang, H. Zhang, L. Zhang, G. Peers, X. Li and M. Lohr (2022). Green diatom mutants reveal an intricate biosynthetic pathway of fucoxanthin. Proc Natl Acad Sci USA 119(38): e2203708119.
Google Scholar: Author Only Title Only Author and Title

Bailleul, B., N. Berne, O. Murik, D. Petroutsos, J. Prihoda, A. Tanaka, V. Villanova, R. Bligny, S. Flori, D. Falconet, A. Krieger-Liszkay, S. Santabarbara, F. Rappaport, P. Joliot, L. Tirichine, P. G. Falkowski, P. Cardol, C. Bowler and G. Finazzi (2015). Energetic coupling between plastids and mitochondria drives CO2 assimilation in diatoms. Nature 524(7565): 366-3267.
Google Scholar: Author Only Title Only Author and Title

Behrenfeld, M. J., K. H. Halsey, E. Boss, L. Karp-Boss, A. J. Milligan and G. Peers (2021). Thoughts on the evolution and ecological niche of diatoms. Ecol Monograph 91(3): e01457.
Google Scholar: Author Only Title Only Author and Title

Broddrick, J. T., N. Du, S. R. Smith, Y. Tsuji, D. Jallet, M. A. Ware, G. Peers, Y. Matsuda, C. L. Dupont, B. G. Mitchell, B. O. Palsson and A. E. Allen (2019). Cross-compartment metabolic coupling enables flexible photoprotective mechanisms in the diatom Phaeodactylum tricornutum. New Phytol 222: 1364-1379.
Google Scholar: Author Only Title Only Author and Title

Bromke, M. A. (2013). Amino Acid biosynthesis pathways in diatoms. Metabolites 3(2): 294-311.
Google Scholar: Author Only Title Only Author and Title

Buck, J. M., C. Río Bártulos, A. Gruber and P. G. Kroth (2018). Blasticidin-S deaminase, a new selection marker for genetic transformation of the diatom. PeerJ 6: e5884.
Google Scholar: Author Only Title Only Author and Title

Buck, J. M., J. Sherman, C. R. Bártulos, M. Serif, M. Halder, J. Henkel, A. Falciatore, J. Lavaud, M. Y. Gorbunov, P. G. Kroth, P. G. Falkowski and B. Lepetit (2019). Lhcx proteins provide photoprotection via thermal dissipation of absorbed light in the diatom Phaeodactylum tricornutum. Nat Commun 10(1): 4167.
Google Scholar: Author Only Title Only Author and Title

Buseman, C. M., P. Tamura, A. A. Sparks, E. J. Baughman, S. Maatta, J. Zhao, M. R. Roth, S. W. Esch, J. Shah, T. D. Williams and R. Welti (2006). Wounding stimulates the accumulation of glycerolipids containing oxophytodienoic acid and dinor-oxophytodienoic acid in Arabidopsis leaves. Plant Physiol 142(1): 28-39.
Google Scholar: Author Only Title Only Author and Title

Bustin, S. A., V. Benes, J. A. Garson, J. Hellemans, J. Huggett, M. Kubista, R. Mueller, T. Nolan, M. W. Pfaffl, G. L. Shipley, J. Vandesompele and C. T. Wittwer (2009). The MIQE Guidelines: Minimum Information for publication of Quantitative real-time PCR Experiments. Clin Chem 55(4): 611-622.
Google Scholar: Author Only Title Only Author and Title

Capella-Gutiérrez, S., J. M. Silla-Martínez and T. Gabaldón (2009). trimAl: a tool for automated alignment trimming in large-scale phylogenetic analyses. Bioinformatics 25(15): 1972-1973.
Google Scholar: Author Only Title Only Author and Title

Carradec, Q., E. Pelletier, C. Da Silva, A. Alberti, Y. Seeleuthner, R. Blanc-Mathieu, G. Lima-Mendez, F. Rocha, L. Tirichine, K. Labadie, A. Kirilovsky, A. Bertrand, S. Engelen, M. A. Madoui, R. Méheust, J. Poulain, S. Romac, D. J. Richter, G. Yoshikawa, C. Dimier, S. Kandels-Lewis, M. Picheral, S. Searson, O. Jaillon, J. M. Aury, E. Karsenti, M. B. Sullivan, S. Sunagawa, P. Bork, F. Not, P. Hingamp, J. Raes, L. Guidi, H. Ogata, C. de Vargas, D. Iudicone, C. Bowler, P. Wincker and Tara Oceans Coordinators (2018). A global ocean atlas of eukaryotic genes. Nat Commun 9(1): 373.
Google Scholar: Author Only Title Only Author and Title

Carrera, D., G. M. George, M. Fischer-Stettler, F. Galbier, S. Eicke, E. Truernit, S. Streb and S. C. Zeeman (2021). Distinct plastid fructose bisphosphate aldolases function in photosynthetic and non-photosynthetic metabolism in Arabidopsis. J Exp Bot 72(10): 3739-3755.
Google Scholar: Author Only Title Only Author and Title

Chang, Y. F., J. S. Imam and M. F. Wilkinson (2007). The nonsense-mediated decay RNA surveillance pathway. Annu Rev Biochem 76: 51-74.
Google Scholar: Author Only Title Only Author and Title

Cruz de Carvalho, M. H., H. X. Sun, C. Bowler and N. H. Chua (2016). Noncoding and coding transcriptome responses of a marine diatom to phosphate fluctuations. New Phytol 210(2): 497-510.
Google Scholar: Author Only Title Only Author and Title

Delmont, T. O., M. Gaia, D. D. Hinsinger, P. Frémont, C. Vanni, A. Fernandez-Guerra, A. M. Eren, A. Kourlaiev, L. d'Agata, Q. Clayssen, E. Villar, K. Labadie, C. Cruaud, J. Poulain, C. Da Silva, M. Wessner, B. Noel, J.-M. Aury, S. Sunagawa, S. G. Acinas, P. Bork, E. Karsenti, C. Bowler, C. Sardet, L. Stemmann, C. de Vargas, P. Wincker, M. Lescot, M. Babin, G. Gorsky, N. Grimsley, L. Guidi, P. Hingamp, O. Jaillon, S. Kandels, D. Iudicone, H. Ogata, S. Pesant, M. B. Sullivan, F. Not, K.-B. Lee, E. Boss, G. Cochrane, M. Follows, N. Poulton, J. Raes, M. Sieracki, S. Speich and E. Pelletier (2022). Functional repertoire convergence of distantly related eukaryotic plankton lineages abundant in the sunlit ocean. Cell Genom 2(5): 100123.
Google Scholar: Author Only Title Only Author and Title

Demé, B., C. Cataye, M. A. Block, E. Maréchal and J. Jouhet (2014). Contribution of galactoglycerolipids to the 3-dimensional architecture of thylakoids. FASEB J 28(8): 3373-3383.
Google Scholar: Author Only Title Only Author and Title

Dolch, L. J. and E. Maréchal (2015). Inventory of fatty acid desaturases in the pennate diatom Phaeodactylum tricornutum. Mar Drugs 13(3): 1317-1339.
Google Scholar: Author Only Title Only Author and Title

Dorrell, R. G., G. Gile, G. McCallum, R. Méheust, E. P. Bapteste, C. M. Klinger, L. Brillet-Guéguen, K. D. Freeman, D. J. Richter and C. Bowler (2017). Chimeric origins of ochrophytes and haptophytes revealed through an ancient plastid proteome. Elife 6, 23717.
Google Scholar: Author Only Title Only Author and Title

Dorrell, R. G., A. M. G. Novák Vanclová, M. Penot, J. J. Pierella Karlusich, C. Bowler, S. Liu, E. Maréchal, J. Jouhet, B. Bailleul and D. Croteau (2022). Functional physiology of novel diatom chloroplast proteins. Open Science Foundation. https://osf.io/89vm3/.
Google Scholar: Author Only Title Only Author and Title

Emanuelsson, O., S. Brunak, G. von Heijne and H. Nielsen (2007). Locating proteins in the cell using TargetP, SignalP and related tools. Nat Protocol 2(4): 953-971.
Google Scholar: Author Only Title Only Author and Title

Erdene-Ochir, E., B. K. Shin, B. Kwon, C. Jung and C. H. Pan (2019). Identification and characterisation of the novel endogenous promoter HASP1 and its signal peptide from Phaeodactylum tricornutum. Sci Rep 9(1): 9941.
Google Scholar: Author Only Title Only Author and Title

Falciatore, A., R. Casotti, C. Leblanc, C. Abrescia and C. Bowler (1999). Transformation of Nonselectable Reporter Genes in Marine Diatoms. Mar Biotechnol (NY) 1(3): 239-251.
Google Scholar: Author Only Title Only Author and Title

Folch, J., M. Lees and G. H. S. Stanley (1957). A simple method for the isolation and purification of total lipids from animal tissues. J Biol Chem 226(1): 497-509.
Google Scholar: Author Only Title Only Author and Title

Friedlingstein, P., M. W. Jones, M. O'Sullivan, R. M. Andrew, D. C. Bakker, J. Hauck, C. Le Quéré, G. P. Peters, W. Peters and J. Pongratz (2022). Global carbon budget 2021. Earth System Science Data 14(4): 1917-2005.
Google Scholar: Author Only Title Only Author and Title

Fukasawa, Y., J. Tsuji, S. C. Fu, K. Tomii, P. Horton and K. Imai (2015). MitoFates: improved prediction of mitochondrial targeting sequences and their cleavage sites. Mol Cell Proteom 14(4): 1113-1126.
Google Scholar: Author Only Title Only Author and Title

Fukayama, H., C. Masumoto, Y. Taniguchi, A. Baba-Kasai, Y. Katoh, H. Ohkawa and M. Miyao (2015). Characterization and expression analyses of two plastidic enolase genes in rice. Biosci Biotechnol Biochem 79(3): 402-409.
Google Scholar: Author Only Title Only Author and Title

Fuss, J., O. Liegmann, K. Krause and S. A. Rensing (2013). Green Targeting Predictor and Ambiguous Targeting Predictor 2: the pitfalls of plant protein targeting prediction and of transient protein expression in heterologous systems. New Phytol 200: 1022-1033.
Google Scholar: Author Only Title Only Author and Title

Gachon, C. M. M., S. Heesch, F. C. Kuepper, U. E. M. Achilles-Day, D. Brennan, C. N. Campbell, A. Clarke, R. G. Dorrell, J. Field, S. Gontarek, C. R. Menendez, R. J. Saxon, A. Veszelovszki, M. D. Guiry, K. Gharbi, M. Blaxter and J. G. Day (2013). The CCAP KnowledgeBase: linking protistan and cyanobacterial biological resources with taxonomic and molecular data. Systemat Biodiv 11(4): 407-413.
Google Scholar: Author Only Title Only Author and Title

Gilbertson, R., E. Langan and T. Mock (2022). Diatoms and their microbiomes in complex and changing polar oceans. Front Microbiol 13: 786764.
Google Scholar: Author Only Title Only Author and Title

Gorbunov, M. Y., E. Shirsin, E. Nikonova, V. V. Fadeev and P. G. Falkowski (2020). A multi-spectral fluorescence induction and relaxation (FIRe) technique for physiological and taxonomic analysis of phytoplankton communities. Mar Ecol Prog Series 644: 1-13.
Google Scholar: Author Only Title Only Author and Title

Grigoriev, I. V., R. D. Hayes, S. Calhoun, B. Kamel, A. Wang, S. Ahrendt, S. Dusheyko, R. Nikitin, S. J. Mondo, A. Salamov, I. Shabalov and A. Kuo (2021). PhycoCosm, a comparative algal genomics resource. Nucleic Acids Res 49(D1): D1004-D1011.
Google Scholar: Author Only Title Only Author and Title

Gruber, A., G. Rocap, P. G. Kroth, E. V. Armbrust and T. Mock (2015). Plastid proteome prediction for diatoms and other algae with secondary plastids of the red lineage. Plant J 81(3): 519-528.
Google Scholar: Author Only Title Only Author and Title

Gschloessl, B., Y. Guermeur and J. M. Cock (2008). HECTAR: a method to predict subcellular targeting in heterokonts. BMC Bioinformatics 9: 393.
Google Scholar: Author Only Title Only Author and Title

Hannaert, V., M.A. Albert, D.J. Ridgen, M.T. da Silva Giotto, O. Thiemann, R.C. Garratt, J. Van Roy, F. R. Opperdoes and P.A.M. Michels. Kinetic characterization, structure modelling studies and crystallization of Trypanosoma brucei enolase. Eur J Biochem 270, 3205-3213.
Google Scholar: Author Only Title Only Author and Title

Hartley, J. L., G. F. Temple and M. A. Brasch (2000). DNA cloning using in vitro site-specific recombination. Genome Res 10(11): 1788-1795.
Google Scholar: Author Only Title Only Author and Title

Hippmann, A. A., N. Schuback, K.-M. Moon, J. P. McCrow, A. E. Allen, L. F. Foster, B. R. Green and M. T. Maldonado (2022). Proteomic analysis of metabolic pathways supports chloroplast–mitochondria cross-talk in a Cu-limited diatom. Plant Direct 6(1): e376.
Google Scholar: Author Only Title Only Author and Title

Horton, P., K. J. Park, T. Obayashi, N. Fujita, H. Harada, C. J. Adams-Collier and K. Nakai (2007). WoLF PSORT: protein localization predictor. Nucl Acids Res 35: W585-W587.
Google Scholar: Author Only Title Only Author and Title

Huang, A., L. Liu, C. Yang and G. Wang (2015). Phaeodactylum tricornutum photorespiration takes part in glycerol metabolism and is important for nitrogen-limited response. Biotechnol Biofuels 8(1): 1-16.
Google Scholar: Author Only Title Only Author and Title

Huang, T., Y. Pan, E. Maréchal and H. Hu (2024). Proteomes reveal the lipid metabolic network in the complex plastid of Phaeodactylum tricornutum. Plant J 117: 385-403.
Google Scholar: Author Only Title Only Author and Title

Initiative, O. T. P. T. (2019). One thousand plant transcriptomes and the phylogenomics of green plants. Nature 574(7780): 679-685.
Google Scholar: Author Only Title Only Author and Title

Jassby, A. D. and T. Platt (1976). Mathematical formulation of the relationship between photosynthesis and light for phytoplankton. Limnol Oceanograph 21(4): 540-547.
Google Scholar: Author Only Title Only Author and Title

Jiang, Y., T. Cao, Y. Yang, H. Zhang, J. Zhang and X. Li (2023). A chlorophyll c synthase widely co-opted across phytoplankton. Science 382(6666): 92-98.
Google Scholar: Author Only Title Only Author and Title

Joli, N., L. Concia, K. Mocaer, J. Guterman, J. Laude, S. Guerin, T. Sciandra, F. Bruyant, O. Ait-Mohamed, M. Beguin, M.-H. Forget, C. Bourbousse, T. Lacour, B. Bailleul, C. Nef, M. Savoie, J.-E. Tremblay, D. A. Campbell, J. Lavaud, Y. Schwab, M. Babin and C. Bowler (2024). Hypometabolism to survive the long polar night and subsequent successful return to light in the diatom Fragilariopsis cylindrus. New Phytol 241(2193-2208).
Google Scholar: Author Only Title Only Author and Title

Jones, P., D. Binns, H. Y. Chang, M. Fraser, W. Li, C. McAnulla, H. McWilliam, J. Maslen, A. Mitchell, G. Nuka, S. Pesseat, A. F. Quinn, A. Sangrador-Vegas, M. Scheremetjew, S. Y. Yong, R. Lopez and S. Hunter (2014). InterProScan 5: genome-scale protein function classification. Bioinformatics 30(9): 1236-1240.
Google Scholar: Author Only Title Only Author and Title

Jouhet, J., J. Lupette, O. Clerc, L. Magneschi, M. Bedhomme, S. Collin, S. Roy, E. Maréchal and F. Rébeillé (2017). LC-MS/MS versus TLC plus GC methods: Consistency of glycerolipid and fatty acid profiles in microalgae and higher plant cells and effect of a nitrogen starvation. PLoS One 12(8): e0182423.
Google Scholar: Author Only Title Only Author and Title

Jouhet, J., E. Maréchal, R. Bligny, J. Joyard and M. A. Block (2003). Transient increase of phosphatidylcholine in plant cells in response to phosphate deprivation. FEBS Lett544(1): 63-68.
Google Scholar: Author Only Title Only Author and Title

Kassambara, A. and F. Mundt (2017). Package 'factoextra'. Extract and visualize the results of multivariate data analyses 76(2).
Google Scholar: Author Only Title Only Author and Title

Katoh, K., J. Rozewicki and K. D. Yamada (2017). MAFFT online service: multiple sequence alignment, interactive sequence choice and visualization. Brief Bioinform 20: 1160-1166.
Google Scholar: Author Only Title Only Author and Title

Kazamia, E., R. Sutak, J. Paz-Yepes, R. G. Dorrell, F. R. J. Vieira, J. Mach, J. Morrissey, S. Leon, F. Lam, E. Pelletier, J. M. Camadro, C. Bowler and E. Lesuisse (2018). Endocytosis-mediated siderophore uptake as a strategy for Fe acquisition in diatoms. Sci Adv 4(5): eaar4536.
Google Scholar: Author Only Title Only Author and Title

Kearse, M., R. Moir, A. Wilson, S. Stones-Havas, M. Cheung, S. Sturrock, S. Buxton, A. Cooper, S. Markowitz, C. Duran, T. Thierer, B. Ashton, P. Meintjes and A. Drummond (2012). Geneious Basic: An integrated and extendable desktop software platform for the organization and analysis of sequence data. Bioinform 28(12): 1647-1649.
Google Scholar: Author Only Title Only Author and Title

Keeling, P. J., F. Burki, H. M. Wilcox, B. Allam, E. E. Allen, L. A. Amaral-Zettler, E. V. Armbrust, J. M. Archibald, A. K. Bharti, C. J. Bell, B. Beszteri, K. D. Bidle, C. T. Cameron, L. Campbell, D. A. Caron, R. A. Cattolico, J. L. Collier, K. Coyne, S. K. Davy, P. Deschamps, S. T. Dyhrman, B. Edvardsen, R. D. Gates, C. J. Gobler, S. J. Greenwood, S. M. Guida, J. L. Jacobi, K. S. Jakobsen, E. R. James, B. Jenkins, U. John, M. D. Johnson, A. R. Juhl, A. Kamp, L. A. Katz, R. Kiene, A. Kudryavtsev, B. S. Leander, S. Lin, C. Lovejoy, D. Lynn, A. Marchetti, G. McManus, A. M. Nedelcu, S. Menden-Deuer, C. Miceli, T. Mock, M. Montresor, M. A. Moran, S. Murray, G. Nadathur, S. Nagai, P. B. Ngam, B. Palenik, J. Pawlowski, G. Petroni, G. Piganeau, M. C. Posewitz, K. Rengefors, G. Romano, M. E. Rumpho, T. Rynearson, K. B. Schilling, D. C. Schroeder, A. G. Simpson, C. H. Slamovits, D. R. Smith, G. J. Smith, S. R. Smith, H. M. Sosik, P. Stief, E. Theriot, S. N. Twary, P. E. Umale, D. Vaulot, B. Wawrik, G. L. Wheeler, W. H. Wilson, Y. Xu, A. Zingone and A. Z. Worden (2014). The Marine Microbial Eukaryote Transcriptome Sequencing Project (MMETSP): illuminating the functional diversity of eukaryotic life in the oceans through transcriptome sequencing. PLoS Biol 12(6): e1001889.
Google Scholar: Author Only Title Only Author and Title

Kopka, J., N. Schauer, S. Krueger, C. Birkemeyer, B. Usadel, E. Bergmüller, P. Dörmann, W. Weckwerth, Y. Gibon, M. Stitt, L. Willmitzer, A. R. Fernie and D. Steinhauser (2005). GMD@CSB.DB: the Golm Metabolome Database. Bioinformatics 21(8): 1635-1638.
Google Scholar: Author Only Title Only Author and Title

Krebs, H. A. (1963). Renal gluconeogenesis. Adv Enzyme Regul 1: 385-400.
Google Scholar: Author Only Title Only Author and Title

Kroth, P. G., A. Chiovitti, A. Gruber, V. Martin-Jezequel, T. Mock, M. S. Parker, M. S. Stanley, A. Kaplan, L. Caron, T. Weber, U.

Maheswari, E. V. Armbrust and C. Bowler (2008). A model for carbohydrate metabolism in the diatom Phaeodactylum tricornutum deduced from comparative whole genome analysis. PLoS One 3(1): e1426.
Google Scholar: Author Only Title Only Author and Title

Lataretu, M. and M. Hölzer (2020). RNAflow: an effective and simple RNA-Seq differential gene expression pipeline using Nextflow. Genes (Basel) 11(12).
Google Scholar: Author Only Title Only Author and Title

Lepetit, B., D. A. Campbell, J. Lavaud, C. Büchel, R. Goss and B. Bailleul (2022). Photosynthetic Light Reactions in diatoms. II. The dynamic regulation of the various light reactions. The Molecular Life of Diatoms. A. Falciatore and T. Mock. Cham, Springer International Publishing: 423-464.
Google Scholar: Author Only Title Only Author and Title

Levering, J., J. Broddrick, C. L. Dupont, G. Peers, K. Beeri, J. Mayers, A. A. Gallina, A. E. Allen, B. O. Palsson and K. Zengler (2016). Genome-scale model reveals metabolic basis of biomass partitioning in a model diatom. Plos One 11(5), 0155038.
Google Scholar: Author Only Title Only Author and Title

Lisec, J., N. Schauer, J. Kopka, L. Willmitzer and A. R. Fernie (2006). Gas chromatography mass spectrometry–based metabolite profiling in plants. Nat Protocol 1(1): 387-396.
Google Scholar: Author Only Title Only Author and Title

Liu, S., M. Storti, C. Bowler, G. Finazzi and R. G. Dorrell (2022). A metabolic, phylogenomic and environmental atlas of diatom plastid transporters from the model species Phaeodactylum. Front Plant Sci 13, 950467.
Google Scholar: Author Only Title Only Author and Title

Liu, S., Z. Wang, R. Zhu, F. Wang, Y. Cheng and Y. Liu (2021). Three Differential Expression Analysis Methods for RNA Sequencing: limma, EdgeR, DESeq2. J Vis Exp(175).
Google Scholar: Author Only Title Only Author and Title

Lovejoy, C., W. F. Vincent, S. Bonilla, S. Roy, M. J. Martineau, R. Terrado, M. Potvin, R. Massana and C. Pedros-Alio (2007). Distribution, phylogeny, and growth of cold-adapted picoprasinophytes in Arctic seas. J Phycol 43(1): 78-89.
Google Scholar: Author Only Title Only Author and Title

Luedemann, A., L. von Malotky, A. Erban and J. Kopka (2012). TagFinder: preprocessing software for the fingerprinting and the profiling of gas chromatography-mass spectrometry based metabolome analyses. Methods Mol Biol 860: 255-286.
Google Scholar: Author Only Title Only Author and Title

Malviya, S., E. Scalco, S. Audic, F. Vincent, A. Veluchamy, J. Poulain, P. Wincker, D. Iudicone, C. de Vargas, L. Bittner, A. Zingone and C. Bowler (2016). Insights into global diatom distribution and diversity in the world's ocean. Proc Natl Acad Sci USA 113(11): 1516-1525.
Google Scholar: Author Only Title Only Author and Title

Maréchal, E. and J. Lupette (2020). Relationship between acyl-lipid and sterol metabolisms in diatoms. Biochimie 169: 3-11.
Google Scholar: Author Only Title Only Author and Title

McCarthy, J. K., S. R. Smith, J. P. McCrow, M. Tan, H. Zheng, K. Beeri, R. Roth, C. Lichtle, U. Goodenough, C. P. Bowler, C. L. Dupont and A. E. Allen (2017). Nitrate Reductase knockout uncouples nitrate transport from nitrate assimilation and drives repartitioning of carbon flux in a model pennate diatom. Plant Cell 29(8): 2047-2070.
Google Scholar: Author Only Title Only Author and Title

Miller, M. A., T. Schwartz, B. E. Pickett, S. He, E. B. Klem, R. H. Scheuermann, M. Passarotti, S. Kaufman and M. A. O'Leary (2015). A RESTful API for access to phylogenetic tools via the CIPRES Science Gateway. Evol Bioinform Online 11: 43-48.
Google Scholar: Author Only Title Only Author and Title

Mistry, J., S. Chuguransky, L. Williams, M. Qureshi, G. A. Salazar, E. L. L. Sonnhammer, S. C. E. Tosatto, L. Paladin, S. Raj, L. J. Richardson, R. D. Finn and A. Bateman (2020). PFAM: the protein families database in 2021. Nucleic Acids Res.
Google Scholar: Author Only Title Only Author and Title

Moog, D., A. Nozawa, Y. Tozawa and R. Kamikawa (2020). Substrate specificity of plastid phosphate transporters in a non-photosynthetic diatom and its implication in evolution of red alga-derived complex plastids. Sci Rep 10(1): 1167.
Google Scholar: Author Only Title Only Author and Title

Moog, D., S. A. Rensing, J. M. Archibald, U. G. Maier and K. K. Ullrich (2015). Localization and evolution of putative triose phosphate translocators in the diatom Phaeodactylum tricornutum. Genom Biol Evol 7(11): 2955-2969.
Google Scholar: Author Only Title Only Author and Title

Murik, O., L. Tirichine, J. Prihoda, Y. Thomas, W. L. Araújo, A. E. Allen, A. R. Fernie and C. Bowler (2019). Downregulation of mitochondrial alternative oxidase affects chloroplast function, redox status and stress response in a marine diatom. New Phytol 221(3): 1303-1316.
Google Scholar: Author Only Title Only Author and Title

Nash, E. A., A. C. Barbrook, R. K. Edwards-Stuart, K. Bernhardt, C. J. Howe and R. E. R. Nisbet (2007). Organization of the mitochondrial genome in the dinoflagellate Amphidinium carterae. Mol Biol Evol 24(7): 1528-1536.
Google Scholar: Author Only Title Only Author and Title

Nawaly, H., H. Matsui, Y. Tsuji, K. Iwayama, H. Ohashi, K. Nakajima and Y. Matsuda (2023). Multiple plasma membrane SLC4s contribute to external HCO3– acquisition during CO2 starvation in the marine diatom Phaeodactylum tricornutum. J Exp Bot 74(1): 296-307.
Google Scholar: Author Only Title Only Author and Title

Nonoyama, T., E. Kazamia, H. Nawaly, X. Gao, Y. Tsuji, Y. Matsuda, C. Bowler, T. Tanaka and R. G. Dorrell (2019). Metabolic innovations underpinning the origin and diversification of the diatom chloroplast. Biomolecules 9(8), 484.
Google Scholar: Author Only Title Only Author and Title

Nymark, M., A. K. Sharma, T. Sparstad, A. M. Bones and P. Winge (2016). A CRISPR/Cas9 system adapted for gene editing in marine algae. Sci Rep 6: 24951.
Google Scholar: Author Only Title Only Author and Title

Pesant, S., F. Not, M. Picheral, S. Kandels-Lewis, N. Le Bescot, G. Gorsky, D. Iudicone, E. Karsenti, S. Speich, R. Trouble, C. Dimier, S. Searson and C. Tara Oceans (2015). Open science resources for the discovery and analysis of Tara Oceans data. Sci Data 2.
Google Scholar: Author Only Title Only Author and Title

Pierella Karlusich, J. J., C. Nef, C. Bowler and R. Dorrell (2023). Modèles biogéographiques et génomes des photoautotrophes aquatiques: 45-82.

Popko, J., C. Herrfurth, K. Feussner, T. Ischebeck, T. Iven, R. Haslam, M. Hamilton, O. Sayanova, J. Napier, I. Khozin-Goldberg and I. Feussner (2016). Metabolome analysis reveals betaine lipids as major source for triglyceride formation, and the accumulation of sedoheptulose during nitrogen-starvation of Phaeodactylum tricornutum. PLoS One 11(10): e0164673.
Google Scholar: Author Only Title Only Author and Title

Prabhakar, V., T. Löttgert, T. Gigolashvili, K. Bell, U. I. Flügge and R. E. Häusler (2009). Molecular and functional characterization of the plastid-localized phosphoenolpyruvate enolase (ENO1) from Arabidopsis thaliana. FEBS Lett 583(6): 983-991.
Google Scholar: Author Only Title Only Author and Title

Raines, C. A. (2003). The Calvin Cycle revisited. Photosynth Res 75(1): 1-10.
Google Scholar: Author Only Title Only Author and Title

Rainteau, D., L. Humbert, E. Delage, C. Vergnolle, C. Cantrel, M.-A. Maubert, S. Lanfranchi, R. Maldiney, S. Collin, C. Wolf, A. Zachowski and E. Ruelland (2012). Acyl chains of phospholipase D transphosphatidylation products in Arabidopsis cells: a study using multiple reaction monitoring mass spectrometry. PLoS One 7(7): e41985.
Google Scholar: Author Only Title Only Author and Title

Rastogi, A., U. Maheswari, R. G. Dorrell, F. R. J. Vieira, F. Maumus, A. Kustka, J. McCarthy, A. E. Allen, P. Kersey, C. Bowler and L. Tirichine (2018). Integrative analysis of large scale transcriptome data draws a comprehensive landscape of Phaeodactylum tricornutum genome and evolutionary origin of diatoms. Sci Rep 8(1): 4834.
Google Scholar: Author Only Title Only Author and Title

Rastogi, A., O. Murik, C. Bowler and L. Tirichine (2016). PhytoCRISP-Ex: a web-based and stand-alone application to find specific target sequences for CRISPR/CAS editing. BMC Bioinform 17(1): 261.
Google Scholar: Author Only Title Only Author and Title

Rastogi, A., F. R. J. Vieira, A. F. Deton-Cabanillas, A. Veluchamy, C. Cantrel, G. Wang, P. Vanormelingen, C. Bowler, G. Piganeau, H. Hu and L. Tirichine (2020). A genomics approach reveals the global genetic polymorphism, structure, and functional diversity of ten accessions of the marine model diatom Phaeodactylum tricornutum. ISME J 14(2): 347-363.
Google Scholar: Author Only Title Only Author and Title

Reinoso, R. F., B. A. Telfer and M. Rowland (1997). Tissue water content in rats measured by desiccation. J Pharmacol Toxicol Methods 38(2): 87-92.
Google Scholar: Author Only Title Only Author and Title

Royo-Llonch, M., P. Sánchez, C. Ruiz-González, G. Salazar, C. Pedrós-Alió, K. Labadie, L. Paoli, C. Tara Oceans, S. Chaffron, D. Eveillard, E. Karsenti, S. Sunagawa, P. Wincker, L. Karp-Boss, C. Bowler and S. G. Acinas (2021). Compendium of 530 metagenome-assembled bacterial and archaeal genomes from the polar Arctic Ocean. Nat Microbiol 2021: 1561-1574.
Google Scholar: Author Only Title Only Author and Title

Rider, CC. and C.B. Taylor, Enolase isoenzymes in rat tissues: electrophoretic, chromatographic, immunological and kinetic properties. Biochim Biophys Acta 365(1): 285-300.

Río Bártulos, C., M. B. Rogers, T. A. Williams, E. Gentekaki, H. Brinkmann, R. Cerff, M. F. Liaud, A. B. Hehl, N. R. Yarlett, A. Gruber, P. G. Kroth and M. van der Giezen (2018). Mitochondrial Glycolysis in a Major Lineage of Eukaryotes. Genom Biol Evol

10(9): 2310-2325.
Google Scholar: Author Only Title Only Author and Title

Sachse, M., S. Sturm, A. Gruber and P. Kroth (2013). Identification and evaluation of endogenous reference genes for steady state transcript quantification by qPCR in the diatom Phaeodactylum tricornutum with constitutive expression independent from time and light. Endocytobiosis Cell Res 24: 7.
Google Scholar: Author Only Title Only Author and Title

Scialdone, A., S. T. Mugford, D. Feike, A. Skeffington, P. Borrill, A. Graf, A. M. Smith and M. Howard (2013). Arabidopsis plants perform arithmetic division to prevent starvation at night. eLife 2: e00669.
Google Scholar: Author Only Title Only Author and Title

Scrutton, M. C. and M. F. Utter (1968). The Regulation of Glycolysis and Gluconeogenesis in Animal Tissues. Annu Rev Biochem 37(1): 249-302.
Google Scholar: Author Only Title Only Author and Title

Serôdio, J. and J. Lavaud (2011). A model for describing the light response of the nonphotochemical quenching of chlorophyll fluorescence. Photosynth Res 108(1): 61-76.
Google Scholar: Author Only Title Only Author and Title

Shtaida, N., I. Khozin-Goldberg and S. Boussiba (2015). The role of pyruvate hub enzymes in supplying carbon precursors for fatty acid synthesis in photosynthetic microalgae. Photosynth Res 125(3): 407-422.
Google Scholar: Author Only Title Only Author and Title

Siegel, P., K. G. Baker, E. Low-Décarie and R. J. Geider (2020). High predictability of direct competition between marine diatoms under different temperatures and nutrient states. Ecol Evol 10(14): 7276-7290.
Google Scholar: Author Only Title Only Author and Title

Smith, S. R., R. M. Abbriano and M. Hildebrand (2012). Comparative analysis of diatom genomes reveals substantial differences in the organization of carbon partitioning pathways. Algal Res 1(1): 2-16.
Google Scholar: Author Only Title Only Author and Title

Smith, S. R., C. L. Dupont, J. K. McCarthy, J. T. Broddrick, M. Oborník, A. Horák, Z. Füssy, J. Cihlář, S. Kleessen, H. Zheng, J. P. McCrow, K. K. Hixson, W. L. Araújo, A. Nunes-Nesi, A. Fernie, Z. Nikoloski, B. O. Palsson and A. E. Allen (2019). Evolution and regulation of nitrogen flux through compartmentalized metabolic networks in a marine diatom. Nat Commun 10(1): 4552.
Google Scholar: Author Only Title Only Author and Title

Smith, S. R., J. T. Gillard, A. B. Kustka, J. P. McCrow, J. H. Badger, H. Zheng, A. M. New, C. L. Dupont, T. Obata, A. R. Fernie and A. E. Allen (2016). Transcriptional orchestration of the global cellular response of a model pennate diatom to diel light cycling under iron limitation. PLoS Genet 12(12): e1006490.
Google Scholar: Author Only Title Only Author and Title

Spitzer, M., J. Wildenhain, J. Rappsilber and M. Tyers (2014). BoxPlotR: a web tool for generation of box plots. Nat Methods 11(2): 121-122.
Google Scholar: Author Only Title Only Author and Title

Stamatakis, A. (2014). RAxML version 8: a tool for phylogenetic analysis and post-analysis of large phylogenies. Bioinformatics 30(9): 1312-1313.
Google Scholar: Author Only Title Only Author and Title

Strassert, J. F. H., I. Irisarri, T. A. Williams and F. Burki (2021). A molecular timescale for eukaryote evolution with implications for the origin of red algal-derived plastids. Nat Commun 12(1): 1879.
Google Scholar: Author Only Title Only Author and Title

Sutherland, E. W., T. Posternak and C. F. Cori (1949). Mechanism of the phosphoglyceric mutase reaction. J Biol Chem 181(1): 153-159.
Google Scholar: Author Only Title Only Author and Title

Tanaka, R. and A. Tanaka (2007). Tetrapyrrole biosynthesis in higher plants. Annu Rev Plant Biol 58: 321-346.
Google Scholar: Author Only Title Only Author and Title

Tardif, M., A. Atteia, M. Specht, G. Cogne, N. Rolland, S. Brugière, M. Hippler, M. Ferro, C. Bruley, G. Peltier, O. Vallon and L. Cournac (2012). PredAlgo: a new subcellular localization prediction tool dedicated to green algae. Mol Biol Evol 29(12): 3625-3639.
Google Scholar: Author Only Title Only Author and Title

Troncoso-Ponce, M. A., J. Rivoal, S. Dorion, R. Sánchez, M. Venegas-Calerón, A. J. Moreno-Pérez, S. Baud, R. Garcés and E. Martínez-Force (2018). Molecular and biochemical characterization of the sunflower (Helianthus annuus L.) cytosolic and plastidial enolases in relation to seed development. Plant Sci 272: 117-130.
Google Scholar: Author Only Title Only Author and Title

Uwizeye, C., J. Decelle, P. Jouneau, B. Gallet, J. Keck, C. Moriscot, F. Chevalier, N. Schieber, R. Templin, G. Curien, Y. Schwab, G. Schoehn, S. C. Zeeman, D. Falconet and G. Finazzi (2020). Morphological bases of phytoplankton energy management and physiological responses unveiled by 3D subcellular imaging. Nat Commun 12: 1à49.
Google Scholar: Author Only Title Only Author and Title

Worden, A. Z., J. H. Lee, T. Mock, P. Rouze, M. P. Simmons, A. L. Aerts, A. E. Allen, M. L. Cuvelier, E. Derelle, M. V. Everett, E. Foulon, J. Grimwood, H. Gundlach, B. Henrissat, C. Napoli, S. M. McDonald, M. S. Parker, S. Rombauts, A. Salamov, P. Von Dassow, J. H. Badger, P. M. Coutinho, E. Demir, I. Dubchak, C. Gentemann, W. Eikrem, J. E. Gready, U. John, W. Lanier, E. A. Lindquist, S. Lucas, K. F. X. Mayer, H. Moreau, F. Not, R. Otillar, O. Panaud, J. Pangilinan, I. Paulsen, B. Piegu, A. Poliakov, S. Robbens, J. Schmutz, E. Toulza, T. Wyss, A. Zelensky, K. Zhou, E. V. Armbrust, D. Bhattacharya, U. W. Goodenough, Y. Van de Peer and I. V. Grigoriev (2009). Green evolution and dynamic adaptations revealed by genomes of the marine picoeukaryotes Micromonas. Science 324(5924): 268-272.
Google Scholar: Author Only Title Only Author and Title

Yang, L., Z. Wang, A. Zhang, R. Bhawal, C. Li, S. Zhang, L. Cheng and J. Hua (2022). Reduction of the canonical function of a glycolytic enzyme enolase triggers immune responses that further affect metabolism and growth in Arabidopsis. Plant Cell 34(5): 1745-1767.
Google Scholar: Author Only Title Only Author and Title

Ye, J., G. Coulouris, I. Zaretskaya, I. Cutcutache, S. Rozen and T. L. Madden (2012). Primer-BLAST: a tool to design target-specific primers for polymerase chain reaction. BMC Bioinform 13: 134.
Google Scholar: Author Only Title Only Author and Title

Yin, W. and H. Hu (2023). CRISPR/Cas9-Mediated Genome Editing via Homologous Recombination in a Centric Diatom Chaetoceros muelleri. ACS Synth Biol 12(4): 1287-1296.
Google Scholar: Author Only Title Only Author and Title

Young, E. F. and J. T. Holt (2007). Prediction and analysis of long-term variability of temperature and salinity in the Irish Sea. J Geophys Res 112(C1).
Google Scholar: Author Only Title Only Author and Title

Yu, G., K. Nakajima, A. Gruber, C. Rio Bartulos, A. F. Schober, B. Lepetit, E. Yohannes, Y. Matsuda and P. G. Kroth (2022). Mitochondrial phosphoenolpyruvate carboxylase contributes to carbon fixation in the diatom Phaeodactylum tricornutum at low inorganic carbon concentrations. New Phytol 235: 1379-1393.
Google Scholar: Author Only Title Only Author and Title

Zhang, Y., A. Sampathkumar, S. M.-L. Kerber, C. Swart, C. Hille, K. Seerangan, A. Graf, L. Sweetlove and A. R. Fernie (2020). A moonlighting role for enzymes of glycolysis in the co-localization of mitochondria and chloroplasts. Nat Commun 11(1): 4509.
Google Scholar: Author Only Title Only Author and Title

Zhao, Z. and S. M. Assmann (2011). The glycolytic enzyme, phosphoglycerate mutase, has critical roles in stomatal movement, vegetative growth, and pollen production in Arabidopsis thaliana. J Exp Bot 62(14): 5179-5189.
Google Scholar: Author Only Title Only Author and Title

Zheng, Y. T., A. H. Quinn and G. Sriram (2013). Experimental evidence and isotopomer analysis of mixotrophic glucose metabolism in the marine diatom Phaeodactylum tricornutum. Microbial Cell Factories 12: 16.
Google Scholar: Author Only Title Only Author and Title

Zhu, B.-H., H.-P. Shi, G.-P. Yang, N.-N. Lv, M. Yang and K.-H. Pan (2016). Silencing UDP-glucose pyrophosphorylase gene in Phaeodactylum tricornutum affects carbon allocation. New Biotechnol 33(1): 237-244.
Google Scholar: Author Only Title Only Author and Title

Zulu, N. N., K. Zienkiewicz, K. Vollheyde and I. Feussner (2018). Current trends to comprehend lipid metabolism in diatoms. Progr Lipid Res 70: 1-16.
Google Scholar: Author Only Title Only Author and Title